Understanding and controlling atomic layer deposition of platinum and platinum oxide

Citation for published version (APA):
Erkens, I. J. M. (2014). *Understanding and controlling atomic layer deposition of platinum and platinum oxide*. [Phd Thesis 1 (Research TU/e / Graduation TU/e), Applied Physics and Science Education]. Technische Universiteit Eindhoven. https://doi.org/10.6100/IR774636

DOI:
10.6100/IR774636

Document status and date:
Published: 01/01/2014

Document Version:
Publisher's PDF, also known as Version of Record (includes final page, issue and volume numbers)

Please check the document version of this publication:

- A submitted manuscript is the version of the article upon submission and before peer-review. There can be important differences between the submitted version and the official published version of record. People interested in the research are advised to contact the author for the final version of the publication, or visit the DOI to the publisher's website.
- The final author version and the galley proof are versions of the publication after peer review.
- The final published version features the final layout of the paper including the volume, issue and page numbers.

Link to publication

General rights
Copyright and moral rights for the publications made accessible in the public portal are retained by the authors and/or other copyright owners and it is a condition of accessing publications that users recognise and abide by the legal requirements associated with these rights.

- Users may download and print one copy of any publication from the public portal for the purpose of private study or research.
- You may not further distribute the material or use it for any profit-making activity or commercial gain
- You may freely distribute the URL identifying the publication in the public portal.

If the publication is distributed under the terms of Article 25fa of the Dutch Copyright Act, indicated by the "Taverne" license above, please follow below link for the End User Agreement:

www.tue.nl/taverne

Take down policy
If you believe that this document breaches copyright please contact us at:

openaccess@tue.nl

providing details and we will investigate your claim.

Download date: 04. Oct. 2023

Understanding and Controlling Atomic Layer Deposition of Platinum and Platinum Oxide

PROEFSCHRIFT

ter verkrijging van de graad van doctor aan de Technische Universiteit
Eindhoven, op gezag van de rector magnificus prof.dr.ir. C.J. van Duijn,
voor een commissie aangewezen door het College voor Promoties, in het
openbaar te verdedigen op dinsdag 1 juli 2014 om 16:00 uur

door

Ivo Johannes Maria Erkens

geboren te Heerlen

Dit proefschrift is goedgekeurd door de promotoren en de samenstelling van de promotiecommissie is als volgt:

Voorzitter:	prof.dr.ir. G.M.W. Kroesen
1e promotor:	prof.dr.ir. W.M.M. Kessels
2e promotor:	prof.dr. F. Roozeboom
Copromotor:	dr. M.A. Verheijen
Leden:	dr. A. Delabie (KU Leuven)
	prof.dr.ir. B.J. Kooi (RUG)
	prof.dr.ir. E.J.E. Cottaar
Adviseur:	dr.ir. S.H. Brongersma (Holst Centre/IMEC-NL)

The research project described in this dissertation has been supported by and conducted in cooperation with IMEC-NL/Holst Centre in Eindhoven, the Netherlands.

This work has also been supported by NanoNextNL, a micro and nanotechnology program of the Dutch Ministry of economic affairs, agriculture and innovation (EL&I) and 130 partners.

Printed and bound by Printservice Technische Universiteit Eindhoven
Cover design by Nick Meeuws, Oranje Vormgevers, Eindhoven

A catalogue record is available from the Eindhoven University of technology Library.
ISBN: 978-90-386-3644-3

To my dad

Contents

Chapter 1

Introduction

More Moore

Electronic devices such as computers, smart phones, and tablets play an intricate part in many aspects of our lives. The advancement of these devices is mainly driven by the semiconductor industry, which has consistently delivered faster and smaller computer chips since the early 1960's. The rate of industrial upscaling of computing power and downscaling of critical dimensions is known as *Moore's Law*, which describes that the number of transistors on integrated circuitry should double every 18 to 24 months. This roadmap maintains a virtuous cycle: through transistor scaling better performance-to-cost ratios are obtained, inducing the financial growth of the semiconductor market; this in turn allows further investments which fuels further scaling. This trend for increased performances will continue, and is labeled "*More Moore.*"

Further downscaling along the More Moore approach poses challenges for the controlled deposition of high-quality thin films. The dimensions of the structures and layers in today’s transistor designs are currently at the nanometer scale. For example, as of the 45 nm technology node, Intel introduced a hafnium-based oxide as a gate dielectric with a thickness of ~3 nm. This dielectric film needs to be deposited on the substrate with superior thickness and uniformity control. Another example of the stringent requirements for thin-film deposition can be found in the trench capacitors used in dynamic random access memories (DRAMs). In these high aspect ratio capacitor structures, one specific requirement is that both the thin-film electrode and dielectric materials are deposited with good conformality.

The requirements for the thin films in More Moore applications can be summarized as follows: high material quality, high uniformity, accurate growth and conformality control as shown schematically in Figure 1.1. Atomic layer deposition (ALD) is a thin-film deposition technique which can meet all these criteria, due to its self-limiting nature (box 1). Because of the unique characteristics of ALD, it is currently used for the most challenging thin-film deposition situations, e.g. the growth of the gate oxide in advanced processors, and the growth of the dielectric and conductor layers in trench capacitors for DRAM (1,2).

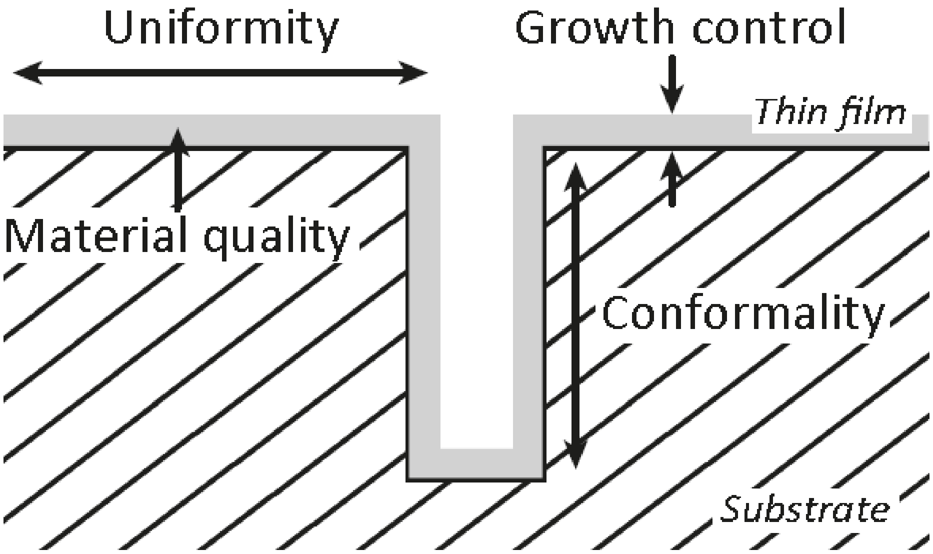

Figure 1.1. Semantic definitions of features in thin film growth on trench and planar substrates. Illustrated are the four major requirements for thin films in More Moore and More than Moore applications: a high material quality, high uniformity, accurate growth control, and good conformality.

More than Moore

The semiconductor industry is now faced with the increasing importance of a new trend: "*More than Moore*" (MtM) (3). This trend is characterized by a functional diversification of semiconductor-based devices, in which multiple functionalities, other than those for computing and data storage, are integrated into a single unit of the device (Figure 1.6). These include the interaction with the outside world through RF transceivers, sensors and actuators and subsystems for powering the unit in so-called voltage islands. These functions may include analog and mixed signal processing, the incorporation of passive components (i.e. capacitors, inductors and resistors), high-voltage components, micro-electromechanical systems (MEMS), sensors and actuators, and micro-fluid devices enabling chemical and biological functionalities. An example of such an MtM device is a metal-oxide gas sensing device described in box 2.

Box 1: Atomic Layer Deposition

ALD is a vapor-based deposition technique in which a substrate surface is exposed to alternating, time-separated doses of various vapor- or gas-phase species. During each cycle of two basic half-reactions, a submonolayer of material is formed. As an example, the well-understood model ALD process of Al_2O_3 is discussed below (4).

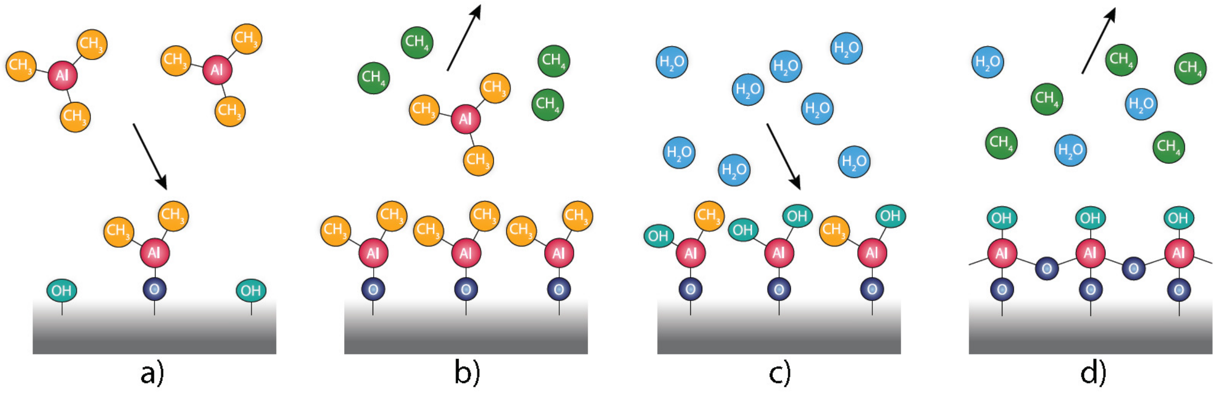

Figure 1.2. *Schematic illustration of a typical ALD process for the deposition of* Al_2O_3*. The cycle consists of alternate exposure of a surface to (a) precursor and (c) reactant gases separated by (b, d) pump or purge steps.*

A typical ALD cycle consists of 4 steps, as illustrated in Figure 1.2. The first step in the Al_2O_3 ALD cycle is the exposure of a hydroxyl-covered surface to the $Al(CH_3)_3$ precursor. During this precursor half-reaction, $Al(CH_3)_3$ molecules adsorb at the surface in a reaction with the surface hydroxyl groups, releasing CH_4 as a volatile by-product. This results in a $–CH_3$ terminated surface, which prevents the adsorption of additional precursor molecules and ensures the *self-limiting* nature of the precursor step. During the second step, excess precursor particles and volatile reaction products are purged from the chamber by an inert gas. During the third step, which again is self-limiting, H_2O molecules react with the $–CH_3$ surface groups, releasing CH_4 as a volatile reaction product, and forming new hydroxyl groups at the surface. The fourth and final step of the process is another purge step, leading to a completely self-limiting process. The cycle can now be repeated, since the last step provides the surface –OH groups required for the first step.

Because of the self-limiting nature of the ALD surface reactions, a difference in the particle flux, at different areas on either a planar or 3D substrate, still results in the same film thickness. The only requirement that needs to be fulfilled is that a sufficient flux reaches all areas. The saturation of both half-cycles leads to a characteristic number for the growth per cycle (GPC), and the process can be repeated until the desired thickness is reached.

Each ALD process has a specific temperature window in which ALD behavior is obtained, as depicted in Figure 1.3. For ideal ALD growth, the temperature window represents the temperature range over which the GPC shows a weak or no temperature dependence. Lower temperatures can either lead to an increase in GPC by precursor or co-reactant condensation, or to a reduction in GPC due to low reactivity through a limited thermal energy level preventing saturation of the surface reactions. At high temperatures, the chemicals can decompose leading to increased growth, or the film itself or the reactive surface groups involved may desorb or etch leading to a decrease in growth.

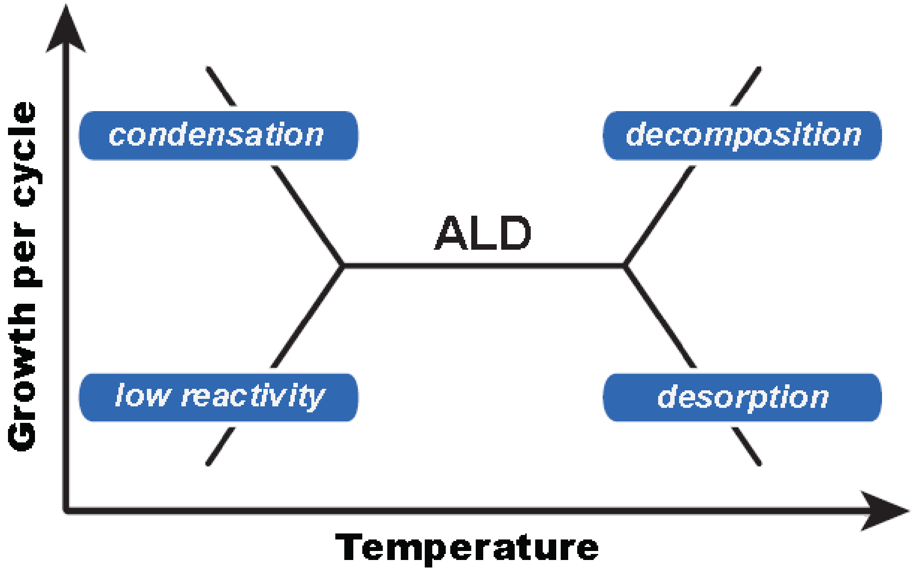

Figure 1.3. *The idealized temperature window of the ALD process, indicated by the growth per cycle as a function of temperature. In the case of ALD behavior, self-limiting growth is obtained and a weak or no dependence on temperature is observed, while outside the window the ALD behavior is lost.*

Box 2: Metal oxide gas sensing

An example of a *More than Moore* (MtM) application can be found in gas detection using a metal-oxide (MO) based gas sensing element (5). Typically, this element is heterogeneously integrated in a miniaturized package with other (Si- technology based MtM) elements for powering, heating and interaction with the outside world, together with a conventional digital processing element (see Figure 1.4). Some of the advantages of MO sensors are their low cost, robustness, high lifetime, high sensitivity, and quick response time. Some of the challenges facing the use of MO sensors are relatively high power consumption, and poor selectivity.

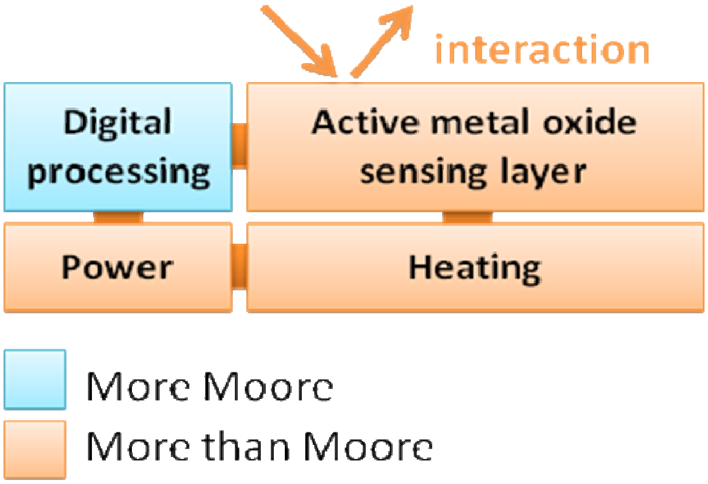

Figure 1.4. *Design of a More-than-Moore (MtM) gas detection device that integrates and complements a digital processing element and allows interaction with ambient atmosphere. A metal-oxide-based gas sensor forms the heart of such an MtM gas detector design.*

Working principle

The basic principle behind MO gas sensors is the conductivity change caused by adsorption or desorption of a gas on a gas sensitive oxide surface (see Figure 1.5). The working of MO gas sensors depends on the presence of oxygen species adsorbed to the surface of the oxide (see Figure 1.5 (a)). When these oxygen species adsorb to the surface, they attract electrons from the MO layer which changes the conductivity of the 'bulk' layer.

The target gas now interacts with the surface of the MO film through these surface adsorbed oxygen species (see Figure 1.5 (b)) (6). By removing or adding oxygen species the carrier concentration of the material changes (7). For an n-type semiconductor where electrons are the majority charge carriers, the interaction with a reducing gas (e.g. CO) will generally increase the conductivity (8,9). Since the target gas only interacts with the surface, the relative conductivity increase depends on the surface-to-volume ratio of the sensing layer. By using ultrathin (quasi-2D) films with a thickness close to the Debye length, the oxide film conductivity will be strongly influenced by gas absorption or desorption at its surface (10).

The sensitivity, response time, and recovery time of sensing devices depend strongly on the operation temperature of the sensing layer, because adsorption and desorption are temperature-activated processes. Reaching optimal operating temperatures generally requires a heating element to heat the sensing layer, leading to additional power consumption (11).

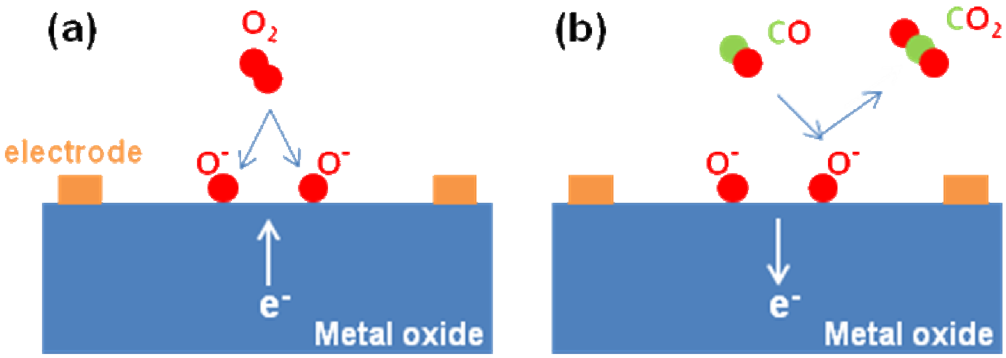

Figure 1.5. *Schematic depiction of the possible interaction of a gas sensitive metal oxide (MO) layer with a gas. (a) Oxygen species adsorb to the surface where they attract electrons from the MO layer. (b) CO reacts with surface oxygen forming* CO_2*. The electrons that are released by this reaction contribute to a conductivity increase of the 'bulk' metal oxide layer. By measuring the conductivity change the CO-concentration can be determined.*

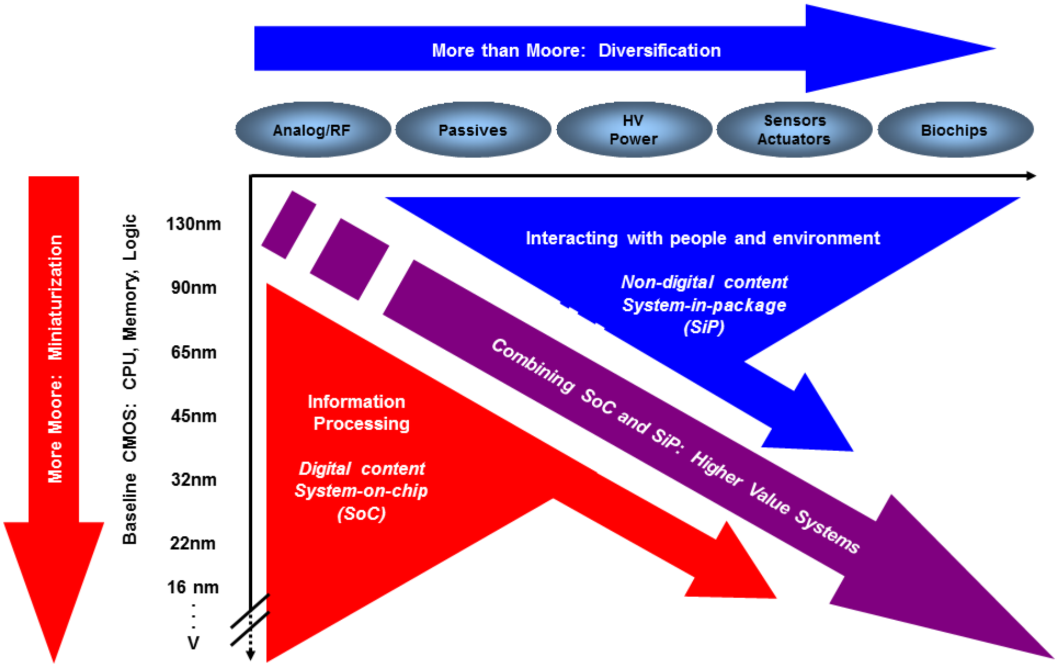

Figure 1.6. *The combined need for digital and non-digital functionalities in an integrated system is illustrated as a dual trend in the International Technology Roadmap for Semiconductors (ITRS): miniaturization in the field of information processing technology ("More Moore") and functional diversification within electronic devices ("More than Moore"). (From ITRS Roadmap, 2011 Edition Executive Summary, p. 10)(12).*

The importance of the MtM component is expected to increase over time. To enable the integration of the MtM approach, a greater diversity in terms of materials, production methods, and surface topologies is required. For example, the ALD materials toolbox that is typically used for More Moore applications (HfO_2, Al_2O_3, TiN) needs to be extended to include, e.g. gas-sensitive or transparent conductive materials (ZnO, SnO_2, In_2O_3, etc.) (5), electrode materials (Pt, Ru) (13), and catalytic materials (Pd, Rh) (14). Other examples include high-k dielectrics for MIM decoupling capacitors in RF devices ($SrTiO_3$) (15), piezoelectric materials in microactuators and energy harvesters ($PbZrTiO_3$) (16), or even alloys or doped materials (Al:ZnO) (17). Furthermore, these materials must be applied with increasing attention for fabrication conditions. For example, new production methods such as *systems in foil* solutions could provide cost-effective roll-to-roll production of OLEDs. The use of polymer substrates in this approach however, requires production at low temperatures (18). This poses even more stringent demands on future deposition techniques. Moreover, since traditional downscaling may not always deliver the desired performance, new technologies have been proposed including structures with 3D topology. For example, the interaction between thin-film sensing layers and target gases may be improved by nano-structuring the surface to obtain high aspect ratio topologies. Naturally, this requires deposition techniques that are able to accommodate 3D topologies. Compared to More Moore, MtM technologies may therefore generally require a more diverse set of materials, a more stringent manufacturing budget (e.g. in terms of temperature), and a greater demand on the 3-D compatibility of deposition techniques.

By expanding beyond the traditional methods and approaches, ALD has the potential to open up new options and new technologies for next-generation MtM applications. A wide variety of technologically important materials can be deposited using ALD, as shown in Figure 1.7 (19). The periodic table shows that the ALD materials toolbox encompasses a significant number of main-group elements, transition metals and lanthanides, either as the principal metal (squares highlighted blue) or as the non-metal components of binary compounds (grey squares). ALD can be used to deposit binary compounds such as metal oxides, nitrides, and carbides, or single-element films, in particular noble metals such as Pt, Ru, and Pd but also metals such as W. Moreover, a standard ALD process scheme can be expanded by expanding the number of steps in ALD cycles, or by combining ALD processes as is explained in box 3. By using these advanced ALD process schemes, tertiary and quaternary compounds, alloys, and even doped materials can be deposited.

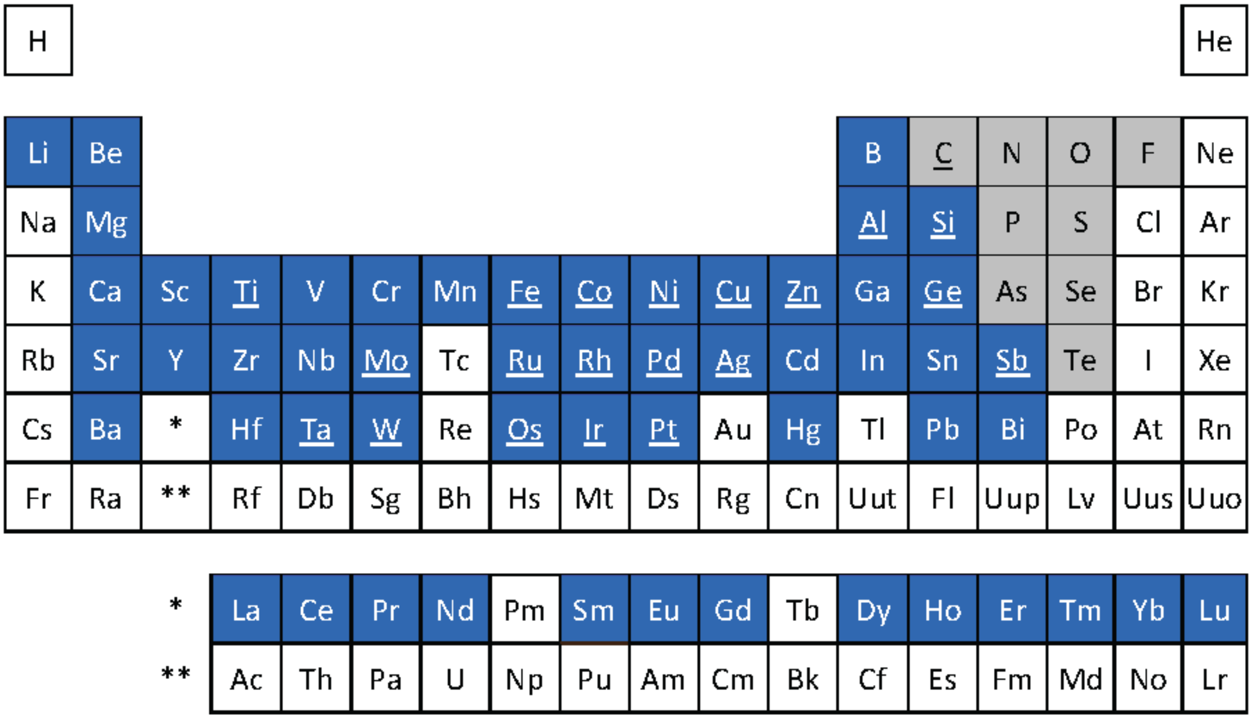

H																	He
Li	Be											B	C	N	O	F	Ne
Na	Mg											Al	Si	P	S	Cl	Ar
K	Ca	Sc	Ti	V	Cr	Mn	Fe	Co	Ni	Cu	Zn	Ga	Ge	As	Se	Br	Kr
Rb	Sr	Y	Zr	Nb	Mo	Tc	Ru	Rh	Pd	Ag	Cd	In	Sn	Sb	Te	I	Xe
Cs	Ba	*	Hf	Ta	W	Re	Os	Ir	Pt	Au	Hg	Tl	Pb	Bi	Po	At	Rn
Fr	Ra	**	Rf	Db	Sg	Bh	Hs	Mt	Ds	Rg	Cn	Uut	Fl	Uup	Lv	Uus	Uuo
		*	La	Ce	Pr	Nd	Pm	Sm	Eu	Gd	Tb	Dy	Ho	Er	Tm	Yb	Lu
		**	Ac	Th	Pa	U	Np	Pu	Am	Cm	Bk	Cf	Es	Fm	Md	No	Lr

Figure 1.7. *Periodic table denoting the materials reported to be deposited by ALD adapted from the literature (19). Metallic (and metalloid) elements with a blue background are those which have been incorporated into ALD films of compounds such as oxides, nitrides, carbides, etc. The gray background indicates elements forming the non-metallic component of the films. Underlined symbols indicate that ALD thin films of the pure element have been reported.*

Box 3: Processing opportunities for ALD

The processing possibilities of ALD can be expanded significantly by expanding the number of steps within an ALD cycle, or by combining ALD processes. Figure 1.8 shows a comparison between various process schemes. The process can consist of more than two half-cycles in what is called a *multi-step process.* In a multi-step process (Figure 1.8 (b)) additional steps can be inserted to change the process in order to widen the temperature window or achieve different material properties. For example, the ALD process based on (MeCp)PtMe$_3$ and O$_2$-plasma can be complemented with an H$_2$ step to ensure Pt deposition at lower temperatures.

ALD cycles for a certain material can also be alternated with cycles for other materials in what is called a *supercycle*. Supercycles (Figure 1.8 (c)) can be used to grow alloy, doped or multilayer films of specific elemental mixtures. An ALD cycle for the first process is run *m* times, which is followed by *n* cycles of a second ALD process. This supercycle of *m+n* cycles is then repeated *x* times until the desired thickness is reached. For example, this approach can be used to deposit Al-doped ZnO with a very precise control over the level of Al doping (17).

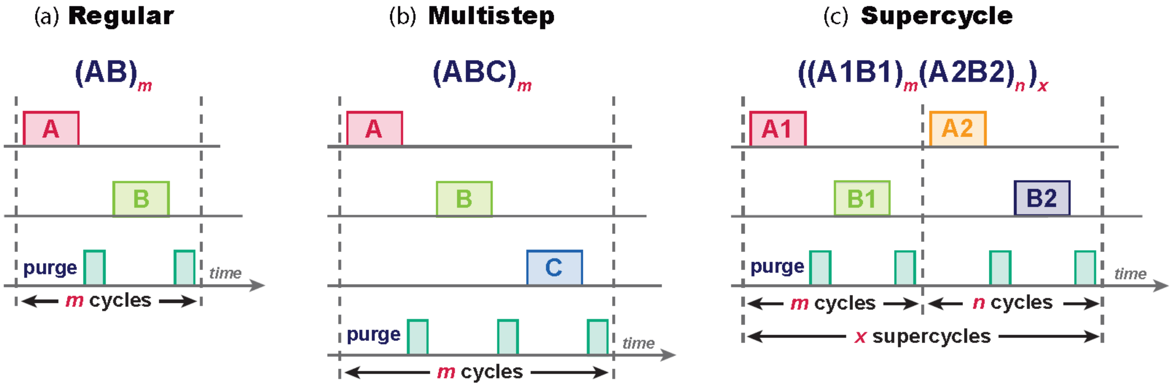

Figure 1.8. *A schematic representation of the various steps in (a) a regular ALD process, (b) a multi-step process and (c) a supercycle. In a multi-step process one or more additional steps are added in the ALD cycle to form for instance an ABC process. In a supercycle, the steps of two normal ALD processes are combined into m cycles of the first process and, subsequently, n cycles of the second process. The variables m and n can be chosen so as to obtain the desired composition and structure of the film.*

Box 4: ALD for gas sensor improvement

Because of their low cost and high sensitivity, metal oxide based gas sensors (see Box 2) show great promise for application in autonomous ultralow power sensing solutions (20). The main challenge in realizing such devices is the relatively high power consumption of MO gas sensors: optimal sensor performance requires a heating element close to the active sensing layer. The extra power consumption needed is in the order of several mW, and too high for application in wireless autonomous network systems which operate preferably at ~100 µW. Therefore, in order to reduce power consumption, the sensitivity of these devices needs to be increased, preferably such that room temperature (RT) operation becomes possible.

It is here that the potential of ALD can be exploited to the fullest extent to improve the design of a metal oxide gas sensing device. The possibilities are depicted schematically in Figure 1.9. The sensitivity of the sensing layer can be increased by increasing its *surface-to-volume*-ratio, e.g. by making use of thin-films, where the thickness of the sensing layer can be controlled precisely using ALD (Figure 1.9 (a)). By doping the metal oxide layer, a beneficial change in the conductivity of the layer can be achieved, further improving sensor performance (Figure 1.9 (b)). The interaction between the gas and the sensing layer can be further improved by adding nanoparticles of a catalytic material to the surface using ALD (Figure 1.9 (c)). The surface-to-volume ratio can be further improved by depositing the sensing layer on a high aspect ratio nanostructured substrate (Figure 1.9 (d)). Remarkably, ALD can be used to combine all four approaches for sensor improvement to obtain optimal sensor performance (Figure 1.9 (e)).

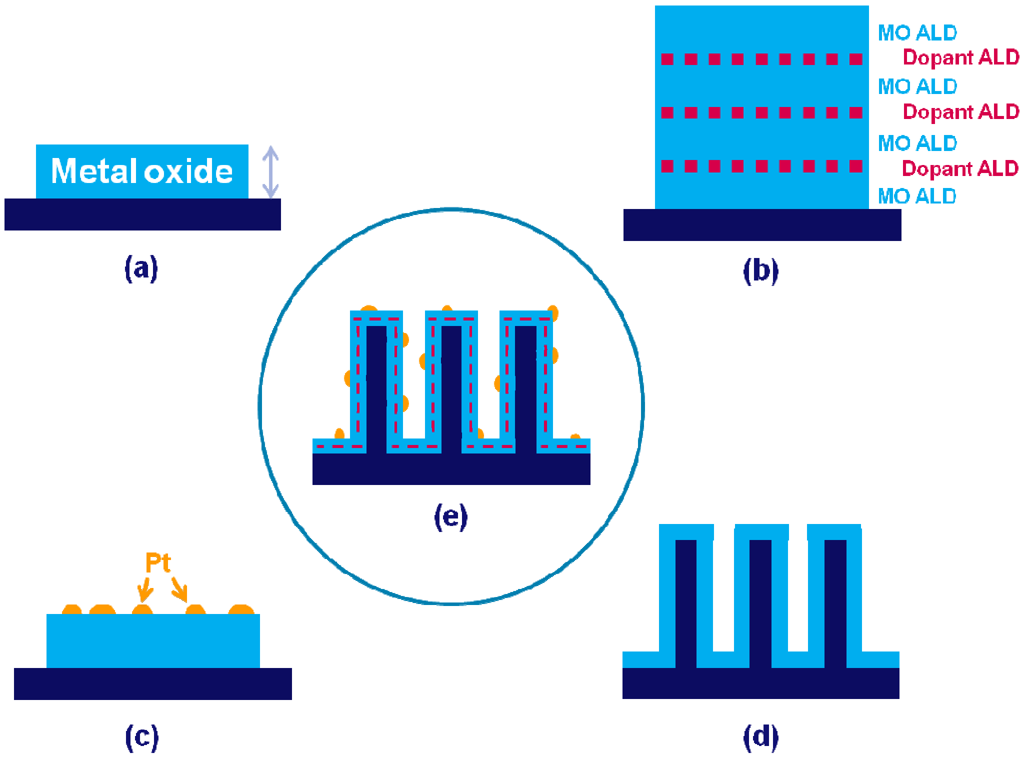

Figure 1.9. *Schematic representation of possible options offered by ALD to improve gas sensing devices. (a) By making use of thin film MO layers, the surface-to-volume-ratio can be improved. (b) By doping the metal oxide layer, a beneficial change in the conductivity of the layer can be achieved. (c) The interaction between the gas and the sensing layer can be further improved by adding nanoparticles of a catalytic material to the surface. (d) The surface-to-volume ratio can be improved by depositing the sensing layer on a high aspect ratio nanostructured substrate. (e) ALD can be used to combine all four approaches for sensor improvement.*

ALD of platinum and platinum oxide

The increasing demand for creative deposition solutions requires a continuous expansion of the capabilities of ALD both in terms of materials and concepts. This creates an ever growing need for in-depth fundamental understanding of ALD processes. An example of how such understanding can lead to novel deposition approaches can be found in ALD of Pt. Because of its high work function and low resistivity Pt is often used as an electrode material, and Pt is applied extensively as a catalyst.

Over the years, several Pt ALD processes have been developed, each with a different combination of precursors and reactants (21-23). The most adopted one has become the thermal ALD process using (MeCp)PtMe$_3$ and O$_2$ gas. Alternatively, ALD of Pt using (MeCp)PtMe$_3$ can also be carried out using O$_2$ plasma rather than O$_2$ gas. Both processes have been studied extensively and the insights that were gained have led to novel approaches for the deposition of platinum. Insights into the reaction mechanism of ALD of Pt have led to the development of an 'ABC'-type ALD process for the deposition of Pt at temperatures as low as room temperature (24). Furthermore, insights into the nucleation behavior led to the conclusion that by controlling the O$_2$ pressure, the growth of Pt can be made area-selective (25). ALD of Pt (and other noble metals such as Pd) also offers the possibility to deposit nanoparticles as well as thin films. By combining area-selective ALD with the ability of the Pt ALD process to deposit nanoparticles, core/shell nanoparticles can be deposited (26).

The advancements gained by the detailed studies of the Pt ALD process so far, call for further study of this process for the continued expansion of the ALD toolbox (25-28). For example, the process using (MeCp)PtMe$_3$ and O$_2$ plasma can be used for the deposition of PtO$_x$ as well as Pt, although this potential has never been fully explored. Furthermore, the challenges faced in plasma-assisted ALD of Pt and PtO$_x$ on demanding 3D surface topologies require extensive investigation. In this thesis, we therefore focus on gaining a better understanding of ALD of Pt and PtO$_x$ with the aim to create more processing opportunities for MtM applications. An example of how novel ALD approaches can be used for MtM devices is given in box 4, where design improvements for a metal oxide gas sensor using ALD are described. This example encompasses the motivation for this thesis work.

Outline of this Thesis

The main goal of this work has been to gain a better understanding of plasma-assisted ALD of Pt and PtO_x, and to use this understanding to explore possible practical applications. In Chapter 2, ALD of Pt is discussed in more detail, including the general reaction mechanisms and an overview of the state-of-the-art in ALD of Pt.

In Chapter 3, one of the most fundamental aspects of ALD is discussed: the particle dose. In order to achieve saturation of the self-limiting half-reactions in ALD, the appropriate precursor and reactant doses need to be delivered to the surface. The influence of the sticking probability on the precursor and O_2 plasma doses will be discussed in Chapter 3. The sticking probability of the $(MeCp)PtMe_3$ precursor will also be determined experimentally.

Chapter 4 deals with several remaining questions concerning the deposition of Pt at lower temperatures. One of the main reasons for using plasma-assisted ALD of Pt is to further reduce the lower limit of the temperature window (250-300 °C) of the conventional thermal process, by using $(MeCp)PtMe_3$ and O_2 plasma. During the $(MeCp)PtMe_3$ pulse, methane has been reported as a volatile reaction product, in addition to combustion-like reaction products (CO_2 and H_2O). In this chapter, experimental data based on both thermal and plasma-assisted ALD will be presented and corroborated using the results from surface science literature. The main questions that will be addressed concern the inhibited growth at lower temperatures, and the type of surface reactions that can lead to the production of methane in Pt ALD.

A major challenge for plasma-assisted ALD is achieving good conformality in high aspect ratio (HAR) structures because of the surface recombination of plasma radicals. For example, O-radicals from the gas phase can recombine with surface O-atoms to form molecular oxygen. Once these O-radicals have recombined they can no longer contribute to the ALD surface reactions as radicals. In Chapter 5, ALD in HAR structures is discussed in more detail. Insights into particle dosing are used to ensure good conformality of Pt films in HAR trenches. The thickness profiles of these films are determined and the obtained conformality will be analyzed.

Remarkably, the plasma-assisted ALD process using (MeCp)PtMe$_3$ and O$_2$ plasma can be used to deposit both Pt and PtO$_x$. Due to the relatively high resistance of Pt against oxidation, the deposition of PtO$_x$ is not trivial. The composition of the deposited material can be influenced by increasing either the precursor or the reactant dose beyond the dose required for saturation. In Chapter 6 we demonstrate how by accurate dosing of the precursor and O$_2$ plasma dosing accurate control over the composition of the deposited material can be achieved, with the ability to deposit both metallic Pt and PtO$_x$. The process window is discussed, the material properties of the deposited films are presented and the nucleation behavior and reaction mechanisms are elucidated.

In Chapter 7, the consequences for the deposition of Pt and/or PtO$_x$ inside HAR trenches are examined. We demonstrate how understanding and controlling particle doses can lead to the simultaneous deposition of both Pt and PtO$_x$ inside single trenches with control over the composition profile.

In Chapter 8, an example is given of how ALD with its unique features can contribute to and improve the nanomanufacturing of sensing devices. Such advanced devices have the potential of detecting low levels (down to ppm) of O$_2$ and CO concentrations at low temperatures (down to room temperature). Thus, an ALD-enabled design of a gas sensing device is presented which utilizes many of the unique features of ALD. In this chapter ALD is used to deposit a thin-film ZnO sensing layer, and to dope this layer with Al. Furthermore, plasma-assisted ALD is used to deposit Pt-nanoparticles which catalytically enhance the sensitivity of the Al-doped ZnO layer. The sensing performance of such a sensing device is also discussed.

In Chapter 9, summarizing conclusions are given alongside several recommendations and outlook for future research.

Bibliography

1. O. Sneh, R. B. Clark-Phelps, A. R. Londergan, J. Winkler, and T. E. Seidel, *Thin Solid Films* **402**, 248 (2002).
2. International technology roadmap for semiconductors, *2009 edition, www. itrs.net.* (2009).
3. A. J. M. Mackus, S. B. S. Heil, E. Langereis, H. C. M. Knoops, M. C. M. van de Sanden, and W. M. M. Kessels, *J. Vac. Sci. Technol. A* **28**, 77 (2010).
4. R. L. Puurunen, *J. Appl. Phys.* **97**, 121301 (2005).
5. G.Eranna, *Metal Oxide Nanostructures as Gas Sensing Devices* (CRC Press, Boca Raton, 2012).
6. K. M. Sancier, *J. Catal.* **9**, 331 (1967).
7. M. E. Franke, T. J. Koplin, and U. Simon, *Small* **2**, 36 (2006).
8. C. Cantalini, M. Post, D. Buso, A. Guglielmi, and A. Martucci, *Sensors and Actuators B-Chemical* **108**, 184 (2005).
9. Y. N. Xia, P. D. Yang, Y. G. Sun, Y. Y. Wu, B. Mayers, B. Gates, Y. D. Yin, F. Kim, and Y. Q. Yan, *Adv. Mater.* **15**, 353 (2003).
10. V. Dam, M. Blauw, S. Brongersma, and M. Crego-Calama, *EUROSENSORS XXIV CONFERENCE* **5**, 172 (2010).
11. I. Eisele, T. Doll, and M. Burgmair, *Sensors and Actuators B-Chemical* **78**, 19 (2001).
12. International technology roadmap for semiconductors, *2011 edition executive summary, www. itrs. net.* (2011).
13. N. Fu, X. Xiao, X. Zhou, J. Zhang, and Y. Lin, *J. Phys. Chem. C* **116**, 2850 (2012).
14. M. L. Toebes, J. A. van Dillen, and Y. P. de Jong, *Journal of Molecular Catalysis A-Chemical* **173**, 75 (2001).
15. K. Chiang, C. C. Huang, G. Chen, W. J. Chen, H. Kao, Y. H. Wu, A. Chin, and S. P. McAlister, *IEEE Trans. Electron Devices* **53**, 2312 (2006).
16. T. Harigai, H. Adachi, and E. Fujii, *J. Appl. Phys.* **107**, 096101 (2010).
17. Y. Wu, S. Potts, P. Hermkens, H. Knoops, F. Roozeboom, and W. Kessels, *Chem. Mater.* **25**, 4619 (2013).
18. N. Colaneri, *Solid State Technol.* **56**, 13 (2013).
19. V. Miikkulainen, M. Leskelä, M. Ritala, and R. L. Puurunen, *J. Appl. Phys.* **113**, 021301 (2013).
20. M. Suchea, S. Christoulakis, K. Moschovis, N. Katsarakis, and G. Kiriakidis, *Thin Solid Films* **515**, 551 (2006).

21. M. Utriainen, M. Kröger-Laukkanen, L. S. Johansson, and L. Niinistö, *Appl. Surf. Sci.* **157**, 151 (2000).
22. J. Hämäläinen, F. Munnik, M. Ritala, and M. Leskelä, *Chem. Mater.* **20**, 6840 (2008).
23. H. C. M. Knoops, A. J. M. Mackus, M. E. Donders, M. C. M. van de Sanden, P. H. L. Notten, and W. M. M. Kessels, *Electrochem. Solid-State Lett.* **12**, G34 (2009).
24. A. J. M. Mackus, D. Garcia-Alonso, H. C. M. Knoops, A. A. Bol, and W. M. M. Kessels, *Chem. Mater.* **25**, 1769 (2013).
25. A. Mackus, N. Thissen, J. Mulders, P. Trompenaars, M. Verheijen, A. Bol, and W. M. M. Kessels, *J. Phys. Chem. C* **117**, 10788 (2013).
26. M. J. Weber, A. J. Mackus, M. A. Verheijen, C. van der Marel, and W. M. M. Kessels, *Chem. Mater.* **24**, 2973 (2012).
27. A. Mackus, S. Dielissen, J. Mulders, and W. M. M. Kessels, *Nanoscale* **4**, 4477 (2012).
28. S. T. Christensen and J. W. Elam, *Chem. Mater.* **22**, 2517 (2010).

Chapter 2

Atomic layer deposition of platinum and platinum oxide

Platinum and platinum oxides

Platinum ranks amongst the most versatile and the most expensive transition metals. About 2/3 of the worldwide supply of platinum is consumed for catalytic applications in environmental and energy-related areas and for 1/3 it is used in jewelry. Platinum is a noble metal, which means that it maintains its chemical stability in oxidizing atmospheres. Furthermore, platinum can catalyze the breaking of C-H, O-O, and H-H bonds into species that interact with and adsorb on its surface, thereby promoting their conversion into other species by oxidation-reduction reactions (1). Therefore, Pt is widely applied as a catalytic material in many commercial thermochemical, electrochemical and photochemical conversion processes (2). It is used as a catalyst, usually as metal nanoparticles dispersed on high-surface-area supports, in the chemical and petroleum industry, e.g. in catalytic reforming of naphtha feedstocks into higher-octane gasoline and in automotive three-way catalyst systems for conversion of NO_x, CO, and hydrocarbons into nitrogen gas, CO_2 and H_2O (3).

Platinum is also increasingly considered for application in future generation electronics because it has excellent electrical properties with a high work function of 5.6 eV and a low resistivity of 10.5 μΩ·cm. Pt is therefore considered as electrode or contact material in nano-electronics (4,5), and is considered for example in dye-sensitized solar cells (6).

Due to its high chemical inertness in oxidizing ambients, Pt has a strong resistance against oxidation (7,8). Nonetheless, stable forms of platinum oxide (PtO_x) do exist although these oxides have not been characterized as extensively as Pt. Several properties of platinum and platinum oxides are given in Table I. In general, platinum oxide exists in several crystalline stoichiometric compositions, namely PtO (9,10), (α- and β- phase) PtO_2 (11,12), Pt_3O_4 (13), Pt_2O (10), PtO_3 (14,15), and $PtO_2{\cdot}H_2O$ (16). Furthermore, amorphous films with chemical composition PtO_x have been reported, where 1<x<2.1, and which are considered to be a homogeneous solid solution of PtO and PtO_2 (17). The reported crystal structures of some of the crystalline platinum oxides are shown in Figure 2.1. Depending on its stoichiometric form, PtO_x can have applications in catalysis, microelectronics, or sensing (9,18,19). PtO_2 is often employed in catalysis (20-24), where PtO_2 has been shown to have an increased selectivity towards the catalytic oxidation of CO (23). Nano-dispersed PtO has been shown to catalytically enhance the performance of metal oxide-based gas sensors (25). The ability of PtO_x films to reduce relatively easily into (porous) platinum makes it a promising material for application in e.g. optical data storage or for thermal lithography (18,26-28). The resistivity of PtO_x films increases with increasing O/Pt ratio, and PtO_x is reported to be semiconducting as well as insulating for higher and lower oxygen concentrations, respectively (9,29,30).

Since Pt is a precious metal, Pt and PtO_x are expensive materials and should therefore be utilized as efficiently as possible. For many applications it is not necessary to have a large amount of material and thin films or even nanoparticles of Pt or PtO_x suffice (31,32). Noble metal nanoparticles for example, can be applied for heterogeneous catalysis (33,34) in applications such as hydrogen storage (35), sensing (36), and automotive emissions catalytic conversion (37).

Thin films of Pt can be deposited using e.g. reactive sputtering, electrodeposition, electroless deposition, or impregnation (38,39). Generally, PtO_x films are deposited by means of reactive sputtering (12,30,40), or through O_2 plasma treatment of Pt films (11,41). The production of supported metallic nanoparticles can be achieved through several wet chemistry techniques such as impregnation, deposition-precipitation, galvanic displacements, colloidal synthesis, and ion exchange processes (42,43). One of the main drawbacks of these wet chemistry and sputter techniques for use in future applications is the limited thickness control and the limited conformality that can be reached on 3D topologies.

Atomic layer deposition (ALD) is a good alternative to wet chemistry and sputter techniques because it allows for the deposition of Pt thin films and nanoparticles with excellent conformality in demanding 3D structures (44). Furthermore, it offers high material quality: O, C, and H contaminations are generally reported to be <1 atom % (45). It also offers high uniformity with a surface roughness in the order of 1 nm, and excellent thickness control with a growth per cycle of approximately 0.045 nm (29). As a result, Pt ALD has been considered for a wide variety of potential applications in the field of microelectronics and catalysis (5,32,46-48). Recently, it has been shown that PtO_x can also be deposited using ALD (9,29).

Table I. *Properties of platinum and the most common platinum oxides. Note: the temperature indications of PtO and PtO_2 are thermal decomposition temperatures. Literature references are given in parentheses.*

	Density (g cm^{-3})	**Resistivity (μΩ cm)**	**Melting point (°C)**
Pt	21.5	10.5	1768
PtO	-	$2 \cdot 10^6$ (9) 10^3 (30)	325
PtO_2	10 (29)	$>10^8$ (29) 10^6 (30)	300-400 in vacuum 550-650 in air (30,49,50)

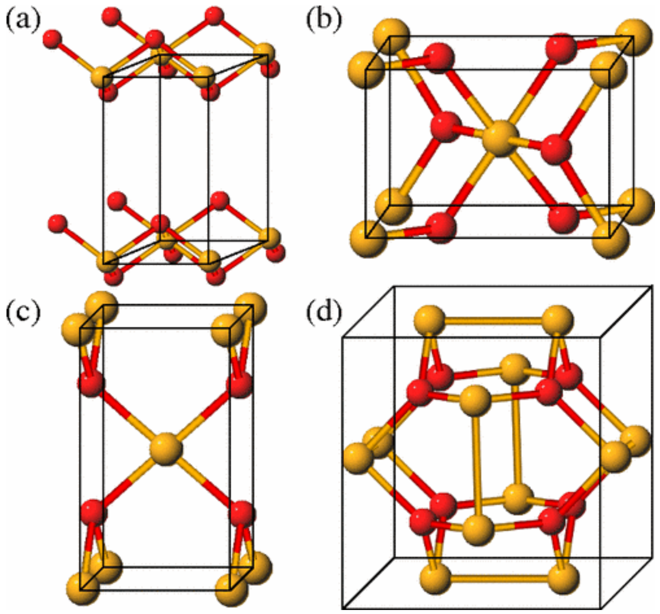

Figure 2.1. *Crystal structures reported for some platinum oxides: (a) α- PtO_2, (b) β-PtO_2, (c) PtO*, and (d) Pt_3O_4 (51). Pt atoms are indicated in orange (bright), and O atoms indicated in red (dark). Unit cells are indicated by the boxes.*

**A cubic form of PtO has also been reported (10).*

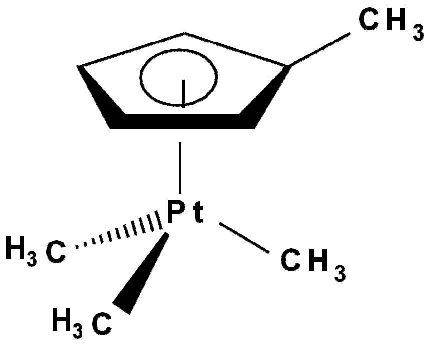

Figure 2.2. *Schematic representation of the (MeCp)$PtMe_3$ precursor.*

Atomic layer deposition of platinum

The first ALD process for Pt was based on (MeCp)$PtMe_3$ (see Figure 2.2) and was introduced 2003 by Aaltonen *et al.* (44). The process was inspired by similar Pt chemical vapor deposition (CVD) processes. (MeCp)$PtMe_3$ is a widely studied CVD precursor because of its low melting point of 30 °C and high volatility (52), and has been used in combination with H_2 (52) and O_2

(53). Other Pt CVD precursors are $CpPtMe_3$ (54), $Pt(acac)_2$ (55), and $Pt(hfac)_2$ (56).

Table II gives an overview of the precursors and co-reactants that have been used for ALD of Pt to date. As shown, ALD of Pt still relies nearly exclusively on the $(MeCp)PtMe_3$ precursor (44,45). A process based on $Pt(acac)_2$ has also been developed, but this precursor shows a limited thermal stability (9). The limited variety in Pt ALD precursors is remarkable given the importance of the Pt ALD process (because of its wide range of applications) and the much greater variety in available precursors for other noble metal ALD processes, e.g. for Ru (57-60) and Ir (61-65). An explanation for the lack of other Pt ALD precursors could be the robustness of the process based on $(MeCp)PtMe_3$, which does not stimulate the development of processes based on new precursors despite the relatively high cost of $(MeCp)PtMe_3$ (45).

Table II. *Overview of ALD processes for Pt deposition reported in the literature. The deposition temperature represents the temperature range over which a growth-per-cycle of at least 0.04 nm per cycle was achieved.*

Metal precursor	**Co-Reactant**	**Deposition temperature**	**Reference**
$(MeCp)PtMe_3$	O_2	250-300	(5,29,32,46,47,66-73)
$(MeCp)PtMe_3$	air	300-310	(44,74)
$(MeCp)PtMe_3$	NH_3 plasma	250-300	(75)
$(MeCp)PtMe_3$	N_2 plasma	250-300	(75)
$(MeCp)PtMe_3$	O_2 plasma (+ H_2)*	30-300	(29,67,76-78)
$(MeCp)PtMe_3$	O_3	100-300	(79)
$Pt(acac)_2$	$O_3 + H_2$	120-130	(80)
$Pt(acac)_2$	O_3	140-200	(9)

* *H_2 gas is used at lower substrate temperatures to reduce PtO_x into metallic Pt (29,76).*

As shown in Table II, the majority of the reports on ALD of Pt using (MeCp)PtMe$_3$ make use of O_2 gas or air as the co-reactant. This popular Pt ALD process has a temperature window ranging from approximately 250-300 °C. By making use of O_3 as a co-reactant, the lower limit of the temperature window can be lowered to 100 °C (79). The plasma-assisted ALD process using O_2 plasma can be used to deposit thin films of Pt at deposition temperatures as low as room temperature (76). For applications for which oxidation of the substrate is undesirable, processes have been developed using NH_3 plasma, or N_2 plasma as co-reactant (75).

Reaction mechanism of ALD of Pt based on (MeCp)PtMe$_3$ and O_2 gas

The growth mechanism for Pt ALD based on (MeCp)PtMe$_3$ and O_2 gas has been studied quite extensively. This mechanism is different from the more general Al_2O_3 case as described in Chapter 1, box 1. First of all, during Pt ALD a metal film containing only a single element is deposited. Secondly, the deposited Pt film has the ability to catalyze the breaking of the C-H bonds of the precursor ligands and the O-O bonds in O_2 which has consequences for the reaction mechanism as described below (67).

Aaltonen *et al.* first proposed a possible reaction mechanism based on that of the corresponding CVD process (44,66). During the O_2 half-reaction, the Pt surface catalyzes the dissociation of O_2 molecules, generating a surface that is covered by chemisorbed oxygen. At the beginning of the (MeCp)PtMe$_3$ pulse, the precursor ligands undergo combustion reactions with the adsorbed oxygen, resulting in CO_2 and H_2O and possibly other reaction products. Because of the limited amount of adsorbed oxygen however, the precursor ligands are not completely oxidized. The remaining hydrocarbon species are then oxidized during the subsequent O_2 step, during which O_2 dissociates at the Pt surface and a new chemisorbed oxygen layer is formed. The formation of CO_2 and H_2O was confirmed by in situ mass spectrometry, which showed that the majority of the precursor carbon is released during the O_2 step (66,73).

The reaction mechanism was further elucidated when the formation of CH_4 during the precursor pulse was detected in a gas phase infrared (FTIR) spectroscopy study by Kessels *et al.* (72), and later confirmed by mass spectrometry studies (68,73). Saturation of the surface reactions was ascribed to the limited supply of surface oxide species following the O_2 pulse (72,81).

Based on these observations and results from surface science studies, Mackus *et al.* proposed a refined reaction mechanism, taking into account the catalytic nature of Pt described extensively in surface science literature (67). According to this mechanism, schematically depicted in Figure 2.3, the (MeCp)$PtMe_3$ precursor is unstable on the Pt surface at the typical Pt ALD temperature of 300 °C. During the (MeCp)$PtMe_3$ pulse, the precursor ligands are catalytically combusted by the surface O forming CO_2 and H_2O as proposed by Aaltonen *et al.* Once the O becomes depleted, the reaction proceeds via dehydrogenation and hydrogenation, and subsequent desorption of CH_4 (and possibly other hydrocarbon species), until a carbonaceous layer forms that prevents further surface ligand decomposition reactions and precursor adsorption (67). The saturation of the (MeCp)$PtMe_3$ half-reaction is therefore caused by the poisoning of the surface by dehydrogenation products in the form of this carbonaceous layer. Using in vacuo photoemission spectroscopy, Geyer *et al.* observed significant amounts of carbonaceous species following the Pt precursor pulse, which points towards the mechanism proposed by Mackus *et al.* During the O_2 pulse, O_2 dissociates at the Pt surface and the carbonaceous layer is combusted to CO_2 and H_2O and a new layer of adsorbed O atoms forms before the start of the ensuing cycle.

Together, the precursor, purge, oxygen, and additional purge step constitute one ALD cycle during which approximately 0.045 nm of Pt is deposited at the substrate temperature of 300 °C (i.e. $3 \cdot 10^{14}$ atoms cm^{-2} per cycle). By controlling the number of ALD cycles the targeted thickness can be reached, giving ALD its precise thickness control.

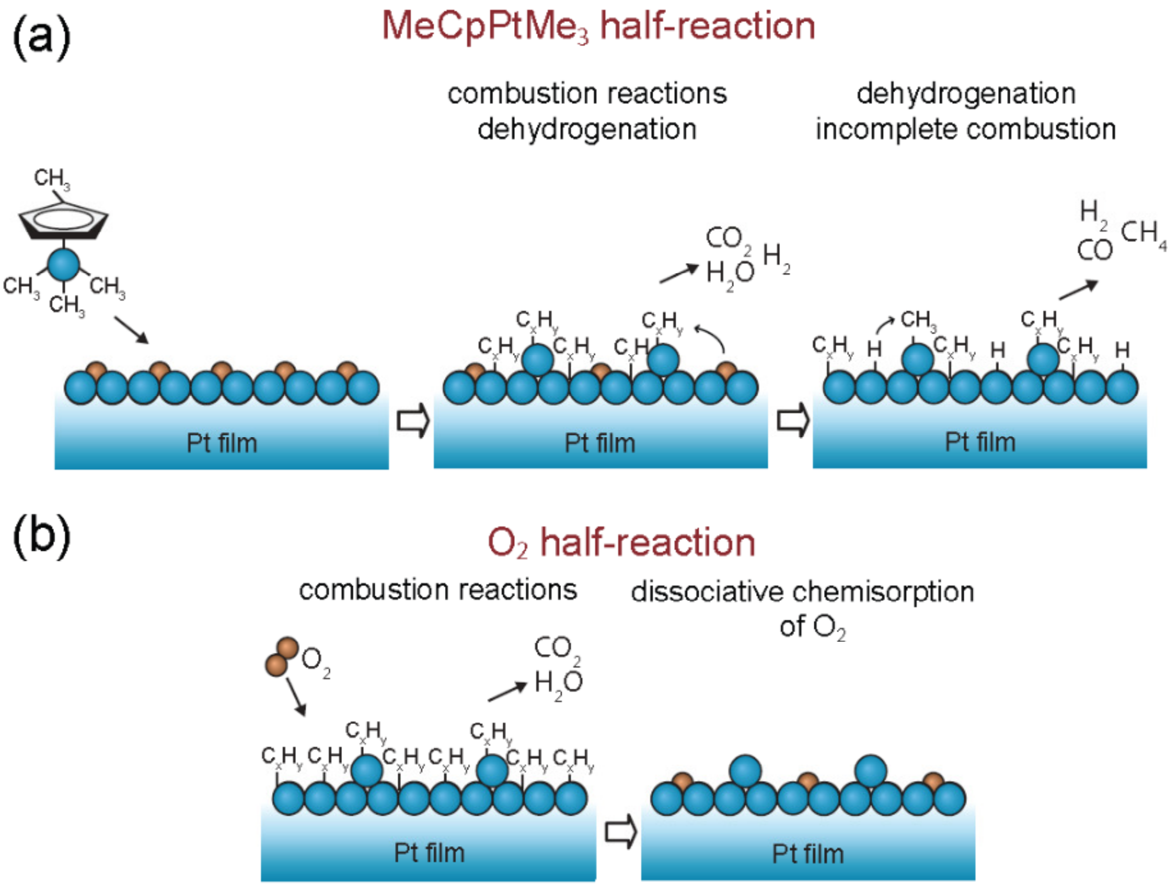

Figure 2.3. *Schematic representation of the reaction mechanism during ALD of Pt, proposed by Mackus et al. (67). (a) At the onset of the (MeCp)PtMe*$_3$ *half-reaction the surface is covered with O atoms. The (MeCp)PtMe*$_3$ *molecules undergo combustion and dehydrogenation reactions upon adsorption on the Pt surface, resulting predominantly in* CO_2 *and* H_2O *reaction products. Once the O becomes depleted, the reactions continue with dehydrogenation and incomplete oxidation, which leads to* H_2*, CO, and* CH_4*, among other hydrogenation products. (b) During the* O_2 *pulse, the carbonaceous layer formed in the (MeCp)PtMe*$_3$ *pulse is combusted, and* O_2 *dissociatively chemisorbs at the surface providing surface-bound oxygen for the next ALD cycle.*

Temperature window

The temperature window of the thermal ALD process based on (MeCp)PtMe$_3$ and O$_2$ gas spans from ~250 to 300 °C. Above 300 °C, the precursor starts to show signs of thermal decomposition. Below 250 °C, the GPC rapidly drops to approximately 0.010 nm at 200 °C, and below 200 °C no thermal ALD growth is reported for this process (82). The inhibition of growth below 200 °C has been ascribed to the carbonaceous layer that is formed by dehydrogenation products of the precursor ligands during the precursor step. At lower temperatures, this carbonaceous layer prevents the dissociative chemisorption of O$_2$ molecules during the O$_2$ pulse (68).

Nucleation

For ALD of noble metals, nucleation on oxide surfaces is generally challenging and ALD growth often shows a relatively long nucleation delay (29,77,83,84). For ALD of Pt based on (MeCp)PtMe$_3$ and O$_2$, the nucleation behavior on oxide substrates is strongly dependent on the O$_2$ exposure, as shown in figure 2.4. In this figure, the dependence of Pt ALD growth on the O$_2$ exposure is plotted (85). For O$_2$ exposures below ~50 mTorr (0.067 mbar) no growth takes place on Al$_2$O$_3$. On a Pt surface however, the growth starts at O$_2$ pressures as low as 2 mTorr. For low O$_2$ exposures, the nucleation of Pt on oxide substrates is difficult to achieve using thermal ALD due to the absence of catalytic Pt-clusters that facilitate O$_2$ dissociation during the initial cycles (85). Although precursor adsorption on a bare oxide substrate is probably not the limiting factor, this only results in the deposition of single Pt precursor fragments, which are not catalytically active enough for efficient O$_2$ dissociation.

Mackus *et al.* showed that sufficient exposure to an oxidizing agent facilitates the diffusion of these Pt atoms over the oxide surface, leading to the growth of Pt islands (see also Figure 2.5) (85). Once these Pt nanoparticles have formed, mediated by the presence of an oxidizing agent, O$_2$ dissociation and *spill-over* of O atoms can occur more effectively which in turn facilitates island growth (77). These islands grow and coalesce to eventually form a closed layer. For Pt, a fully closed film is typically not obtained until a film thickness of at least 8 nm is reached (77). A similar O$_2$ pressure dependent nucleation behavior was also observed for ALD of Ru from CpRu(CO)$_2$Et and O$_2$ gas (86). The dependence of Pt ALD growth on O$_2$

exposure defines a regime in the O_2 pressure for which the growth is area-selective on Pt seed layer patterns (87).

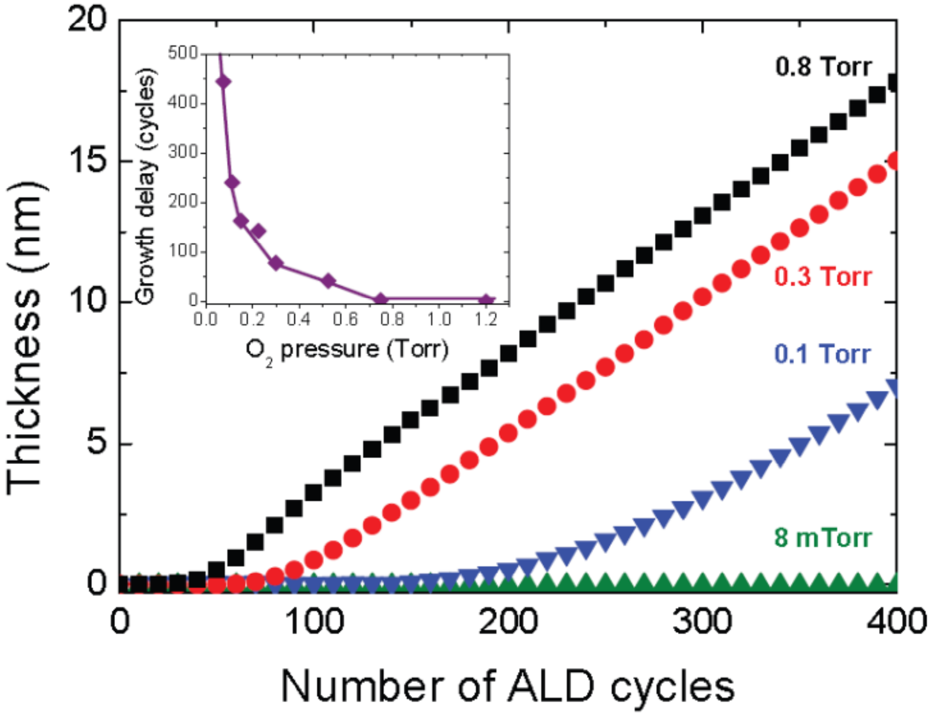

Figure 2.4. *Thickness as a function of the number of cycles for Pt ALD on Al_2O_3 substrate as measured by in situ spectroscopic ellipsometry (SE) using different O_2 pressures and a 10 s pulse time. In the inset the growth delay deduced from the nucleation curves is presented as a function of the O_2 pressure (85).*

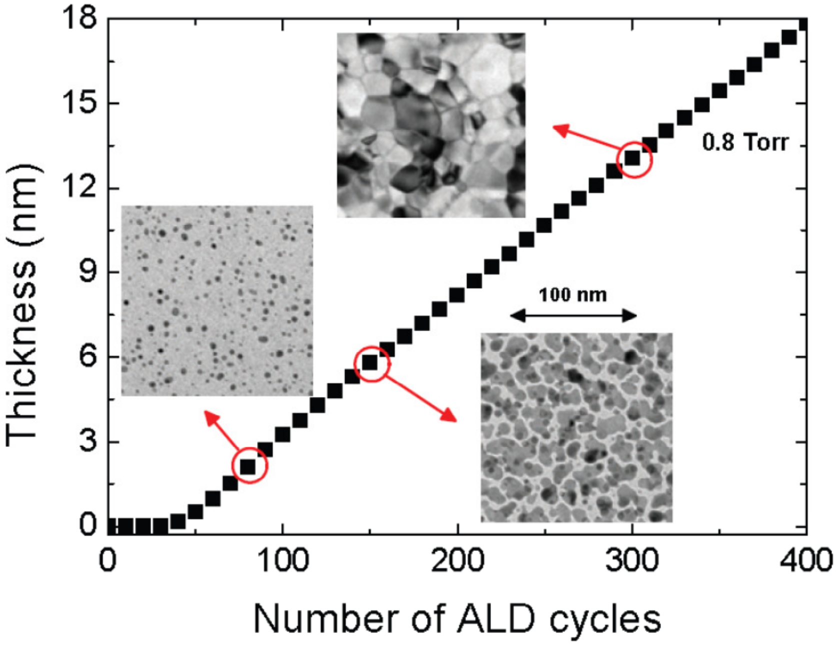

Figure 2.5. *Thickness as a function of the number of cycles for Pt ALD on* Al_2O_3 *as measured by in situ spectroscopic ellipsometry (SE) using an* O_2 *exposure of 0.8 Torr* O_2 *for 10 s. The bright field TEM images in the figure illustrate that Pt ALD nucleation evolves from island growth, via island coalescence, to film closure. A scale bar is given for the TEM images (85).*

Plasma-assisted ALD of Pt and PtO_x

In the Pt ALD process using $(MeCp)PtMe_3$, the thermal O_2 gas exposure can also be replaced by an O_2 plasma exposure (29). The reactive and energetic species produced in the plasma offer several benefits for the deposition of Pt using ALD (88). In an O_2 plasma, reactive O-radicals are supplied from the gas phase and there is no need to first dissociate the O_2 at the surface in order to participate in surface reactions. This means that the carbonaceous layer formed by the precursor ligands can be combusted at much lower temperatures. It has been recently reported by our group that Pt can be deposited at room temperature by a 3-step ABC-type (see chapter 1, box 3) plasma-assisted ALD process comprising $(MeCp)PtMe_3$ precursor, O_2 plasma, and H_2 gas/plasma pulses (76). The H_2 pulses are required to counteract the oxidation of the film by the O_2 plasma which readily takes place at low temperatures, such that the deposition of Pt is ensured. Using this process, Pt can be deposited at room temperature on various temperature-sensitive materials such as polymers, paper, and textile (76).

Other advantages of plasma-assisted ALD of Pt are its fast nucleation on oxide surfaces (77) and the ability to deposit PtO_x as well as metallic Pt (29). In 2008, Hämäläinen *et al.* were the first to report on an ALD process for PtO, which made use of $Pt(acac)_2$ and O_3. Although O_3 proved reactive enough to form PtO, higher oxidation states (PtO_2) were not reached, and the temperature window for this process ranged from 120-130°C. In 2009, Knoops *et al.* first showed that for sufficiently long O_2 plasma exposures, $PtO_{2.4}$ could be deposited in a temperature range from 100-300°C (29). A detailed investigation of the PtO_x process was beyond the scope of the work of Knoops *et al.* at that time. The very limited insights into the PtO_x process window and reaction mechanism formed a large part of the motivation for a detailed investigation of ALD of PtO_x in this thesis. For example, the nucleation behavior of ALD of PtO_x with possible nanoparticle formation had never been examined, and the ability to deposit thin films of PtO_x conformally in high aspect ratio 3D structures had never been demonstrated.

Extending conventional ALD

The typical nucleation behavior of ALD of Pt has led to several innovative applications of this process. For example, the formation of Pt islands during the nucleation stage has been exploited to deposit Pt nanoparticles for applications in sensing and catalysis (48,89-94). Furthermore, by combining the possibility to deposit nanoparticles with area-selective growth, ALD can be used for the deposition of multi-metallic core/shell nanoparticles (32,95). Due to the lattice strain created in these core/shell nanoparticles and the heterometallic bonding interactions, the surface electronic properties of the nanoparticles are modified. Therefore, core/shell nanoparticles often show improved catalytic properties compared to their alloyed counterparts or to mixtures of monometallic nanoparticles (95).

Recently, area-selective ALD growth has enabled a novel approach which combines the benefits of ALD with those of electron beam induced deposition (EBID) (71,87). EBID enables direct-write patterning of metallic structures with sub-10 nm lateral resolution (96,97). One of the most important advantages of EBID is that the pattern is written directly and only at locations where it is desired, which limits the number of processing steps and eliminates the use of resists or lift-off steps. One of the main drawbacks of EBID of Pt is the poor material quality with high carbon contamination (87). By combining EBID with ALD, the best of both worlds can be obtained; the nanoscale patterning capability of EBID and the material quality and thickness control of ALD.

ALD of Pt can be used in super-cycles (see Chapter 1, box 3) with other noble metal ALD processes to obtain bimetallic structures or even alloys. The use of ALD of Pt has been reported in combination with iridium (47,73), ruthenium (93), and palladium (32). The study of e.g. Ir-Pt films showed that both the Ir and Pt ALD processes are unaffected by the presence of the other metal (73). Remarkably, by employing super-cycles of Ir and Pt ALD, alloy films have been deposited rather than a laminate structure, and a specific film composition can be achieved by adjusting the ratio between the two processes.

ALD of Pt in high aspect ratio structures

Nanostructured metal films with large specific surface areas have found extensive use in a variety of fields including catalysis, sensing, and energy storage (47,98-101). Conventional approaches for synthesizing such films (e.g. electrodeposition with arrays of nanotubes) suffer from a limited control over film composition and thickness. The ALD process using (MeCp)PtMe$_3$ and O$_2$ gas has been used to deposit highly conformal Pt films in high aspect ratio features with aspect ratios over 100 (47,70). This makes ALD of Pt the ideal technique to deposit Pt thin films and nanoparticles for many future applications.

For example, ALD of Pt has been used to create nanostructured films by using anodized aluminum oxide (AAO) as a template, and the potential of these films for electrochemical sensing applications has been demonstrated by the non-enzymatic sensing of glucose (47). Furthermore, Pt nanoparticle catalysts have been deposited using ALD on silicon nanowires for solar hydrogen generation, where ALD showed favorable results compared to conventional techniques (99). A combination of Pt and Al$_2$O$_3$ ALD in AAO has also been reported to form a metal-insulator-electrolyte system, possibly enabling field effect control of the nanofluidic properties of a membrane.

ALD of Pt has furthermore been investigated as a means to deposit contacts on carbon nanotubes (5,90,102-104).

To the best of our knowledge, plasma-assisted ALD using (MeCp)PtMe$_3$ and O$_2$ plasma has not been reported for deposition in high aspect ratio structures. This may be due to the perceived challenges concerning the surface recombination of the O-radicals (105). The advantages of plasma-assisted ALD concerning fast nucleation and lower deposition temperatures formed the inspiration to study the high aspect ratio potential of this process, discussed in Chapter 5 and 7. The deposition of PtO$_x$ inside high aspect ratio structures will be discussed in Chapters 6 and 7.

Bibliography

1. C. G. Freyschlag and R. J. Madix, *Materials Today* **14**, 134 (2011).
2. G. A. Somorjai and J. Y. Park, *Chem. Soc. Rev.* **37**, 2155 (2008).
3. R. M. Heck and R. J. Farrauto, *Applied Catalysis A-General* **221**, 443 (2001).
4. S. Conoci, S. Petralia, P. Samori, F. M. Raymo, S. Di Bella, and S. Sortino, *Advanced Functional Materials* **16**, 1425 (2006).
5. C. Liu, C. C. Wang, C. C. Kei, Y. C. Hsueh, and T. P. Perng, *Small* **5**, 1535 (2009).
6. N. Fu, X. Xiao, X. Zhou, J. Zhang, and Y. Lin, *J. Phys. Chem. C* **116**, 2850 (2012).
7. J. C. Chaston, *Platinum metals Rev.* **8**, 50 (1964).
8. J. C. Chaston, *Platinum metals Rev.* **9**, 51 (1965).
9. J. Hämäläinen, F. Munnik, M. Ritala, and M. Leskelä, *Chem. Mater.* **20**, 6840 (2008).
10. J. Kumar and R. Saxena, *Journal of the Less-Common Metals* **147**, 59 (1989).
11. J. J. Blackstock, D. R. Stewart, and Z. Li, *Applied Physics A-Materials Science & Processing* **80**, 1343 (2005).
12. J. R. Mcbride, G. W. Graham, C. R. Peters, and W. H. Weber, *J. Appl. Phys.* **69**, 1596 (1991).
13. N. Seriani, W. Pompe, and L. C. Ciacchi, *Journal of Physical Chemistry B* **110**, 14860 (2006).
14. J. S. Mayell, *J. Electrochem. Soc.* **113**, 385 (1966).
15. J. S. Mayell and S. H. Langer, *J. Electrochem. Soc.* **111**, 438 (1964).
16. Y. Gong and M. Zhou, *Chemphyschem* **11**, 1888 (2010).

17. H. Neff, S. Henkel, E. Hartmannsgruber, E. Steinbeiss, W. Michalke, K. Steenbeck, and H. G. Schmidt, *J. Appl. Phys.* **79**, 7672 (1996).
18. Q. Liu, T. Fukaya, S. Cao, C. Guo, Z. Zhang, Y. Guo, J. Wei, and J. Tominaga, *Optics Express* **16**, 213 (2008).
19. K. G. Kreider, M. J. Tarlov, and J. P. Cline, *Sensors and Actuators B-Chemical* **28**, 167 (1995).
20. A. Hamze, O. Provot, M. Alami, and J. D. Brion, *Organic Letters* **8**, 931 (2006).
21. A. Hamze, O. Provot, M. Alami, and J. D. Brion, *Organic Letters* **7**, 5625 (2005).
22. N. Sabourault, G. Mignani, A. Wagner, and C. Mioskowski, *Organic Letters* **4**, 2117 (2002).
23. M. D. Ackermann, T. M. Pedersen, B. L. M. Hendriksen, O. Robach, S. C. Bobaru, I. Popa, C. Quiros, H. Kim, B. Hammer, S. Ferrer, and J. W. M. Frenken, *Phys. Rev. Lett.* **95**, 255505 (2005).
24. S. Putzien, E. Louis, O. Nuyken, and F. E. Kuehn, *Catalysis Science & Technology* **2**, 725 (2012).
25. D. Haridas, K. Sreenivas, and V. Gupta, *Sensors and Actuators B-Chemical* **133**, 270 (2008).
26. F. Machalett, K. Gartner, K. Edinger, and M. Diegel, *J. Appl. Phys.* **93**, 9030 (2003).
27. F. Machalett, K. Edinger, M. Diegel, and K. Steenbeck, *Microelectron. Eng.* **60**, 429 (2002).
28. K. Kurihara, Y. Yamakawa, T. Nakano, and J. Tominaga, *J. Opt. A: Pure Appl. Opt.* **8**, S139 (2006).
29. H. C. M. Knoops, A. J. M. Mackus, M. E. Donders, M. C. M. van de Sanden, P. H. L. Notten, and W. M. M. Kessels, *Electrochem. Solid-State Lett.* **12**, G34 (2009).
30. Y. Abe, M. Kawamura, and K. Sasaki, *Jpn. J. Appl. Phys.* **38**, 2092 (1999).
31. M. Vukmirovic, J. Zhang, K. Sasaki, A. Nilekar, F. Uribe, M. Mavrikakis, and R. Adzic, *Electrochim. Acta* **52**, 2257 (2007).
32. M. J. Weber, A. J. Mackus, M. A. Verheijen, C. van der Marel, and W. M. M. Kessels, *Chem. Mater.* **24**, 2973 (2012).
33. D. Astruc, F. Lu, and J. R. Aranzaes, *Angewandte Chemie-International Edition* **44**, 7852 (2005).
34. M. C. Daniel and D. Astruc, *Chemical Reviews* **104**, 293 (2004).

35. M. Yamauchi, H. Kobayashi, and H. Kitagawa, *Chemphyschem* **10**, 2566 (2009).
36. S. Lal, S. Link, and N. J. Halas, *Nature Photonics* **1**, 641 (2007).
37. J. Kaspar, P. Fornasiero, and N. Hickey, *Catal. Today* **77**, 419 (2003).
38. D. Battistel, G. Battaglin, and S. Daniele, *Sensors and Actuators B-Chemical* **191**, 143 (2014).
39. D. P. Ruiz, J. L. Fierro, and P. A. Reyes, *Journal of the Brazilian Chemical Society* **21**, 262 (2010).
40. L. Maya, L. Riester, T. Thundat, and C. S. Yust, *J. Appl. Phys.* **84**, 6382 (1998).
41. J. F. Weaver, J. J. Chen, and A. L. Gerrard, *Surf. Sci.* **592**, 83 (2005).
42. H. Yang, *Angewandte Chemie-International Edition* **50**, 2674 (2011).
43. X. Zhao, M. Yin, L. Ma, L. Liang, C. Liu, J. Liao, T. Lu, and W. Xing, *Energy & Environmental Science* **4**, 2736 (2011).
44. T. Aaltonen, M. Ritala, T. Sajavaara, J. Keinonen, and M. Leskelä, *Chem. Mater.* **15**, 1924 (2003).
45. J. Hämäläinen, M. Ritala, and M. Leskelä, *Chem. Mater.* **26**, 786 (2014).
46. S. T. Christensen, J. W. Elam, B. Lee, Z. Feng, M. J. Bedzyk, and M. C. Hersam, *Chem. Mater.* **21**, 516 (2009).
47. D. J. Comstock, S. T. Christensen, J. W. Elam, M. J. Pellin, and M. C. Hersam, *Advanced Functional Materials* **20**, 3099 (2010).
48. C. Marichy, M. Bechelany, and N. Pinna, *Adv. Mater.* **24**, 1017 (2012).
49. K. Hauff, U. Tuttlies, G. Eigenberger, and U. Nieken, *Appl. Catal. B* **123**, 107 (2012).
50. K. Hauff, H. Dubbe, U. Tuttlies, G. Eigenberger, and U. Nieken, *Appl. Catal. B* **129**, 273 (2013).
51. N. Seriani, Z. Jin, W. Pompe, and L. C. Ciacchi, *Phys. Rev. B* **76**, 155421 (2007).
52. Z. L. Xue, M. J. Strouse, D. K. Shuh, C. B. Knobler, H. D. Kaesz, R. F. Hicks, and R. S. Williams, *J. Am. Chem. Soc.* **111**, 8779 (1989).
53. M. Hiratani, T. Nabatame, Y. Matsui, K. Imagawa, and S. Kimura, *J. Electrochem. Soc.* **148**, C524 (2001).
54. Y. J. Chen, H. D. Kaesz, H. Thridandam, and R. F. Hicks, *Appl. Phys. Lett.* **53**, 1591 (1988).
55. B. S. Kwak, P. N. First, A. Erbil, B. J. Wilkens, J. D. Budai, M. F. Chisholm, and L. A. Boatner, *J. Appl. Phys.* **72**, 3735 (1992).

56. B. Lecohier, J. M. Philippoz, and H. Vandenbergh, *Journal of Vacuum Science & Technology B* **10**, 262 (1992).
57. T. Aaltonen, P. Alen, M. Ritala, and M. Leskelä, *Chem. Vap. Deposition* **9**, 45 (2003).
58. O. K. Kwon, J. H. Kim, H. S. Park, and S. W. Kang, *J. Electrochem. Soc.* **151**, G109 (2004).
59. K. Kukli, J. Aarik, A. Aidla, T. Uustare, I. Jogi, J. Lu, M. Tallarida, M. Kemell, A. A. Kiisler, M. Ritala, and M. Leskela, *J. Cryst. Growth* **312**, 2025 (2010).
60. S. K. Kim, S. Y. Lee, S. W. Lee, G. W. Hwang, C. S. Hwang, J. W. Lee, and J. Jeong, *J. Electrochem. Soc.* **154**, D95-D101 (2007).
61. J. Hämäläinen, T. Hatanpaa, E. Puukilainen, T. Sajavaara, M. Ritala, and M. Leskelä, *J. Mater. Chem.* **21**, 16488 (2011).
62. J. Hämäläinen, F. Munnik, M. Ritala, and M. Leskelä, *J. Electrochem. Soc.* **156**, D418 (2009).
63. T. Aaltonen, M. Ritala, V. Sammelselg, and M. Leskelä, *J. Electrochem. Soc.* **151**, G489-G492 (2004).
64. S. W. Kim, S. H. Kwon, S. J. Jeong, J. S. Park, and S. W. Kang, *Electrochem. Solid-State Lett.* **11**, H303-H305 (2008).
65. B. H. Choi, J. H. Lee, H. K. Lee, and J. H. Kim, *Appl. Surf. Sci.* **257**, 9654 (2011).
66. T. Aaltonen, A. Rahtu, M. Ritala, and M. Leskelä, *Electrochem. Solid-State Lett.* **6**, C130 (2003).
67. A. J. M. Mackus, N.M. Leick, L.Baker, and W. M. M. Kessels, *Chem. Mater.* **24**, 1752 (2012).
68. I.J.M. Erkens, A. J. M. Mackus, H. C. M. Knoops, P. Smits, T.H.M. van de Ven, F. Roozeboom, and W. M. M. Kessels, *ECS Journal of Solid State Science and Technology* **1**, 255 (2012).
69. P. Shrestha, D. Gu, N. Tran, K. Tapily, H. Baumgart, and G. Namkoong, *Atomic Layer Deposition Applications 6* **33**, 127 (2010).
70. Y. Zhu, K. A. Dunn, and A. E. Kaloyeros, *J. Mater. Res.* **22**, 1292 (2007).
71. A. Mackus, S. Dielissen, J. Mulders, and W. M. M. Kessels, *Nanoscale* **4**, 4477 (2012).
72. W. M. M. Kessels, H. C. M. Knoops, S. A. F. Dielissen, A. J. M. Mackus, and M. C. M. van de Sanden, *Appl. Phys. Lett.* **95**, 013114 (2009).
73. S. T. Christensen and J. W. Elam, *Chem. Mater.* **22**, 2517 (2010).
74. X. Jiang and S. F. Bent, *J. Electrochem. Soc.* **154**, D648 (2007).

75. D. Longrie, K. vloo-Casier, D. Deduytsche, S. Van den Berghe, K. Driesen, and C. Detavernier, *ECS Journal of Solid State Science and Technology* **1**, Q123 (2012).
76. A. J. M. Mackus, D. Garcia-Alonso, H. C. M. Knoops, A. A. Bol, and W. M. M. Kessels, *Chem. Mater.* **25**, 1769 (2013).
77. L. Baker, A. Cavanagh, D. Seghete, S. George, A. Mackus, W. Kessels, Z. Liu, and F. Wagner, *J. Appl. Phys.* **109**, 084333 (2011).
78. Erkens I.J.M., H. C. M. Knoops, T. F. Landaluce, A. J. M. Mackus, M. Verheijen, F. Roozeboom, and W. M. M. Kessels, *Accepted for publication in Chemical Vapor Deposition* (2014).
79. J. Dendooven, R. K. Ramachandran, K. vloo-Casier, G. Rampelberg, M. Filez, H. Poelman, G. B. Marin, E. Fonda, and C. Detavernier, *J. Phys. Chem. C* **117**, 20557 (2013).
80. J. Hämäläinen, E. Puukilainen, T. Sajavaara, M. Ritala, and M. Leskelä, *Thin Solid Films* **531**, 243 (2013).
81. S. D. Elliott, *Langmuir* **26**, 9179 (2010).
82. T. Aaltonen, M. Ritala, Y. L. Tung, Y. Chi, K. Arstila, K. Meinander, and M. Leskelä, *J. Mater. Res.* **19**, 3353 (2004).
83. J. Elam, A. Zinovev, C. Han, H. Wang, U. Welp, J. Hryn, and M. Pellin, *Thin Solid Films* **515**, 1664 (2006).
84. J.W.Elam, A.V.V.Zinovev, Michael J.Pellin, David J.Comstock, and Mark C.Hersam, *ECS Trans.* **3** 271 (2007).
85. A. J. M. Mackus, M. A. Verheijen, N. M. Leick, A. A. Bol, and W. M. M. Kessels, *Chem. Mater.* **25**, 1905 (2013).
86. N. Leick, R. Verkuijlen, L. Lamagna, E. Langereis, S. Rushworth, F. Roozeboom, M. van de Sanden, and W. Kessels, *Journal of Vacuum Science & Technology A* **29**, 021016 (2011).
87. A. Mackus, N. Thissen, J. Mulders, P. Trompenaars, M. Verheijen, A. Bol, and W. Kessels, *J. Phys. Chem. C* **117**, 10788 (2013).
88. H. Profijt, S. Potts, M. van de Sanden, and W. M. M. Kessels, *Journal of Vacuum Science & Technology A* **29**, 050801 (2011).
89. C. Liu, C. C. Wang, C. C. Kei, Y. C. Hsueh, and T. P. Perng, *Small* **5**, 1535 (2009).
90. A. Johansson, R. Yang, K. Haugshoj, J. Larsen, V, L. Christensen, and E. Thomsen, V, *Int. J. Hydrogen Energy* **38**, 11406 (2013).

91. J. S. King, A. Wittstock, J. Biener, S. O. Kucheyev, Y. M. Wang, T. F. Baumann, S. K. Giri, A. V. Hamza, M. Baeumer, and S. F. Bent, *Nano Letters* **8**, 2405 (2008).
92. S. T. Christensen, J. W. Elam, F. A. Rabuffetti, Q. Ma, S. J. Weigand, B. Lee, S. Seifert, P. C. Stair, K. R. Poeppelmeier, M. C. Hersam, and M. J. Bedzyk, *Small* **5**, 750 (2009).
93. S. T. Christensen, H. Feng, J. L. Libera, N. Guo, J. T. Miller, P. C. Stair, and J. W. Elam, *Nano Letters* **10**, 3047 (2010).
94. H. B.-R. Lee and S. F. Bent, *Chem. Mater.* **24**, 279 (2012).
95. J. Lu, K. B. Low, Y. Lei, J. A. Libera, A. Nicholls, P. C. Stair, and J. W. Elam, *Nat. Commun.* **5**, 3264 (2014).
96. I. Utke, P. Hoffmann, and J. Melngailis, *Journal of Vacuum Science & Technology B* **26**, 1197 (2008).
97. W. van Dorp and C. Hagen, *J. Appl. Phys.* **104**, 081301 (2008).
98. O. Bethge, G. Pozzovivo, C. Henkel, S. Abermann, and E. Bertagnolli, *Journal of Micromechanics and Microengineering* **22**, 085013 (2012).
99. P. Dai, J. Xie, M. T. Mayer, X. Yang, J. Zhan, and D. Wang, *Angewandte Chemie-International Edition* **52**, 11119 (2013).
100. L. Baggetto, R. A. H. Niessen, F. Roozeboom, and P. H. L. Notten, *Adv. Funct. Mater.* **18**, 1057 (2008).
101. P. Banerjee, I. Perez, L. Henn-Lecordier, S. B. Lee, and G. W. Rubloff, *Nature Nanotechnology* **4**, 292 (2009).
102. C. T. Hsieh, Y. Y. Liu, D. Y. Tzou, and W. Y. Chen, *J. Phys. Chem. C* **116**, 26735 (2012).
103. Y. C. Hsueh, C. C. Wang, C. Liu, C. C. Kei, and T. P. Perng, *Nanotechnology* **23**, 405603 (2012).
104. R. V. Hull, L. Li, Y. C. Xing, and C. C. Chusuei, *Chem. Mater.* **18**, 1780 (2006).
105. H. C. M. Knoops, E. Langereis, M. C. M. van de Sanden, and W. M. M. Kessels, *J. Electrochem. Soc.* **157**, G241 (2010).

Chapter 3

Towards an Understanding of Precursor and Reactant Doses in ALD

Abstract

In atomic layer deposition (ALD), the dosing details for the precursor and co-reactant species play an important role in reaching saturation of the surface, in particular on surface topologies that contain 3D features. For some ALD processes the dosing details even determine the composition of the deposited material, e.g. the O/Pt ratio of Pt/PtO_x films when using the process with (MeCp)$PtMe_3$ and O_2 plasma. In this chapter, the influence of precursor and co-reactant doses is discussed in detail based on results from Monte Carlo simulations and mathematical models. For the ALD process using (MeCp)$PtMe_3$ precursor experimental results are also presented. These experiments yielded a sticking probability $s = 0.95$ for (MeCp)$PtMe_3$.

Introduction

Atomic layer deposition (ALD) is a cyclic thin-film deposition technique based on the alternating exposure of a substrate surface to precursor and co-reactant gasses (1). Some of the unique characteristics of ALD are its precise thickness control, uniformity over large substrate areas, and good conformality in 3D features. These features are based on the self-limiting nature of the half-reactions that occur at the surface during the consecutive precursor and reactant exposures, which are separated by purge and/or pump steps. When sufficient amounts of precursor and co-reactant species are supplied to the surface, saturation of these self-limiting half-reactions is achieved. Once saturation is reached, the deposition rate is no longer proportional to the particle dose *D*, *i.e.* the number of particles delivered to the surface during a certain amount of time. Therefore, the same amount of material is deposited everywhere on the surface, even when the surface topology contains 3D features. This is one of the key merits of ALD.

Reaching saturation, i.e. delivering the dose needed to fully saturate a substrate surface, is a fundamental and vital aspect in ALD. It is very important therefore, to know the process conditions that lead to saturation. This calls for a better understanding of the (surface) reactions that take place and the probabilities at which they occur. Reaching the saturation dose should preferably be done in an efficient manner, and a balance should be found in the careful trade-off between truly reaching saturation conditions and minimizing usage of the often expensive precursor while also minimizing total cycle time. An important parameter for reaching the appropriate balance is the residence time of the precursor particles in the deposition chamber (1).

For deposition in high aspect ratio (HAR) 3D features, precursor and reactant doses need to be considered even more closely. To achieve good conformality, saturation of the surface reactions for both the precursor and reactant step must be achieved throughout the 3D feature. Usually, ALD processes are optimized for planar geometries before deposition on 3D features is attempted. Whether adjustments to the precursor and/or reactant doses are needed for deposition in 3D features depends on the deposition regime that holds for the ALD process. Film growth can be considered to take place in one of three identified regimes: the reaction-limited (2), the diffusion-limited (2,3), or the recombination-limited regime

(4). The main factors are the aspect ratio (*AR*) of the 3D feature, the sticking probability *s* of the precursor/reactant, and the recombination probability *r* in the case of limited lifetime species. The sticking probability generalizes the reaction probability per collision for a particle to contribute to the ALD process. For relatively low *s* (reaction-limited regime) an increase in AR requires almost no increase in dose. For higher values of *s* (diffusion-limited regime) an increase in AR will require a strong increase in saturation dose. The recombination probability represents the probability that e.g. a plasma radical from the gas phase recombines with a surface species after which it is lost to the ALD surface reactions. In the recombination-limited regime, the dose depends strongly on *r*. Therefore, considering the influence of *s* and *r* on the particle dose more closely can be very valuable in determining saturation doses for ALD in HAR features.

In some cases, it may be necessary or desired to deliver a precursor and/or reactant dose that is greater or smaller than the saturation dose. For example, some processes have precursor and/or reactant half-reactions that are not strictly self-limiting, and increased exposure to precursor and/or reactant may change the properties of the deposited film. An example of such a process is ALD based on $(MeCp)PtMe_3$ and O_2 plasma, which can be used to deposit both Pt and PtO_x depending on the precursor and plasma doses (5). By increasing the O_2 plasma dose sufficiently beyond the saturation dose, the Pt that is deposited during the $(MeCp)PtMe_3$ step can be oxidized into PtO_x by the O-radicals (6). Remarkably, by increasing the $(MeCp)PtMe_3$ dose sufficiently beyond the saturation dose, the formed PtO_x can be reduced back into metallic Pt. Oxidation and reduction are temperature dependent, and for higher substrate temperatures, the $(MeCp)PtMe_3$ dose must be sufficiently low to obtain PtO_x. Other examples of ALD processes where precursor and reactant dose influence the composition of the deposited material are the Ru/RuO_x and the Ir/IrO_x processes (7,8).

Clearly, it is important to have good understanding of the *required* dose, i.e. the dose needed to obtain all the desired film properties, including conformality and composition. This *required* dose may be different from the (planar) *saturation* dose. In this work, we will look more closely into precursor and reactant doses, taking the ALD process based on $(MeCp)PtMe_3$ and O_2 plasma as a model system. We will first consider how the particle dose depends on the number of particles in the deposition chamber through the particle flux. Given that the particle density in the reactor depends on the net result from particle production terms and loss terms, the manner in which particles may enter or leave the deposition chamber during ALD will be discussed. Next, the relation between sticking probability and saturation dose will be examined for planar surfaces. The solution to the differential equation for the time-dependent surface coverage is presented and used to determine the sticking probability of the (MeCp)PtMe$_3$ precursor on a Pt surface.

Particle dose

In this section, the parameters that determine the precursor and reactant doses during ALD are discussed. The particle dose *D* can be defined as the number of particles impinging on a surface per unit area during a certain amount of time τ. Therefore, *D* is the time integral of the particle flux towards the surface as a function of time *J(t)*:

$$D\ (\tau)\ = \int_0^{\tau} J(t)dt. \qquad \text{(Equation 2.1)}$$

In this work, *D* will be expressed in collisions nm^{-2} unless indicated otherwise. For an ideal gas, the particle flux, i.e. the number of particles traveling in one direction through a surface per unit of area per unit of time, can be derived from kinetic theory:

$$J(t) = \frac{n(t)\,v}{4}, \qquad \text{(Equation 2.2)}$$

where *n(t)* is the density of the gas as a function of time and *v* is the mean speed of the particles. The mean speed of the particles can be derived from kinetic theory and is given by:

$$v\ = \sqrt{\frac{8kT}{\pi m}}, \qquad \text{(Equation 2.4)}$$

where *m* is the mass of the particles, *k* is the Boltzmann constant ($1.38{\cdot}10^{-23}$ JK^{-1}), and *T* is the gas temperature of the particles. By substituting Equation 2.3 and 2.4 in Equation 2.1, *J(t)* can be expressed as:

$$J(t) = n(t)\sqrt{\frac{kT}{2\pi m}}. \qquad \text{(Equation 2.5)}$$

Therefore, the dose for a particle with mass *m* at a temperature *T* depends directly on the particle density which may vary in time and which is the result from particle "production" and particle "loss." During an ALD half-cycle, particle production can occur through particle injection or local generation and particle loss can occur through pumping/purging or through surface losses. These pathways leading to particle production and loss will now be discussed in more detail.

Particle generation

The number of particles inside a deposition chamber will increase due to particle injection, or in the case of a plasma, due to local particle generation. Precursor particles are injected during the precursor step. The method of injection is typically chosen on the basis of the ALD reactor type, of which many exist. The method by which particles are introduced into the chamber depends on the vapor pressure of the precursor (1). If this vapor pressure is sufficiently high, particles will easily flow into the chamber by opening up the precursor container to the chamber. This is referred to as *vapor-drawn injection*. During vapor-drawn injection the chamber can be closed from the pump to increase the residence time of the particles. After the precursor pulse, the chamber can remain closed during an additional waiting period, allowing remaining precursor particles to react with the surface without adding new precursor particles. Alternatively, if the vapor pressure of the precursor is relatively low, the precursor is often dosed with an inert carrier gas. For *carrier gas injection*, the carrier gas flows from the precursor container through the deposition chamber to the pump, entraining the precursor molecules which may lead to a shorter residence time in the chamber. After the precursor step, the remaining precursor particles are removed by opening the chamber completely to the pump, thereby evacuating the chamber. An inert purge gas can be used to more effectively pump the reactor during the pumpdown.

During the reactant exposure, the reactant gas generally flows continuously through the reactor to the pump. For plasma-assisted ALD, the reactant step also includes a plasma step. In order to produce a stable plasma, the reactant gas generally flows before, during, and after plasma ignition. The plasma exposure time is the time during which plasma power is on, and during which plasma particles are generated. These plasma particles generally consist of radicals, photons, and ions, which all may provide reactivity to the surface (9). However, in this work only radicals are considered because they are considered most important for the Pt ALD process.

Particle loss

Particle loss can occur due to either purging/pumping or due to surface reactions. Particle loss due to purging/pumping depends on the pump speed and is reactor specific. We will first consider particle loss due to the surface reactions. For convenience we will assume that the surface is uniformly divided into identical surface sites, such that each surface site can accommodate one precursor particle. A surface site is referred to as active when it is capable of reacting with incoming particles. When a reactive surface site is not capable of reacting with particles it is referred to as "passive."

When a particle hits a surface site it can either react with the surface or be reflected. All the reactions that contribute to the ALD process in some manner are generalized by a reaction probability per collision, the sticking probability s. For precursor particles, ALD surface reactions may include ligand exchange, dissociation, association, etc. When one of these reactions occurs, the precursor particle "sticks" to the surface and is lost. Reactant particles (or fragments thereof) may stick to the surface and be incorporated in the deposited film. For example, during ALD of Al_2O_3, H_2O provides the O to the film (10). Reactant particles may also stick to the surface to take part in reactions during the following precursor step, e.g. chemisorbed O in Pt ALD (11). Reactant particles can also react with the surface to provide or remove surface groups, thereby facilitating ligand exchange, combustion, etc. Unlike precursor particles, multiple reactant particles may react with a single surface site, before saturation of the surface reactions is reached. For example, to combust the ligands of a single $(MeCp)PtMe_3$ molecule into CO_2 and H_2O, approximately 20 O particles are required (11).

Plasma radicals are generally subject to the same surface reaction losses as regular reactants, although they are usually more reactive. Therefore, many surface reactions occur faster, more readily, or even exclusively for these plasma particles. In the Pt ALD process for example, O-radicals do not need to dissociate on the Pt surface before becoming reactive, unlike O_2 molecules. As a result, they can often combust precursor ligands at much lower temperatures without being hindered by the presence of a carbonaceous layer that forms at these lower temperatures. A loss mechanism for plasma particles that does not contribute to the ALD process is surface recombination. For example, an O-radical may recombine with an O atom at the surface, forming gaseous O_2. This O_2 molecule is then lost for those ALD surface reactions for which O-radicals are required. The recombination probability r depends on the type of radical and the surface material (4).

Surface saturation

In the previous section the particle dose, and particle production and loss for ALD processes were discussed. In this section the saturation behavior of the surface will be examined more closely. We will first discuss some general observations concerning surface saturation, and then present some elementary simulations and calculations to obtain useful insights. For conceptual simplicity, we will only consider reactions where a single surface site can react with at most one particle, as is the case for e.g. precursor particles.

We assume that there are only two circumstances in which a particle hits the surface and is reflected and therefore not lost: *(i)* a particle hits a reactive surface site but does not react, *(ii)* a particle hits a passive (occupied) site. Consider now a surface consisting of only one single surface site. To determine the required dose for the saturation of this single surface site, only circumstance *(i)* needs to be considered. After all, for circumstance *(ii)* to occur, the site would already have to be saturated (i.e. occupied). Therefore, the average required saturation dose when considering a single surface site is equal to $1/s$ (i.e. s^{-1}) particles per site.

If we now consider the saturation of a surface consisting of multiple surface sites however, there is an increasing chance that an incoming particle will hit a passive site and is reflected (circumstance *(ii)*). On average therefore, the number of particles that will hit a single surface site before saturation of all the other surface sites is reached is greater than 1/*s*. This can be understood by considering that particles that hit passive sites contribute to the particle dose even though they cannot contribute to surface reactions (s = 0). The number of particles that will hit a single surface site before saturation of the entire surface is reached is defined here as the saturation dose per surface site D_s, and can be determined by a simple Monte Carlo simulation as will be demonstrated below.

Surface coverage: infinite particle reservoir

We will now determine the number of particles that must hit a surface site before saturation of the entire surface is reached, based on a Monte Carlo simulation. Consider a certain number S_0 of reactive surface sites, which are all active at the start of the simulation. We will define D_s as the dose per surface site required to reach 99 % rather than 100 % saturation of the surface, in order to save computation time. The interaction between particles and the surface will be considered on a particle-by-particle basis. This can be regarded as a loop, where during each iteration the interaction of a single particle with a single surface site is determined. During each iteration, one site is randomly selected to be hit by a particle. If the site is active, a random number between 0 and 1 is generated. If this random number is smaller than *s* the particle reacts, and the site is set to passive. If the random number is greater than *s*, or if the particle hits a passive site, the particle is reflected and the next iteration is started. The loop is repeated until 99 % of the surface sites are occupied. The particle reservoir is assumed to be infinite, i.e. the particle density is assumed to be independent of surface losses.

The results of this simple experiment (for 10^4 sites) are shown in Figure 3.1, where the saturation dose per surface site D_s is given as a function of *s* by the solid line. For comparison, the dotted line indicating $D_s = s^{-1}$ is also given. This line therefore indicates the saturation dose if only a single surface site is considered (only circumstance *(i)* can occur), while the solid line indicates the required dose if multiple surface sites are considered (circumstances *(i)* and *(ii)* can occur). As can be seen, the saturation dose per surface site when considering multiple surface sites $D_s = 4.6\ s^{-1}$. This indicates that, e.g. for s = 1 on average ~4.6 particles will hit any given site before 99 % saturation is reached.

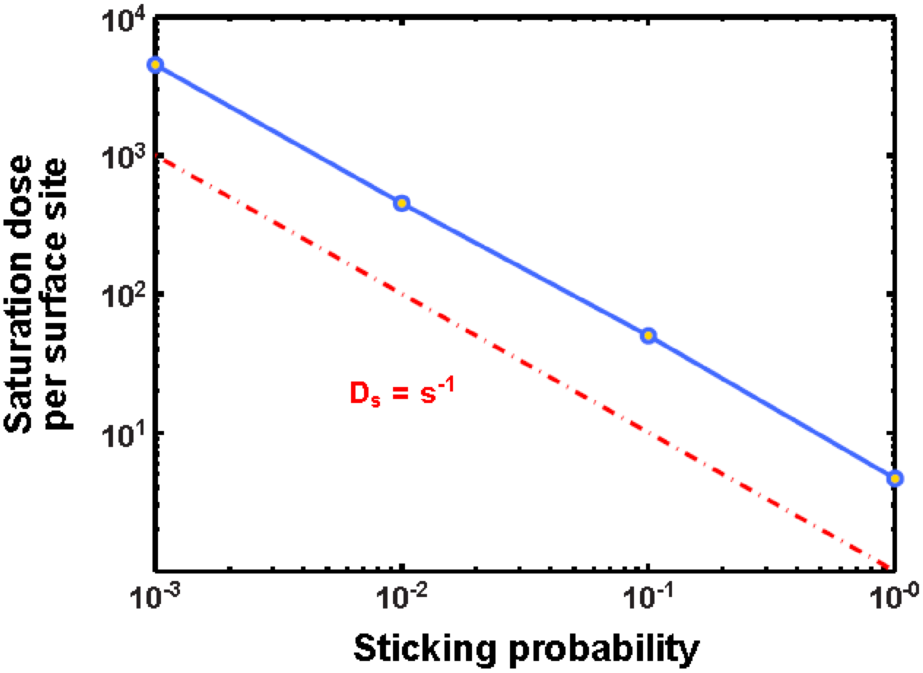

Figure 3.1. *The required dose for saturation per surface site as a function of sticking probability. The solid line indicates the values calculated by the Monte Carlo simulation. The dotted line serves as a reference where the saturation dose equals 1/s.*

Surface coverage: time-dependent solution

The previous simulation of the saturation dose as a function of sticking probability was based on a particle-by-particle approach. The time required to reach the saturation dose was therefore not taken into account. The rate with which the saturation dose is reached depends on the flux (Equation 2.5) of precursor particles towards the surface. We will now derive a mathematical expression which describes the surface coverage as a function of the sticking probability and time, i.e. taking the flux into account. We assume here that a certain number of precursor particles is present in a closed deposition chamber at t = 0, i.e. the influence of particle injection is not taken into account. Furthermore, to study the initial saturation behavior it is assumed that the number of particles is smaller than the number of surface sites and that one particle can react per site. Particles can only be lost by sticking to a surface site. Therefore, eventually all the particles will stick to the surface, resulting in a normalized surface coverage less than 1. The surface coverage can now be derived as follows.

Consider a volume V containing N_0 free particles at t = 0. This volume contains a reactive surface containing S_0 active adhesion sites ($N_0 < S_0$), each with area A_s, where particles will stick with a sticking probability s. As time progresses, a fraction of the particles hitting the reactive surface will stick, thereby reducing the number of free particles and active sites. The number of remaining free particles $N(t)$ and the number of remaining active sites $S(t)$ are related through:

$$N(t) = N_0 - \left(S_0 - S(t)\right). \qquad \text{(Equation 2.6)}$$

The change dS in $S(t)$ in a sufficiently small time interval dt (i.e. the number of free sites being occupied by particles in a small time interval) is given by:

$$\frac{dS(t)}{dt} = -sJ(t)S(t)A_s = -s\frac{N(t)}{V}\sqrt{\frac{kT}{2\pi m}}S(t)A_s, \qquad \text{(Equation 2.7)}$$

where Equation 2.5 was used to substitute $J(t)$ and $n(t)$ is given by $N(t)/V$. By substituting Equation 2.6 in Equation 2.7 and solving this differential Equation, $S(t)$ can be determined as follows. For convenience, the normalized surface coverage of active sites $\theta_a(t)$ is defined as:

$$\theta_\mathrm{a}(t) = \frac{S(t)}{S_0}, \qquad \text{(Equation 2.8)}$$

which gives the boundary conditions:

$$\theta_\mathrm{a}(0) = 1, \qquad \text{(Equation 2.9)}$$

since at t = 0, $S(t) = S_0$, and

$$\theta_\mathrm{a}(\infty) = \frac{S(\infty)}{S_0} = \frac{S_0 - N_0}{S_0}, \qquad \text{(Equation 2.10)}$$

because once all particles have reacted, $S(t) = S_0 - N_0$, since $N_0 < S_0$. By using the boundary conditions in Equations 2.9 and 2.10, the following solution for $\theta(t)$ is obtained:

$$\theta_\mathrm{a}(t) = \frac{S_0 - N_0}{S_0 - N_0 e^{-s\mathrm{C}(\mathrm{S_0}-\mathrm{N_0})\mathrm{t}}}. \qquad \text{(Equation 2.11)}$$

where, for convenience, C is defined as:

$$C = \frac{A_S}{V}\sqrt{\frac{kT}{2\pi m}}. \qquad \text{(Equation 2.12)}$$

The normalized surface coverage can now be defined as:

$$\theta(t) = 1 - \theta_a(t). \qquad \text{(Equation 2.13)}$$

This general mathematical derivation of the normalized surface coverage can be used to, for example, describe the surface coverage during the precursor step of an ALD process.

Experimental determination of the sticking probability of the (MeCp)PtMe$_3$ precursor

In this section, the sticking probability of the (MeCp)PtMe$_3$ precursor is determined experimentally. The basis for this determination is the expression which describes the normalized surface coverage as a function of sticking probability and time (Equation 2.13). This normalized surface coverage is equal to the growth per cycle (GPC) normalized with respect to the maximum GPC. After all, the maximum surface coverage (saturated precursor and reactant step) yields the maximum GPC for an ALD process. Therefore, the normalized GPC (NGPC) is a direct measure for the precursor surface coverage, assuming a fully saturated reactant step. The sticking probability can be determined experimentally by comparing GPC values as a function of exposure time to Equation 2.13. Such experiments were performed to determine the sticking probability of the (MeCp)PtMe$_3$ precursor.

To use Equation 2.13, the number of reactive adhesion sites S_0 should be known. Therefore, a well-defined reactive surface area with a homogeneous temperature was created. To do so, the entire inside of the home-built reactor (V = $11.4 \cdot 10^{-3}$ m^3) including the walls (T= 373 K) and the substrate stage (T=573 K) was coated with approximately 40 nm of Al_2O_3. After the reactor was coated, a substrate with an area of 6 cm^2 and with a 15 nm Pt seed layer on top was placed on the substrate stage. The thermal Pt ALD process using (MeCp)PtMe$_3$ and O_2 gas at a pressure of 0.01 mbar, which was used for these experiments, will undergo a nucleation delay of several hundreds of cycles on an Al_2O_3 surface (12). On Pt however, there is no nucleation delay. Therefore, by coating the reactor with Al_2O_3, growth is virtually inhibited anywhere except on the Pt seed layer substrate, at least for the initial few hundred cycles. For the obtained reactive area of 6 cm^2, the number of reactive adhesion sites S_0 corresponds to $1.8 \cdot 10^{15}$, based on the density of Pt and a GPC of 0.045 nm per cycle.

Furthermore, Equation 2.13 is valid under the assumption that at the onset of the precursor step, a fixed number of precursor molecules N_0 is present in a closed volume, and that $N_0 < S_0$. In order to meet this requirement, the precursor was heated to 45 °C and vapor-drawn into the reactor during a pulse of respectively 0.2, 0.4, and 1 s, while the valve to the turbo-pump was closed. This resulted in an NGPC of 0.18, 0.29, and 0.49 respectively, normalized to the saturation GPC for Pt ALD (0.045 nm per cycle). After the precursor pulse, the valve to the turbo-pump was kept closed for an additional variable waiting period between 0 and 7.5 s. This ensured that a fixed amount of precursor molecules was able to interact with the Pt substrate during a total precursor exposure time consisting of the pulse and the wait. The opening of the valve however took approximately 1.4 s, which means that the precursor particles were not evacuated from the deposition chamber immediately after the precursor pulse, even if the waiting period would have been 0 s. Therefore, precursor particles were assumed to be present in the deposition chamber for an additional 0.7 s after the end of the precursor pulse. The O_2 step consisted of a 10 s O_2 pulse (no plasma) at a pressure of 0.01 mbar. Using spectroscopic ellipsometry (SE), the GPC for a certain precursor pulse was determined as a function of the total precursor exposure time. By fitting Equation 2.13 (normalized surface coverage as a function of time) to the experimental data (NGPC as a function of exposure time), *s* was determined.

The results are shown in Figure 3.2, which shows the NGPC as a function of precursor exposure time for three different precursor pulse times: (a) 0.2 s, (b) 0.4 s, and (c) 1.0 s. The dots represent the experimentally determined GPC values, with the average value indicated by the dotted lines. The solid lines indicate the fits to Equation 2.13, which yielded an average sticking probability of ~0.95.

We will now consider the results from Figure 3.2 more closely. The dashed lines indicate the solution to Equation 2.13 for different sticking probabilities. This gives an indication of the dependence of the NGPC (and therefore also of the normalized surface coverage) on *s*. As can be seen, the normalized surface coverage as a function of time does not depend greatly on *s* for *s* > ~0.5. More importantly, all the data points in Figure 3.2 show that the NGPC is already in saturation after ~1 s. Although this makes it difficult to get a precise estimation of the sticking probability, it does clearly indicate that the sticking probability is relatively close to 1.

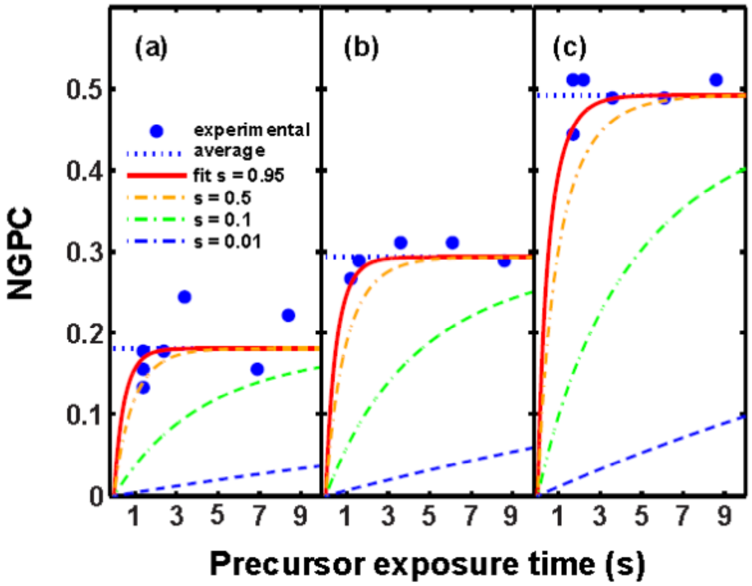

Figure 3.2. *Normalized growth per cycle (NGPC) as a function of precursor exposure time for different precursor pulse times* (a) 0.2 s, (b) 0.4 s, and (c) 1.0 s. *Dots indicate NGPC values as determined from SE, whose average is represented by the dotted lines. The solid lines indicate the fit to* $\theta(t)$ *(Equation 2.13), yielding a sticking probability of 0.95. The dashed lines represent Equation 2.13 for different sticking probabilities ranging from s =* 0.01 to 0.5*.*

Conclusion

In ALD, the precursor and co-reactant particle dose is the time integral of the particle flux towards the surface. This particle flux depends on the particle density of the precursor/reactant particles inside the deposition chamber, which varies in time due to particle production and loss. The number of particles will increase due to injection or generation. Particles will be lost due to purging/pumping or due to reactions with the surface or with surface species. Through a simple Monte Carlo simulation model, the required saturation dose per surface site as a function of the sticking probability was shown to be equal to 4.6 s^{-1}.

Using the particle flux as a function of particle density, the differential Equation describing surface coverage as a function of time could be solved. For $s > \sim 0.5$, the rate at which the surface is covered does not depend greatly on s. Experimental GPC data as a function of precursor exposure time was fitted using the mathematical expression describing surface coverage as a function of time. This yielded a sticking probability for the (MeCp)PtMe$_3$ precursor $s \approx 0.95$.

Bibliography

1. S. M. George, *Chemical Reviews* **110**, 111 (2010).
2. J. W. Elam, D. Routkevitch, P. P. Mardilovich, and S. M. George, *Chem. Mater.* **15**, 3507 (2003).
3. R. G. Gordon, D. Hausmann, E. Kim, and J. Shepard, *Chem. Vap. Deposition* **9**, 73 (2003).
4. H. C. M. Knoops, E. Langereis, M. C. M. van de Sanden, and W. M. M. Kessels, *J. Electrochem. Soc.* **157**, G241 (2010).
5. H. C. M. Knoops, A. J. M. Mackus, M. E. Donders, M. C. M. van de Sanden, P. H. L. Notten, and W. M. M. Kessels, *Electrochem. Solid-State Lett.* **12**, G34 (2009).
6. I.J.M. Erkens, A. J. M. Mackus, H. C. M. Knoops, M. Verheijen, F. Roozeboom, W. M. M. Kessels, and T. F. Landaluce, *Accepted for publication in Chemical Vapor Deposition* (2014).
7. S. W. Kim, S. H. Kwon, D. K. Kwak, and S. W. Kang, *J. Appl. Phys.* **103**, 023517 (2008).
8. J. Hämäläinen, M. Ritala, and M. Leskelä, *Chem. Mater.* **26**, 786 (2013).
9. H. Profijt, *Plasma-Surface Interaction in Plasma-Assisted Atomic Layer Deposition, PhD thesis* (2012).
10. R. L. Puurunen, *J. Appl. Phys.* **97**, 121301 (2005).
11. I. J. M. Erkens, A. J. M. Mackus, H. C. M. Knoops, P. Smits, T. H. M. van de Ven, F. Roozeboom, and W. M. M. Kessels, *ECS Journal of Solid State Science and Technology* **1**, 255 (2012).
12. L. Baker, A. Cavanagh, D. Seghete, S. George, A. Mackus, W. Kessels, Z. Liu, and F. Wagner, *J. Appl. Phys.* **109**, 084333 (2011).

Chapter 4

Mass Spectrometry Study of the Temperature Dependence of Pt Film Growth by Atomic Layer Deposition*

Abstract

Insights into the temperature dependence of atomic layer deposition (ALD) of Pt using (methylcyclopentadienyl)trimethylplatinum, (MeCp)PtMe$_3$, precursor and O_2 are presented, based on a study of reaction products by time-resolved quadrupole mass spectrometry (QMS) measurements. Above 250°C, Pt ALD proceeds through unhindered O_2 dissociation at the Pt surface, inducing complete and instantaneous combustion of the precursor ligands. Quantification of the QMS data revealed that at 300°C, approximately 20% of the C-atoms react during the precursor pulse, forming mainly CH_4 (~18 %) balanced by CO_2 (~2%). The remaining 80% of the C-atoms are combusted during the O_2 pulse. Time-resolved data indicated that the combustion reactions compete with the hydrogenation reactions for the available surface carbon. Combustion reactions were found to be dominant, provided that a sufficient amount of chemisorbed oxygen is available. When the temperature drops below 250°C, deposition becomes hindered by the presence of a carbonaceous surface layer of partially fragmented and dehydrogenated precursor ligands, formed during the precursor pulse. The carbonaceous layer limits dissociative chemisorption of O_2 and hence combustion reactions (leading to CO_2) whereas reduced surface reactivity also limits (de-)hydrogenation reactions (leading to CH_4). Below 100°C, the carbonaceous layer fully prevents O_2 dissociation and ALD of Pt cannot proceed.

*Published as: I.J.M. Erkens, A.J.M. Mackus, H.C.M. Knoops, P. Smits, T.H.M. van de Ven, F. Roozeboom and W.M.M. Kessels, *ECS Journal Solid State Science and Technology* **1**, 255 (2012)

Introduction

Atomic layer deposition (ALD) of Pt-group metals and their oxides on high aspect ratio 3-D nanostructures, can have a wide variety of applications in nanoelectronics as well as in sensing and catalysis (1-9). One noble metal ALD process that has attracted a lot of recent attention is that of platinum, based on (methylcyclopentadienyl)trimethylplatinum precursor ($(MeCp)PtMe_3$) and O_2 gas, as developed by Aaltonen *et al.*(10). As it is amongst the most widely applied and studied processes, it can be considered a model system for noble metal ALD processes that are based on the availability of chemisorbed surface oxygen at the start of each precursor pulse. Several studies have been performed on the reaction products that are produced during the process, to obtain information about surface reactions and to better understand the reaction mechanism (11-14). Extending the work of Aaltonen *et al.*(10), Kessels *et al.* (12) describe a possible reaction mechanism of the process at 300°C:

$$2\ (MeCp)PtMe_3(g) + 3\ O(ads) \rightarrow$$

$$2\ (MeCp)PtMe_2(ads) + CH_4(g) + CO_2(g) + H_2O(g) \qquad \text{(Equation 4.1)}$$

$$2\ (MeCp)PtMe_2(ads) + 24\ O_2(g) \rightarrow$$

$$2\ Pt(s) + 3\ O(ads) + 16\ CO_2(g) + 13\ H_2O(g). \qquad \text{(Equation 4.2)}$$

This mechanism was based on steady-state gas phase FTIR experiments in a cold-wall reactor at an O_2 pressure of 1 mbar. By balancing the carbon containing volatile reaction products, on average approximately 1 C-atom per precursor molecule was found to be removed during the precursor pulse. This occurs through combustion of the ligands by chemisorbed oxygen producing CO_2 and H_2O, as well as through the production of CH_4, with an observed CH_4 / CO_2 ratio of 1:1. During the subsequent O_2 step, the remaining hydrocarbon ligands, that constitute ~87% of the precursor carbon, are combusted by O_2 gas. Overall, this reaction mechanism was also confirmed by Christensen *et al.* (13) who analyzed the process at 300°C in a viscous flow reactor using QMS and quartz crystal microbalance (QCM) techniques. Their study confirmed that the majority of the C-atoms is combusted during the O_2 pulse, although the ratio of CH_4 / CO_2 production during the precursor pulse was found to be 5:1 instead of 1:1.

Despite these and other studies, several questions remain concerning the reaction mechanism of the Pt ALD process. One characteristic of the Pt ALD process that is still not fully understood is the temperature dependence of the growth per cycle (GPC). Knoops *et al.* showed that the growth of platinum is relatively constant between 300 and 250°C, while the GPC decreases between 250 and 150°C, and growth is inhibited for substrate temperatures of 150°C and lower (15). This behavior was also confirmed by new experiments (see Figure 4.1). An explanation for the reduced growth at lower temperatures was not given, although it was inferred from surface science studies that the dissociative chemisorption of O_2 should not be the limiting factor.

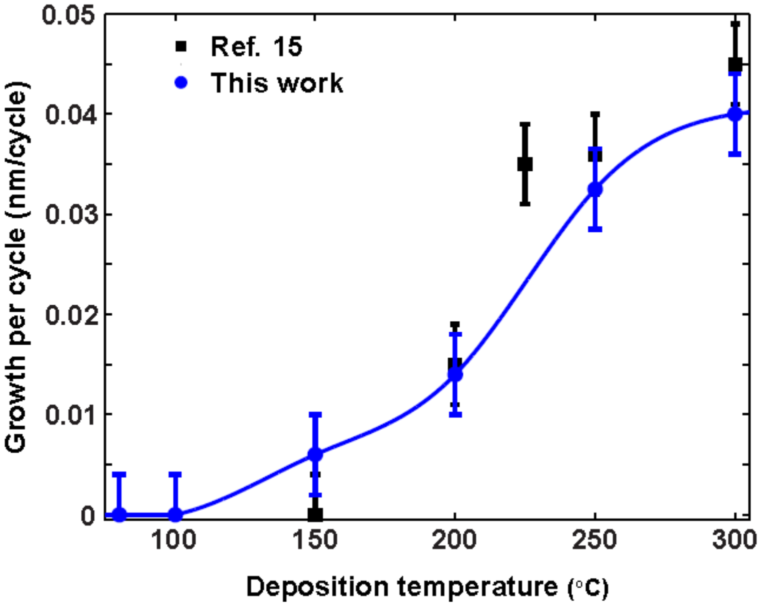

Figure 1. *The growth per cycle as a function of deposition temperature (curve serves as a guide to the eye). All depositions were carried out on as-deposited platinum seed layers with a thickness of 13 nm. Data from Knoops et al. (15) are given for comparison.*

Another matter that could benefit from further study is the fact that reaction Equations 4.1 and 4.2 are overall reactions, and give no information on individual reaction paths or on the reaction kinetics. Whereas CO_2 and H_2O can be ascribed to combustion by chemisorbed oxygen, some debate remains on the exact nature of the reaction leading to the production of CH_4 and the interdependency between the production of CH_4 and CO_2 / H_2O.

Elliott *et al.* suggest the involvement of in-situ created hydroxyl groups in the formation of CH_4, although to date the presence of OH groups has not been confirmed to the best of our knowledge (16). Mackus *et al.* make a strong case for the possibility of hydrogenation of the hydrocarbon surface ligands leading to the production of CH_4 (17).

To gain more insight into both the temperature dependence of the reaction mechanism, and to increase understanding of reaction kinetics , more data and especially time-resolved data is required. In the present work, the issue of both the temperature dependence of the GPC and the reaction kinetics is addressed on the basis of time-resolved QMS measurements carried out in an ALD temperature series. An explanation for the temperature dependence of the GPC and the inhibition of growth at lower temperatures by surface poisoning is given. Furthermore, the insights that were gained into the surface reactions and reaction rates during Pt ALD are described, showing that the reactions leading to the production of CH_4 compete with combustion reactions producing CO_2.

Experimental

Experimental setup

All measurements were performed in an open load home-built ALD reactor. It consists of a deposition chamber containing a substrate heating stage, connected to an inductively coupled plasma source (100 W) and a turbomolecular pump through gate valves. The temperature of the reactor walls T_w, which can be raised to 150°C, was kept at 80°C (unless mentioned otherwise) to prevent reactions from taking place at the walls , as will be explained later. The temperature of the substrate stage was varied between 80 and 300°C. The $(MeCp)PtMe_3$ precursor (98% purity, Sigma-Aldrich), kept at a temperature of 70°C, was vapor drawn into the reactor without any carrier gas and the precursor dosing time was typically 5 s. The O_2 flow was controlled using a mass flow controller to obtain a 10 s pulse with a stable pressure of 0.08 mbar. During the ALD cycles , the reaction chamber was continuously pumped by the turbomolecular pump. The pressure inside the deposition chamber varied from the base pressure of the order of 10^{-6} mbar during the 30 s pump-down step, to 0.08 mbar during the O_2 pulse.

A Pfeiffer Vacuum QMS 200 mass spectrometer with a mass-to-charge (*m/z*) range of 200 atomic mass units (amu) was connected to the deposition chamber through a pipeline (kept at 80°C) and a 150 µm pinhole. A channeltron detector was used, and the energy of the electrons in the ionizer was set to 70 eV. In-situ spectroscopic ellipsometry (SE) was performed using a J. A. Woollam, Inc. M2000U ellipsometer to determine the thickness of the deposited layers. For the modeling of the dielectric function of the deposited layers, a Drude-Lorentz parameterization was used, assuming that every film consists of a homogeneous layer of Pt (15). During standard SE monitoring, every measurement was performed after a complete cycle, immediately giving the GPC. During some experiments however the SE measurements were performed after every half-cycle, i.e. after every precursor step and after every O_2 step (18). This was done to obtain insight into the effects of precursor absorption and subsequent combustion on the apparent thickness of the film.

QMS measurement procedure

Performing QMS measurements during an ALD process poses several opportunities and challenges, and special care must be taken when recording and analyzing the data (19). The measurement procedure that was developed for this work will be described based on the measurements shown in Figure. This figure shows the measured QMS ion current as a function of time for substrate temperatures between 100 and 300°C (T_{wall} = 80°C). Precursor and O_2 pulse durations are indicated by arrows for clarity. As in previous studies (12,13) a scan of all relevant *m/z* ratios revealed that H_2O, CH_4 and CO_2 are the only gas phase reaction products that could be detected using QMS. In particular, measurements of *m/z* = 79 for the methylcyclopentadienyl ligand ($(C_5H_4)CH_3^+$) did not reveal this ligand as a reaction product, although it clearly appeared as a fragment in the precursor cracking pattern. Detection of H_2 as a reaction product proved challenging due to the abundance of *m/z* = 1 and 2 in the cracking pattern of the precursor and other species (e.g. CH_4 and H_2O). Therefore, although it was not detected, the production of H_2 could not be excluded based on the measurements performed here.

Furthermore, because the detection of H_2O can be troubled by condensation of water on the colder reactor walls and QMS line, the focus of the QMS analysis was on CH_4 and CO_2. To track CO_2, *m/z* = 44 was recorded, and for CH_4 the fragment at *m/z* = 15 (CH_3^+) was chosen rather than the signal due to the parent molecule at *m/z* = 16, to avoid interference from the signal caused by cracking of O_2. The sensitivity of the QMS for *m/z* = 15 and 44 is assumed to be constant. The QMS data shown in Figure 4.2 is based on measurements of ALD depositions on as-deposited Pt films under steady-state conditions, free from nucleation or start-up effects. The signals for *m/z* = 15 and 44 were recorded simultaneously to prevent any manual time alignment errors. A dwell-time of 0.05 s ensured that the systematic time alignment error caused by mass filter switching and settling did not exceed 0.1 s. The repetitive nature of ALD was optimally utilized to increase the signal-to-noise ratio (SNR) of the measurements: since every cycle can be assumed to be identical to the next, the QMS data of several cycles was aligned to overlap in time and then averaged, using a dedicated MATLAB algorithm. As a result, every line in Figure represents the average of at least 10 ALD cycles.

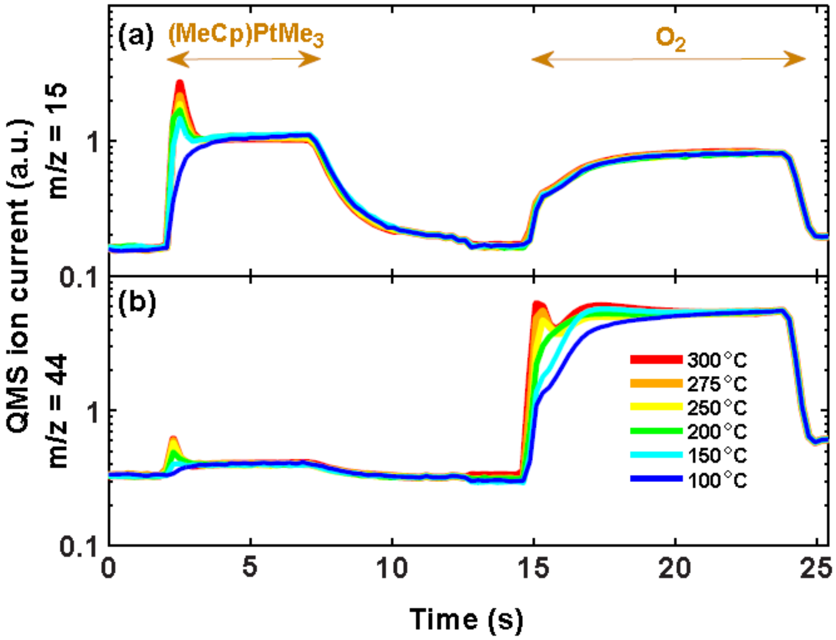

Figure 4.2. *Time resolved QMS signal for different substrates temperatures for (a) m/z = 15 (CH_3^+ from CH_4 and (MeCp)PtMe$_3$) and (b) m/z = 44 (CO_2^+ from CO_2). The precursor pulse (5 s) and O_2 pulse (10 s) are indicated by arrows for clarity. Comparison to precursor only and oxygen only data showed that at 100°C, virtually no reaction products are produced. The thinnest (blue) line can therefore be regarded as a baseline for the other data.*

The interpretation of the data is not straightforward because of two effects: *m/z* overlap and a pressure artifact. The former concerns the overlap between signals from reaction products and the precursor. As molecules are ionized through electron bombardment in the ionizer, several of them will break down into smaller fragments. These fragments, which in the case of the precursor form a broad spectrum of *m/z* ratios including 15 and 44, are also detected. The *m/z* ratios of 15 and 44 can therefore not be unambiguously assigned to CH_4 or CO_2, since the precursor and the reaction products are present in the deposition chamber at the same time. This can be seen during the precursor step in Figure. The measured ion currents at 100°C (dark blue lines) for both *m/z* ratios can be seen to increase during the precursor pulse (t = 2-7 s). This increase can be fully ascribed to fragments from the precursor. This was confirmed by measuring *precursor only* cycles (not shown): by repeatedly dosing only precursor into the deposition chamber (without subsequent O_2 pulse) the entire surface was saturated preventing any surface reaction products from being formed. The QMS signals measured during a precursor pulse under these saturated conditions therefore only had a precursor component. This precursor signal was then used as a reference for the full cycles, confirming that virtually no reaction products were formed at 100°C. Similarly, *oxygen only* cycles showed that the increase of both signals at 100°C during the O_2 pulse (t = 14-24 s) is also not caused by reaction products.

Under the applied conditions the QMS signal was found to depend on the *total* pressure in the deposition chamber rather than just the partial pressure of O_2. This is referred to here as the pressure artifact. During the O_2 pulse, the pressure inside the deposition chamber and as a result in the QMS detector increases over several orders of magnitude. For such high pressure variations, the QMS signals were found to show a dependence on the total pressure and not merely the partial pressure of a certain species. Peak pressures in the QMS detector of the order of $5 \cdot 10^{-6}$ mbar were detected, which might result in space charge effects in the ionizer and ion-neutral scattering interactions in the mass filter. This could cause deviations from linearity of the detected signal which is known to occur when the pressure inside the ionizer exceeds $\sim 10^{-5}$ mbar (20). However, both this pressure artifact and the *m/z* overlap could be corrected for.

The *precursor only* and *oxygen only* cycles confirmed that no significant amount of reaction products is formed during deposition at 100°C. While this is different for higher temperatures it shows that the reactor walls, kept at 80°C, will not contribute any significant amount of reaction products, i.e. virtually all reaction products are formed at the substrate stage. Furthermore, this offers the opportunity to use the measurements at 100°C as a reference for the measurements at higher temperatures since the precursor dose and O_2 pressure can be assumed constant over the studied temperature range. By subtracting this reference signal at 100°C from the other measured ion currents, both the precursor *m/z* overlap effect and the pressure artifact are ipso facto corrected. The result of this correction is plotted in Figure , which shows only the net reaction products as will be discussed in the next section.

Results

In Figure , the corrected QMS signals for the Pt ALD process can be seen, showing the net production of CH_4 ($m/z = 15$) and CO_2 ($m/z = 44$). Since the signals at 100°C were used as a reference, they are zero during the entire cycle by definition. Peaks in the signals can be seen however at the beginning of the precursor pulse for temperatures of 150°C and above. This indicates that ligand oxidation (leading to CO_2) and other surface reactions (leading to CH_4) can occur at these temperatures. The fact that production of CH_4 and CO_2 only occurs within the first second of the precursor pulse shows that the process reaches saturation after one second of precursor dosing, which was also observed by Kessels *et al.*(12). For higher temperatures, the amount of reaction products that is formed increases. In the insets of Figure , the production of CO_2 is shown to precede the production of CH_4; the signals for CO_2 production start rising and also reach peak value approximately 0.2 s before the signals for CH_4.

Figure 4.3 also shows that during the O_2 pulse, only CO_2 is produced and no CH_4, as was also reported in previous studies (11-13). Since the QMS signals in Figure have been baseline corrected and show the net production, the area under curve (AUC) is a direct measure for the amount of reaction products that is produced. This was used to quantify the carbon containing reaction products, by assuming that all 9 C-atoms of the precursor molecule are converted into volatile reaction products which are either CH_4 or CO_2. By balancing the AUC of the QMS signals for *m/z* = 15 and 44 for both the precursor and O_2 step at 300°C, the relative amounts of CH_4 and CO_2 could be determined. Firstly however, the AUC values of both species were corrected for partial ionization cross-sections. The total ionization cross-section for CO_2 at 70 eV is $3.56{\cdot}10^{-16}$ cm^2, while CO_2^+ has a partial ionization cross-section of $2.13{\cdot}10^{-16}$cm^2.(21) For CH_4 the total cross-section at 70 eV is $3.54{\cdot}10^{-16}$ cm^2, with a partial cross-section of $1.35{\cdot}10^{-16}$ cm^2 for the production of CH_3^+.(22) Based on measurements at 300°C it was determined that approximately 20% of the carbon is released during the (MeCp)PtMe$_3$ pulse: ~18% as CH_4, and ~2% as CO_2. The remaining 80% are combusted during the O_2 pulse and are converted into CO_2, which agrees nicely with previous results reported by Christensen *et al.*, and Kessels *et al.* (12,13).

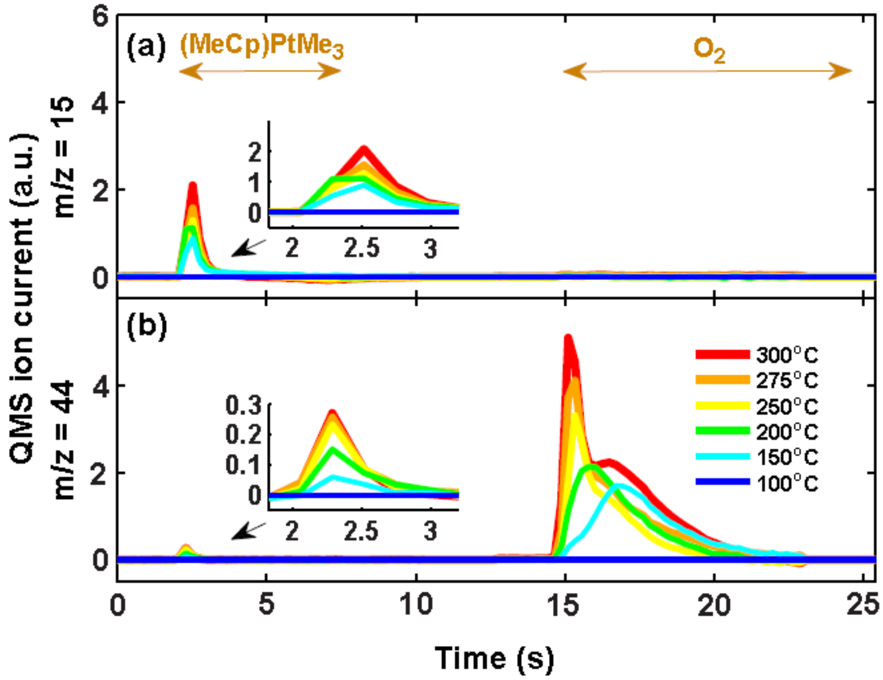

Figure 4.3. *(Color online) Baseline corrected QMS signal as deduced from Figure 4.2. Data are given for (a) m/z = 15 (CH_3^+ from CH_4 and (MeCp)PtMe$_3$) and (b) m/z = 44 (CO_2^+ from CO_2). The insets show the signal for CH_4 and CO_2 during the precursor pulse in more detail. The areas under the measured signals represent the amount of reaction products produced at a given temperature.*

Temperature dependence

The time-resolved QMS signals in Figure show that during the O_2 pulse the rate of combustion of the hydrocarbon precursor ligands on the Pt surface increases with temperature. At 150°C, CO_2 production reaches peak value approximately 2 seconds after the onset of the O_2 pulse, while at 300°C the peak in production is reached almost instantaneously. Based on the combustion rates during the O_2 pulse, 3 temperature regions can be distinguished:

(i) **T<100°C:** virtually no combustion occurs.

(ii) **100<T<250°C:** combustion occurs at a relatively slow rate, and complete combustion requires several seconds of O_2 dosing.

(iii) **T>250°C:** combustion occurs almost instantaneously; the bulk of the carbon atoms combusts within the first second of the O_2 pulse.

These temperature regions will be discussed in more detail later on in this section, although it should be noted here that the transitions between these regions are not considered to be sharply defined. Remarkably, at 300°C two distinct peaks can be distinguished: one large peak at the onset of O_2 dosing, and a shoulder that reaches its maximum approximately 2 seconds later. The combustion rate that is displayed by the shoulder is very similar to that of the reaction occurring at approximately 150°C. This suggests that at 300°C set-point temperature, combustion occurs at 2 different reactor zones, each with their own temperature. We therefore attribute the shoulder to reactions on parasitically heated reactor parts near the substrate stage (e.g. the parts holding the stage), that reach elevated temperatures due to heat transfer from the stage. At a heating stage temperature of 300°C these parts might reach temperatures were oxidation proceeds at a slower rate. This effect of parasitic heating also occurs at 250 and 275°C albeit to a much lesser extent. Although this is considered a likely explanation, other explanations (e.g. two distinct and separate reaction pathways leading to CO_2 production) cannot be ruled out at present.

The temperature dependence of the QMS data shows a strong correlation with that of the growth per cycle (GPC) data shown in Figure 4.1. This graph shows the GPC as a function of deposition temperature for the thermal ALD of Pt as measured with SE. As can be seen, no growth occurs for temperatures below ~100°C, while the GPC appears to saturate as a function of temperature starting at ~250°C, which agrees with the results from Knoops *et al.*(15). Parallel to the combustion rate, 3 temperature regions can therefore also be distinguished for the GPC:

(i) **T<100°C:** lack of growth, which coincides with lack of combustion.

(ii) **100<T<250°C:** limited growth, which is accompanied by combustion at a reduced rate.

(iii) **T>250°C:** normal growth as well as instantaneous combustion.

The strong correlation between ligand oxidation rate and GPC suggests that the rate of combustion of the ligands during the O_2 step is an important parameter in determining the temperature dependence of Pt ALD growth.

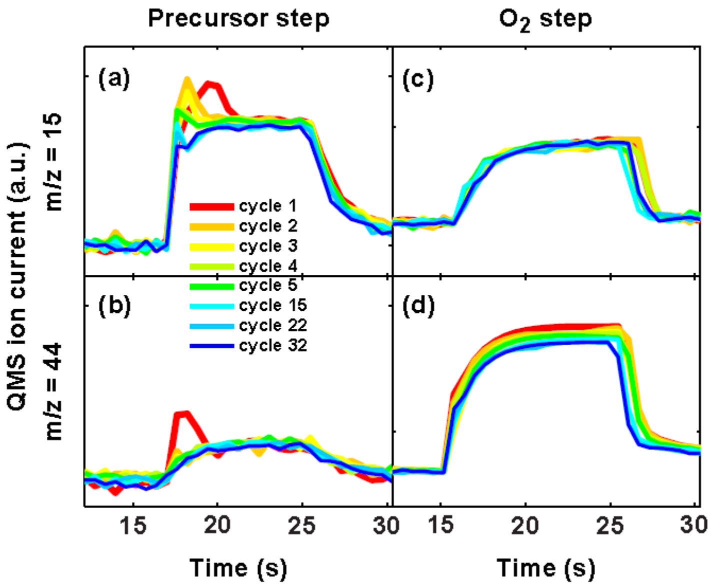

Figure 4.4. *The measured QMS signal for (a) m/z = 15 and (b) m/z = 44 during the precursor pulse, and (c) m/z = 15 and (d) m/z = 44 during the* O_2 *pulse; for 32 consecutive ALD cycles, all measured at 100°C. The ALD recipe for all cycles was similar to that of the measurement in Figure 4.2 (8 s* $(MeCp)PtMe_3$*, 10 s* O_2*). However, prior to the first cycle, the entire reactive Pt surface was treated with an* O_2 *plasma. Since virtually no reaction products are produced during cycle 32, this can be regarded as the baseline level.*

Reactions at 100°C

To learn more about possible surface reactions at lower temperatures, the process at 100°C was studied in more detail. Although no reactions take place under steady state ALD conditions at 100°C, it is known that plasma assisted ALD of Pt at this temperature is possible (15). The highly reactive atomic oxygen generated in the plasma ensures complete hydrocarbon removal at the end of every cycle. Therefore, an experiment was devised where standard thermal ALD cycles were preceded by an O_2 plasma treatment. By starting on a plasma-treated surface, surface reactions are expected to occur at least for the first precursor pulse at 100°C. By monitoring the following subsequent cycles individually, valuable information about the process was obtained.

Because a plasma was used, reactions could also take place at the reactor walls during this experiment. Therefore, the walls were also heated to 100°C (instead of 80°C), turning the entire deposition chamber into one large reactive surface with one single temperature. Furthermore, for these experiments the reactor walls were completely coated with Pt, to ensure a homogeneous reactive surface composition, and the precursor pulse was increased to 8 seconds to ensure saturation for this larger surface area. The QMS signals of the cycles are shown in Figure , and the corresponding AUC values as a function of cycle number (indicating a measure for the amount of reaction products produced) are shown in Figure . The graphs in Figure show the as-measured QMS ion currents, i.e. no corrections with respect to a reference have been applied. As a result both the precursor and the pressure artifact are visible. However, cycle 32 can be regarded as a reference because hardly any reaction products are formed anymore during that cycle. This can be inferred from the fact that after cycle 25 the AUC values remained relatively constant and no growth occurred. This can be seen more clearly in Figure , where AUC values flatten out beyond cycle 25. The baseline level (indicating a lack of reaction products) that is reached after cycle 25 is represented by the black dotted lines which serve as a guide to the eye.

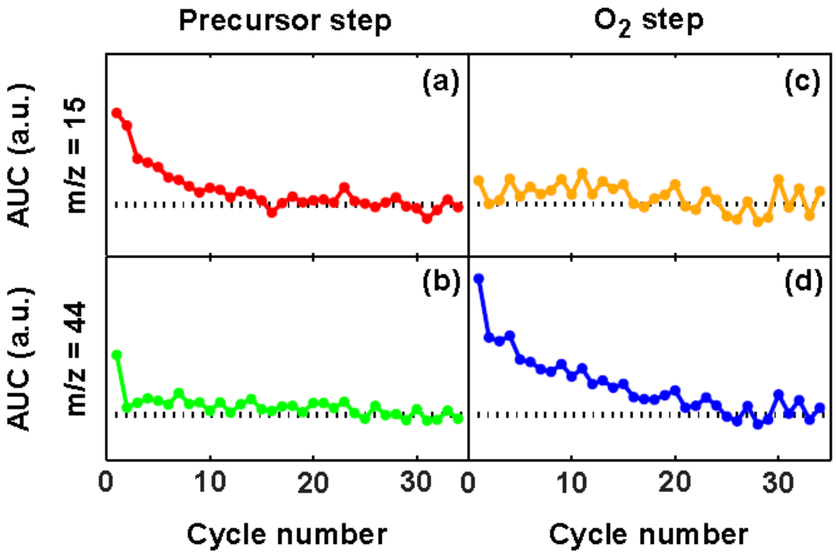

Figure 5.5. *(a-d) The area under curve (AUC) of the measurements shown in Figure 4.4, representing the amount of reaction products as a function of cycle number. Prior to the first cycle the Pt surface was treated with an* O_2 *plasma. Baseline values that are reached after cycle 25 are indicated by the black dotted lines which serve as a guide to the eye.*

The signals in Figure will now be considered cycle-by-cycle, starting at cycle 1, which was the first standard ALD cycle following the plasma treatment. Clearly, reaction products are indeed formed during this cycle. The production of CH_4 and CO_2 is evident from the peaks in the signals that are observed at the beginning of the precursor pulse in Figure (a) and (b). The peaks in Figure (a) and (b) are broader, i.e. the signals increase over a longer period of time compared to the signals during the peaks in Figure. This indicates that reactions proceed for a longer period of time. The longer reaction times are most likely due to the fact that the precursor requires more time to saturate the larger reactive surface. It is also possible however that the increased reaction time is caused by slower reaction kinetics due to the lower temperature. Because the reactions are stretched out over a longer period of time, it becomes even clearer that the production of CO_2 precedes the production of CH_4.

Furthermore, during the precursor step of the next cycle (cycle 2), the production of CO_2 has disappeared almost completely, while the production of CH_4 still persists. Because the reaction pathway leading to CH_4 is now unhindered by competing combustion reactions, this pathway becomes more dominant, and CH_4 is produced at the very onset of precursor dosing. This clearly demonstrates that the production of CH_4 is a separate process that does not necessarily depend upon the production of CO_2, at least at a temperature of 100°C. During the following cycles, the amount of CH_4 production gradually decreases until it reaches baseline values around cycle 25. Considering the O_2 pulse, see Figure (c) and (d), no production of CH_4 was detected during any cycle as expected. Some CO_2 is produced during the first cycles (compared to reference cycle 32) although there is no clear peak as was seen in Figure. This indicates that although there is some carbon combustion during the first cycles after the plasma treatment, combustion is far less effective than at 300°C.

During the following cycles the amount of CO_2 that is produced continuously decreases up to approximately cycle 25. After cycle 25, the CO_2 signal remains relatively constant indicating combustion has ceased. The decrease in the amount of reaction products can also be seen in the AUC values in Figure . The amount of CH_4 during the precursor step slowly decreases over several cycles, while the production of CO_2 drops to baseline immediately after cycle 1. This shows nicely that the production of CH_4 persists even after the production of CO_2 has ceased. During the O_2 step, the amount of combustion products continuously decreases, while no production of CH_4 can be seen. During this experiment, SE data was also recorded which showed an increase of apparent thickness of 0.1 nm over cycle 1 (GPC for plasma assisted ALD of Pt at 100°C is normally 0.045 nm), while during the following cycles virtually no growth was detected. The relatively large increase during the first cycle indicates that precursor molecules did adsorb during the precursor pulse, but that their ligands were not completely combusted during the O_2 pulse.

Summarizing these results, the study of the thermal process following plasma treatment at 100°C indicates that no growth occurs at this temperature due to the lack of ligand combustion. When chemisorbed oxygen is available however (due to e.g. a plasma treatment), precursor molecules can adsorb with their ligands reacting into CO_2 and CH_4. In the absence of chemisorbed oxygen, only CH_4 can be produced until reactions become prevented by some form of surface blocking.

Spectroscopic ellipsometry

Whereas growth below 100°C is completely inhibited for the thermal process, between 100 and 250°C growth does occur albeit at lower growth rates, as was depicted in Figure 4.1. The temperature regime in which this occurs coincides with the production of CO_2 at reduced reaction rates during the O_2 pulse (see Figure). To examine the growth behavior more closely, additional SE measurements were performed at temperatures between 80 and 300°C. The data is shown for 4 cycles in Figure . The thickness was measured after every half-cycle, i.e. after every precursor and after every O_2 step.

Once again, three distinct temperature regions become apparent. Above 250°C, a sawtooth-shaped curve is obtained. Between 100 and 250°C this sawtooth shape can no longer be seen, although there is still some growth. At temperatures of 100°C and below, the apparent thickness remains virtually constant, indicating very little or no growth. The characteristic sawtooth-shaped curve that was observed for temperatures above 250°C, can be explained by considering the apparent thickness of the surface (18). After the precursor pulse, the thickness of the layer will have increased with the newly deposited Pt as well as the adsorbed precursor ligands which have not yet been eliminated.

The SE model that was used in these experiments assumes that the dielectric properties of the layer are constant. The thickness of the layer was the only parameter that was varied to fit the data. Therefore, the uncombusted ligands could cause a relatively large increase in the apparent thickness of the layer, greater than the GPC. During the subsequent O_2 pulse the excess ligands are combusted, causing a (smaller) decrease in apparent thickness. The difference between the increase in apparent thickness during the precursor step, and the decrease in apparent thickness during the O_2 step, yields the GPC.

By combining the insights gained from the experiments described above, a more comprehensive model of the temperature dependence of the reaction mechanism can be obtained as well as a better understanding of individual reaction paths, as will be discussed in the next section.

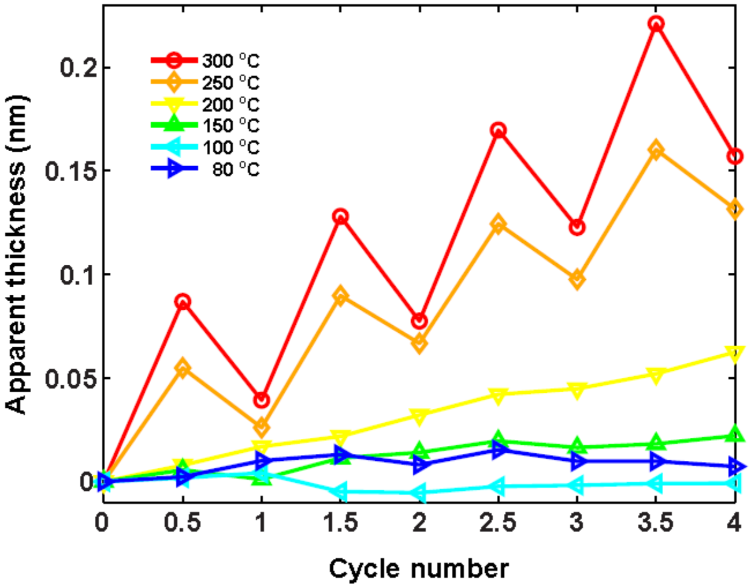

Figure 4.6. *The apparent thickness of the films obtained from SE, performed every half-cycle for ALD at different substrate temperatures different temperatures. The half-integer and full-integer data points represent SE measurements after the precursor and* O_2 *pulse, respectively.*

Discussion

The implications of the results shown in the previous section for our understanding of the reaction mechanism of Pt ALD will be discussed here.

Temperature dependence

(i) **T<100°C** Starting at lower temperatures, it is clear from Figure 4.1 that no growth occurs at ~100°C. Figure 4.3 shows furthermore, that no reaction products are formed at this temperature. A possible explanation for the lack of growth and reaction products could be poor precursor adsorption at lower temperatures. However, adsorption of the precursor has been reported even at room temperature (23). Furthermore, it is known that plasma assisted ALD of Pt is possible at 100°C, and in the plasma treatment experiment shown in Figure 4.4 reaction products were observed during the 1st cycle. This confirms that the precursor can adsorb at 100°C. Another possible explanation for growth inhibition would be the lack of chemisorbed surface oxygen at the onset of the precursor pulse. However, according to Getman *et al.* the oxygen surface coverage of a Pt(111) surface in equilibrium with O_2 gas, should not depend on temperature in the ALD range (24). This coverage was found to be 0.25 monolayers (ML) on Pt(111) for the temperatures and pressures used in the Pt ALD process (25). The presence of surface oxygen at 100°C is also indicated by the fact that CO_2 was detected during the first cycle after the plasma treatment (see Figure 4.4 (b)). The amount of chemisorbed oxygen that can cover a clean Pt surface at a temperature of 100°C should therefore not be the limiting factor inhibiting growth either.

One remaining possible cause is the incomplete combustion of the precursor ligands during the O_2 pulse. The data in Figure 4.1 and Figure 4.3 show a clear correlation between a reduced GPC and the reduced level of combustion during the O_2 pulse at lower temperatures. Reduced combustion was also indicated by the relatively small amount of CO_2 that was detected during the O_2 pulse for the cycles following the plasma treatment (Figure 4.4 (d)). Furthermore, the experiments involving a plasma treatment also showed that beyond the first cycle, no CO_2 was produced during the precursor pulse, even though the production of CH_4 continued (Figure 4.4 (a, b)). This suggests that under these conditions no chemisorbed oxygen is available at the beginning of the precursor pulse. In order to explain the lack of chemisorbed oxygen, the state of the platinum surface after the precursor pulse should be considered.

The (MeCp)PtMe$_3$ precursor contains both methyl (Me) and methylcyclopentadienyl (MeCp) ligands. Due to the catalytic nature of Pt however, it is likely that some of the ligands on the surface will become fragmented upon precursor adsorption (17). For conceptual clarity however, the initial species on the surface after precursor adsorption are assumed here to be either Me or MeCp. The fact that the MeCp ligand was not detected as a volatile reaction product in this work or in the QMS study of Christensen *et al.* indicates that this ligand remains at the surface (13). In our previous work on the Pt ALD mechanism, a compelling case was made for the use of results from the surface science literature (17). The behavior of hydrocarbon species on Pt surfaces was discussed extensively, and the relevant results will be discussed here. The surface chemistry of Me groups on a Pt (111) surface can be described as a competition between hydrogenation producing CH_4, and dehydrogenation reactions forming hydrocarbon species that have a relatively high C/H ratio (26,27). The desorption of methane takes place for temperatures of -73°C and higher (27). Concerning the behavior of MeCp on a Pt surface, results reported for other cyclic hydrocarbon species can be useful since different cyclic hydrocarbon species are reported to behave similarly on Pt (28). Marsh *et al*. describe temperature programmed desorption (TPD) measurements of a benzene covered Pt(111) surface (29) In their experiment, the substrate temperature was gradually raised while the substrate was exposed to O_2. They found that below a temperature of 107°C the pre-adsorption of benzene on the Pt (111) inhibits the adsorption of oxygen as a result of which hydrocarbon oxidation is inhibited. Given the agreement between results from Marsh *et al.* and those reported here, it is plausible that a similar inhibition of ligand combustion occurs during the Pt ALD process at temperatures of ~100°C. At these temperatures, both the MeCp ligands and the carbon-rich products of MeCp / Me dehydrogenation could form a carbonaceous layer that blocks surface sites required for O_2 dissociation, thereby preventing combustion. This is corroborated by the fact that in Figure 4.4 (b) no CO_2 is produced during the precursor pulse beyond cycle 1. The relatively small and decreasing amount of combustion products during the O_2 pulse (Figure 4.4 (d)) also indicates a gradual "poisoning" of the Pt surface by carbonaceous surface species. Similarly, the surface species could inhibit further hydrogenation of Me ligands preventing CH_4 production. Evidence of this inhibition can be seen in Figure 4.4 (a), where the production of CH_4 gradually extinguishes in the subsequent cycles. The presence of the unreactive hydrocarbon species might thereby inhibit growth by hindering hydrogenation and by blocking oxygen chemisorption. This would also explain why plasma-assisted deposition is possible at low temperatures; the oxygen radicals that are generated in the plasma do not need to be dissociated at the Pt surface and can react directly with the hydrocarbon fragments on the surface.

(ii) **100<T<250°C** The Pt ALD process between 100 and 250°C is characterized by an increase in the GPC as well as an increase in the amount of CH_4 and CO_2 produced in the precursor pulse. Furthermore, the reaction rate for combustion during the O_2 pulse increases as a function of temperature, although combustion is not yet instantaneous (see Figure 4.3). Apparently, due to the increase in substrate temperature, a larger amount of precursor molecules can absorb due to increased ligand combustion during the O_2 pulse. An explanation for this increase in combustion can be found by once again considering the Me/MeCp-covered platinum surface. In their TPD experiments of a benzene covered Pt surface exposed to O_2, Marsh *et al*. reported the production of CO_2 and H_2O for temperatures between 107-347°C (29). They ascribed the oxidation of benzene to a reaction between benzene derived intermediates and atomic oxygen at the surface. The temperature range in which Marsh *et al.* observed the production of CO_2 and H_2O coincide remarkably with the onset of the formation of combustion products presented in this work. This indicates that the MeCp group starts to react with oxygen above ~100°C. Furthermore, it is likely that MeCp can start to undergo dehydrogenation in the temperature region between ~100 and ~250°C: Cp is reported to start to dehydrogenate on a Pt surface for temperatures above 223°C, while benzene dehydrogenates above 177°C (30-32). Clearly, in the temperature range between 100 and 250°C MeCp becomes more reactive with the surface. Some of the MeCp groups could form intermediates or start to break into smaller hydrocarbon groups by dehydrogenation. Furthermore, the products of dehydrogenation of the Me and MeCp species are likely to change as a function of temperature. The increased reactivity of the MeCp with the surface and the possible change in dehydrogenation reaction products can lead to a change in the composition and thickness of the carbonaceous layer that is formed during the precursor pulse. This would free up more sites for oxygen chemisorption which will lead to increased combustion. A final possible cause for the increased reaction product formation and growth is the increased combustion rate at higher temperatures which was observed in Figure 4.3.

While it is difficult to give a precise description of all the surface species and surface reactions, it does seem likely that an increase in surface temperature has the following two effects: a change in composition of the surface species allowing more oxygen chemisorption, and enhanced combustion reactions. A combination of these effects could lead to increased ligand combustion, subsequent increased precursor adsorption, and therefore, increased growth per cycle. This explanation is in line with the SE measurements shown in Figure . When SE measurements are performed every half-cycle during normal Pt ALD growth (i.e. at 300°C), the apparent thickness of the film can increase upon precursor adsorption, due to the bulky ligands that remain at the surface. After the subsequent O_2

pulse these ligands are combusted, which could cause a relative decrease in apparent thickness. Between 100 and 250°C however, the amount of precursor molecules that adsorb is too small to cause a noticeable change in apparent thickness, since the surface is already covered with a carbonaceous layer at the beginning of the precursor pulse. Similarly, the small amount of ligands that is combusted during the O_2 pulse causes only a negligible change in apparent thickness. The growth caused by the small amount of precursor molecules that adsorbs can only be detected when measured over several cycles.

(iii) **T>250°C.** The temperature region between 250 and 300°C is characterized by a growth per cycle that seems to flatten for higher temperatures (Figure 4.1), sawtooth shaped SE half-cycle curves (Figure 4.6), and instantaneous combustion during the O_2 pulse (Figure 4.2). At these temperatures the hydrocarbon species at the Pt surface are fragmented to such an extent that oxygen can chemisorb unhindered and react immediately with these species until virtually all surface carbon is removed.

Reactions at 300°C

The study of the temperature dependence of the reaction mechanism presented in this work also provides insight into Pt ALD at 300°C, which is the typically employed deposition temperature for this process. The involvement of dehydrogenation reactions has been suggested by Mackus *et al.* to explain the formation of CH_4 during the precursor pulse (17). They describe the surface reactions as a competition between these dehydrogenation reactions and combustion reactions, where the latter take precedence provided a sufficient supply of oxygen is available. When most of the oxygen has been consumed, the production of CO_2 will diminish and be replaced by CH_4 formation. This explains why CH_4 is produced during the precursor pulse only. The proposed competition between combustion and hydrogenation reactions for the available surface carbon is supported by the time-resolved QMS data in Figures 3 and 4. In both figures the production of CO_2 is shown to precede CH_4 formation, although the distinction is much clearer for the first cycle in Figure 4.4. The peak in CH_4 formation occurs approximately 2 seconds after the peak in CO_2 production. During the following cycles, the absence of CO_2 production causes CH_4 to be produced earlier after the start of the precursor pulse and at an increased rate. This clearly points to a competition between these two reactions and supports the occurrence of dehydrogenation reactions. The fact that the data in Figure 4.4 was obtained at 100°C should not be of major influence given that the reaction kinetics during the precursor pulse do not seem to depend greatly on temperature as can be seen in Figure 4.3. Further indications that dehydrogenation reactions play a role in the reaction mechanism of Pt ALD can be found by evaluating the reaction mechanism (Equation 4.1 and 4.2). In this reaction mechanism equation, which was based on an FTIR study, the ratio of CH_4 / CO_2 production during the precursor pulse was found to be 1:1 (12). One CH_3 ligand is combusted by 2 O atoms, releasing 3 H atoms. These 3 H atoms are sufficient to produce 1 H_2O molecule and hydrogenate 1 Me ligand from another precursor molecule to produce CH_4. The combustion of 1 Me ligand therefore provides the hydrogen for the production of 1 CH_4 molecule. In this work however, as well as in the study by Christensen, the CH_4 / CO_2 ratio was found to be 6 to 9 times higher. Assuming the ratio is larger than 1, this excess CH_4 production during the precursor pulse requires an additional source of H atoms. Since hydroxyl (OH) groups or H_2O are not expected to be stable on the Pt surface, the only available source for this H is the precursor ligands themselves (33). Since the combustion of ligands is insufficient to supply the hydrogen (CH_4 / CO_2 >1), the likely alternative would be the dehydrogenation of other Me or MeCp ligands. Therefore, the relatively high amount of CH_4 production during the precursor pulse implies that dehydrogenation reactions take place. Since the CH_4 / CO_2 ratio is relevant for this matter, the different values found in the mentioned studies will be discussed briefly. A possible explanation for the differences in the ratio of the reaction products could be found in the measurement techniques that were used, and differences in process parameters (see Table 4.1). During both QMS studies, the reaction products were measured in real-time, while during the FTIR study a single measurement lasted up to 5 minutes. Furthermore, while performing the FTIR measurements, all reaction products were confined to the deposition chamber, and it cannot be excluded that this leads to additional or different reactions. Despite the differences in CH_4 / CO_2 ratio, the overall reaction mechanism is expected to be similar, since all 3 studies show that the majority of the carbon is combusted during the O_2 pulse.

***Table 4.1.** Summary of the results of several studies with respect to the amount of reaction products that are produced during Pt ALD. Relevant process parameters are also listed.*

Referenc	Techniqu	Precursor		O$_2$ step		O$_2$ Pressur	Substrate Temperatur	Wall Temperatur
		CH$_4$	CO$_2$	CH	CO$_2$			
(12)	FTIR	6.5	6.5	0	87	1 mbar	300°C	80°C
(13)	QMS	18%	3%	0	79	1.3	300°C	300°C
This work	QMS	18%	2%	0	80	0.08	300°C	80°C

Conclusions

Time-resolved QMS and in-situ SE results in combination with insights from surface science studies were used to investigate the reaction mechanism of Pt ALD. An investigation of the temperature dependence showed that the process can roughly be divided into 3 temperature regions. At and below 100°C, growth is inhibited and virtually no reaction products are formed. Between 100°C and 250°C, the GPC, the amount of reaction products, and the rate of combustion increase as a function of temperature. Above 250°C, the GPC is relatively constant while combustion occurs instantaneously and is complete. Monitoring the process after a plasma treatment with QMS and in-situ SE showed that the lack of growth at low temperatures cannot be ascribed to poor precursor adsorption or reduced oxygen chemisorption, but is due to lack of ligand combustion. An explanation for the temperature dependence of the reaction mechanism was found by considering the possible behavior of MeCp and Me on the surface. Below 100°C, the MeCp ligand remains uncombusted and can form a carbonaceous layer together with the carbon-rich products of MeCp / Me dehydrogenation. This carbonaceous layer might block sites required for oxygen dissociation. Above 100°C, MeCp may start to dehydrogenate (allowing for CH_4 production) and the increased temperature may change the composition and thickness of the carbonaceous layer. This would allow oxygen to dissociate leading to CO_2 production. Furthermore, ligand combustion may proceed at faster rates for elevated temperatures. Above 250°C, the surface groups have been fragmented by dehydrogenation or other reactions to such an extent that oxygen can dissociate and chemisorb on the surface unhindered, and combustion occurs instantaneously.

Quantification of the QMS data at 300°C indicated that approximately 20% of all precursor carbon atoms react during the precursor pulse: ~18% as CH_4, and ~2% as CO_2. The remaining 80% of the precursor carbon is combusted during the O_2 pulse. The fact that more CH_4 than CO_2 is produced during the precursor pulse suggests that the dehydrogenation of the Me and MeCp ligands supplies the required H for hydrogenation of Me to form CH_4. The time-resolved QMS data indicated that combustion and hydrogenation reactions (producing CO_2 and CH_4, respectively) compete for the available surface carbon and that combustion is the dominant reaction provided a sufficient supply of oxygen is available.

The reaction mechanism of Pt ALD has been discussed on the basis of the behavior of both Me and MeCp on the Pt surface. As mentioned previously, it should be noted that the actual state and composition of the hydrocarbon species on the Pt surface may change due to catalytic activity of the surface. Since this catalytic behavior is also displayed by other Pt group metals, the conclusions that are drawn here could possibly be generalized to other precursors (with other hydrocarbon ligands) and even to other noble metal ALD processes.(17) For the ALD of Ru, Os, Rh, Ir and Pt with O_2 as a reactant, a substrate temperature of at least 200°C is required to obtain deposition of high-quality films.(34-38) Furthermore, the nature of the precursor ligands does not seem to have a large influence on the lower limit of the temperature window. For Ir ALD for example, high-quality films can be deposited for substrate temperatures above ~220°C, regardless of whether Ir(EtCp)(COD), $Ir(acac)_3$, or (MeCp)Ir(CHD) precursor is used. All Pt-group metals show a similar ability to break C-H bonds of adsorbed species, independent of specific precursor ligands. Therefore, a reaction mechanism and temperature dependence similar to that of Pt ALD may also apply to other noble metal ALD processes.

Acknowledgments

This research has been supported financially by IMEC-NL, the Netherlands. The research of one of the authors (W.M.M. Kessels) is supported by the Netherlands Organization for Scientific Research (NWO) and the Technology Foundation STW through the VICI program on “Nanomanufacturing”. Special thanks to Janneke Zeebregts, Ries van de Sande, and Joris Meulendijks for their technical support.

Bibliography

1. K. J. Albert, N. S. Lewis, C. L. Schauer, G. A. Sotzing, S. E. Stitzel, T. P. Vaid, and D. R. Walt, *Chemical Reviews* **100**, 2595 (2000).
2. H. Seo, T. Endoh, H. Fukuda, and S. Nomura, *Electronics Letters* **33**, 535 (1997).
3. K. Tsukada, T. Kiwa, T. Yamaguchi, S. Migitaka, Y. Goto, and K. Yokosawa, *Sensors and Actuators B-Chemical* **114**, 158 (2006).
4. M. S. H. Abadi, M. Gholizadeh, and A. Salehi, *Sensors and Actuators B-Chemical* **141**, 1 (2009).
5. M. Zhang, Z. Yuan, J. Song, and C. Zheng, *Sensors and Actuators B: Chemical* **148**, 87 (2010).
6. X. Y. Xue, Z. H. Chen, C. H. Ma, L. L. Xing, Y. J. Chen, Y. G. Wang, and T. H. Wang, *Journal of Physical Chemistry C* **114**, 3968 (2010).
7. D. Haridas, K. Sreenivas, and V. Gupta, *Sensors and Actuators B: Chemical* **133**, 270 (2008).
8. D. J. Comstock, S. T. Christensen, J. W. Elam, M. J. Pellin, and M. C. Hersam, *Advanced Functional Materials* **20**, 3099 (2010).
9. D. Haridas, A. Chowdhuri, K. Sreenivas, and V. Gupta, *Sensors and Actuators B-Chemical* **153**, 89 (2011).
10. T. Aaltonen, M. Ritala, T. Sajavaara, J. Keinonen, and M. Leskelä, *Chem. Mater.* **15**, 1924 (2003).
11. T. Aaltonen, A. Rahtu, M. Ritala, and M. Leskelä, *Electrochem. Solid-State Lett.* **6**, C130 (2003).
12. W. M. M. Kessels, H. C. M. Knoops, S. A. F. Dielissen, A. J. M. Mackus, and M. C. M. van de Sanden, *Appl. Phys. Lett.* **95**, 013114 (2009).
13. S. T. Christensen and J. W. Elam, *Chem. Mater.* **22**, 2517 (2010).
14. W. Setthapun, W. D. Williams, S. M. Kim, H. Feng, J. W. Elam, F. A. Rabuffetti, K. R. Poeppelmeier, P. C. Stair, E. A. Stach, F. H. Ribeiro, J. T. Miller, and C. L. Marshall, *J. Phys. Chem. C* **114**, 9758 (2010).
15. H. C. M. Knoops, A. J. M. Mackus, M. E. Donders, M. C. M. van de Sanden, P. H. L. Notten, and W. M. M. Kessels, *Electrochem. Solid-State Lett.* **12**, G34 (2009).
16. S. D. Elliott, *Langmuir* **26**, 9179 (2010).
17. A. J. M. Mackus, N.M. Leick, L. Baker, and W. M. M. Kessels, *Chem. Mater.* **24**, 1752 (2012).

18. E. Langereis, S. B. S. Heil, H. C. M. Knoops, W. Keuning, M. C. M. van de Sanden, and W. M. M. Kessels, *J. Phys. D: Appl. Phys.* **42**, 073001 (2009).
19. H. C. M. Knoops, E. Langereis, M. C. M. van de Sanden, and W. M. M. Kessels, *Journal of Vacuum Science & Technology A* **30** 010801 (2012).
20. Stanford research systems user manual QMS 100 series gas analyzer 2000).
21. Y. Itikawa, *J. Phys. Chem. Ref. Data* **31**, 749 (2002).
22. H. C. Straub, D. Lin, B. G. Lindsay, K. A. Smith, and R. F. Stebbings, *J. Chem. Phys.* **106**, 4430 (1997).
23. J. J. L. Mulders, L. M. Belova, and A. Riazanova, *Nanotechnology* **22** 055302 (2011).
24. R. B. Getman, Y. Xu, and W. F. Schneider, *J. Phys. Chem. C* **112**, 9559 (2008).
25. G. N. Derry and P. N. Ross, *Surf. Sci.* **140**, 165 (1984).
26. F. Zaera, *Surf. Sci.* **262**, 335 (1992).
27. F. Zaera and H. Hoffmann, *J. Phys. Chem.* **95**, 6297 (1991).
28. W. L. Manner, G. S. Girolami, and R. G. Nuzzo, *Langmuir* **14**, 1716 (1998).
29. A. L. Marsh, D. J. Burnett, D. A. Fischer, and J. L. Gland, *Journal of Physical Chemistry B* **107**, 12472 (2003).
30. N. R. Avery, *J. Electron Spectrosc. Relat. Phenom.* **39**, 1 (1986).
31. N. R. Avery, *Surf. Sci.* **146**, 363 (1984).
32. C. T. Campbell, J. M. Campbell, P. J. Dalton, F. C. Henn, J. A. Rodriguez, and S. G. Seimanides, *J. Phys. Chem.* **93**, 806 (1989).
33. A. Shavorskiy, T. Eralp, M. J. Gladys, and G. Held, *J. Phys. Chem. C* **113**, 21755 (2009).
34. T. Aaltonen, M. Ritala, and M. Leskelä, *Electrochem. Solid-State Lett.* **8**, C99 (2005).
35. J. Hämäläinen, T. Sajavaara, E. Puukilainen, M. Ritala, and M. Leskelä, *Chemistry of Materials*, **25**, 1656 (2011).
36. T. Aaltonen, M. Ritala, V. Sammelselg, and M. Leskelä, *J. Electrochem. Soc.* **151**, G489 (2004).
37. T. Aaltonen, M. Ritala, Y. L. Tung, Y. Chi, K. Arstila, K. Meinander, and M. Leskelä, *J. Mater. Res.* **19**, 3353 (2004).
38. T. Aaltonen, P. Alen, M. Ritala, and M. Leskelä, *Chem. Vap. Deposition* **9**, 45 (2003).

Chapter 5

Plasma-assisted Atomic Layer Deposition of Conformal Pt Films in High Aspect Ratio Trenches

Abstract

To date, conventional thermal atomic layer deposition (ALD) grown from (MeCp)PtMe$_3$ vapor and O$_2$ gas at 300 °C, has been the method of choice to deposit high-quality Pt thin films. Plasma-assisted ALD of Pt using O$_2$ plasma can offer several additional advantages over thermal ALD, such as faster nucleation and deposition at lower temperatures. In this work, it is demonstrated that plasma-assisted ALD, also allows for the deposition of highly conformal Pt films in high aspect ratio trenches with aspect ratios (ARs) of 3, 9, 22, and 34. Scanning electron microscopy (SEM) inspection revealed that the conformality of the deposited Pt films was 100 % within the error margin in trenches with ARs up to 34. These results were corroborated by high-precision layer thickness measurements by transmission electron microscopy (TEM) for trenches with an AR of 22.

Introduction

Platinum is a noble metal that is widely used as a catalyst driving chemical reactions at a commercial scale. It has the ability to break certain bonds in molecules adsorbed on its surface, while its inertness as a noble metal makes it chemically sTable 5.1n oxidizing atmospheres. In addition, Pt has favorable electrical properties such as a high work function of 5.6 eV and a low resistivity of 10.5 µΩ·cm. These properties are very relevant for application of the material as a metal contact or electrode in various electronic devices. Using atomic layer deposition (ALD), thin films as well as nanoparticles of Pt can be deposited with excellent material properties, precise thickness control on the sub-nanometer level, and good layer uniformity over large substrate areas. ALD is a cyclic process, based on the self-limiting surface reactions between vapor-phase precursor or reactant molecules and the chemical species present on a substrate surface. For Pt, the thermal ALD process using (MeCp)PtMe$_3$ vapor and O$_2$ gas has been most popular (1). Using this ALD process, thin films and nanoparticles of Pt can even be deposited on challenging 3-D topologies (2-4). As a result, ALD of Pt has a large number of potential applications in nanoelectronic devices, catalytic converters, chemicals production, sensors and fuel cells (5-7).

In the thermal ALD process based on (MeCp)PtMe$_3$ and O$_2$ gas, the O$_2$ gas is catalytically dissociated by the Pt surface, leading to reactive O-atoms. Alternatively, instead of O$_2$ gas, an O$_2$ plasma can be used to supply reactive O-radicals directly from the gas phase to the surface. This reduces the activation energy barriers for the surface reactions, giving plasma-assisted ALD of Pt several advantages (8).

Firstly, Pt can be deposited at significantly lower temperatures using plasma-assisted ALD. This expands the applicability of Pt ALD to substrates that cannot withstand conventional Pt ALD temperatures, such as polymers, textile, and paper. The lower limit of the temperature window of thermal ALD (250 – 300 °C) is determined by the inability of O$_2$ molecules to dissociate at the carbon-covered Pt surface at lower temperatures (9). In plasma-assisted ALD the thermal dissociation of O$_2$ at the surface is no longer required to generate O-radicals. When using a so-called ABC-type of

ALD process in which the O_2 plasma is followed by an H_2 plasma, Pt films can even be deposited at room temperature (10).

A second advantage of plasma-assisted ALD is the ability to deposit PtO_x as well as metallic Pt by controlling the precursor and O-radical dose. The composition of the material has been shown to depend on the substrate temperature, where for increasing temperatures, higher O_2 plasma exposures and/or shorter Pt-precursor exposures are required to obtain PtO_x (11). At low temperatures, e.g. at room temperature, making use of an O_2 plasma always leads to the deposition of PtO_x. To reduce the PtO_x to Pt, H_2 gas or an H_2 plasma can be supplied (10).

A third advantage of the plasma-assisted process is its fast Pt-nucleation on oxide surfaces. Generally, film nucleation of Pt on such substrates is relatively hard to accomplish when using thermal ALD due to the absence of catalytic Pt-species at the start of the process (12). Precursor adsorption on a bare oxide substrate is most likely not the limiting factor (9). However, this only results in the deposition of single Pt-atoms, which are not sufficiently effective in dissociating O_2 catalytically. Mackus *et al.* showed that exposure to O_2 gas enhances the diffusion of Pt atoms over the oxide surface, leading to the growth of Pt-islands (12). They observed that at higher O_2 pressures or for longer dosing times, these islands grow faster. Once these Pt islands have formed, O_2 dissociation and spill-over of O-atoms becomes more effective which in turn facilitates the overall ALD reactions (13). Thermal ALD of Pt on oxide surfaces therefore displays a relatively long nucleation delay depending on the O_2 exposure. However, this nucleation delay is absent or significantly reduced when using an O_2 plasma because the dissociation of O_2 is not the limiting factor. Moreover, the O-radicals present in the plasma may also enhance the diffusion of Pt-atoms over the oxide surface.

The difference in nucleation between thermal and plasma-assisted ALD on SiO_2 is illustrated in Figure 5.1. In this figure, the thickness of deposited Pt films as measured by in situ spectroscopic ellipsometry (SE) is plotted as a function of the number of cycles. For the O_2 exposure used for all experiments described in this work (0.06 Torr O_2 for a duration of 5 s) the nucleation delay for thermal ALD of Pt is approximately 300 cycles, while the plasma-assisted process has almost no nucleation delay. Interestingly, thermal ALD of Pt does not display a nucleation delay when this takes place on pre-deposited Pt seed layers as shown in Figure 5.1 (14). When the plasma-assisted ALD process is used to deposit a thin Pt seed-layer, the growth per cycle (GPC) of the subsequent thermal process on this seed layer is similar to that of the plasma-assisted process (0.047 ± 0.004 vs. 0.049 ± 0.004 nm/cycle, respectively).

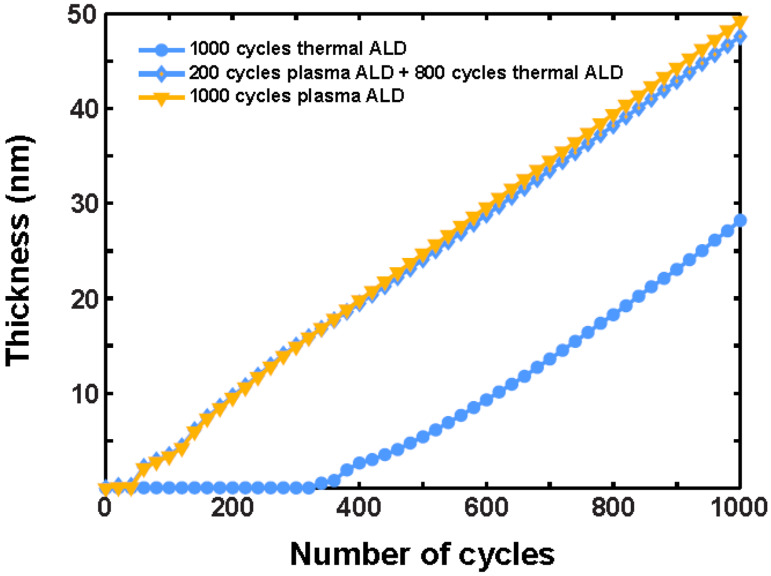

Figure 5.1. *The thickness of Pt films deposited on SiO_2 as a function of number of cycles, as measured with in situ spectroscopic ellipsometry. During every cycle, the reactant step consisted of 5 s exposure to O_2 at a pressure of 0.06 Torr. Furthermore, for plasma-assisted ALD cycles an O_2 plasma was ignited for 0.5 s during this 5 s exposure to O_2. For thermal ALD, growth starts after approximately 300 cycles. For plasma-assisted ALD growth takes off almost immediately. If 200 cycles of plasma-assisted ALD are used to deposit a Pt seed-layer, growth starts immediately for thermal ALD.*

The ability to deposit films conformally in high aspect ratio structures is a very powerful feature of ALD. While excellent conformality has been demonstrated for the thermal Pt ALD process (2), it is less trivial to reach saturation during plasma-assisted ALD. To achieve good conformality, saturation of the surface reactions during both the precursor and reactant step must be reached throughout the entire 3D feature. However, during the O_2 plasma step the dose required to reach saturation is often influenced by the surface recombination of the plasma radicals. This is caused by the reduction of the O-radical flux inside a trench where these radicals undergo many collisions while diffusing down into the trench. In fact, surface recombination of plasma radicals is considered to be a major challenge in reaching conformality in high aspect ratio structures using plasma-assisted ALD. Therefore, obtaining conformal film growth using plasma-assisted ALD of Pt is not at all trivial. Indeed, a previous study of plasma-assisted ALD of Pt inside HAR trenches showed a conformality of only 65 % when using the deposition conditions as determined for optimized planar saturation (15).

In this Chapter, the conformality that can be reached for Pt films using plasma-assisted ALD in HAR trenches has been investigated, based on the process using $(MeCp)PtMe_3$ vapor and O_2 plasma. This process might serve as a model system for metal ALD in general, since very few studies have been reported on noble metal plasma-assisted ALD in HAR features, as we will show below. We will first discuss the influence of sticking and recombination probabilities on the particle dose required for saturation for ALD of films in high aspect ratio trenches in more detail. To examine the conformality that can be achieved for Pt ALD, films were deposited in trenches with *AR*s up to 34. Scanning electron microscopy (SEM) images were used to determine the thickness profiles of the deposited Pt films. Furthermore, transmission electron microscopy (TEM) was used to determine a high-resolution thickness profile of a trench with an *AR* of 22, giving detailed statistical information on the conformality.

ALD in high aspect ratio features

Usually, ALD processes are optimized for planar geometries before deposition on 3D features is attempted. Whether or not significant adjustments to the particle doses are required for deposition on 3D features depends on the deposition regime which holds for the process. Three deposition regimes have been identified for ALD film growth in high aspect ratio features: 1) the reaction-limited (16), 2) the diffusion-limited (16,17), and 3) the recombination-limited regime (18). The main factors determining each of these regimes are the aspect ratio (*AR*) of the feature, the sticking probability s of the precursor/reactant, and the recombination probability r when using species with limited lifetime such as plasma radicals or O_3. The sticking probability s describes the reaction probability per collision whereby a particle is lost to the surface while contributing to the ALD surface chemistry. These reactions also include reactions other than sticking. The recombination probability r represents the recombination efficiency of e.g. O-radicals from the gas phase recombining with surface O-atoms to form molecular oxygen. In this case, the reaction does not contribute to the ALD surface chemistry.

The regimes are schematically depicted in Figure 5.2. In this figure the thickness can be interpreted either as the profile resulting from a process not yet in saturation or as the evolution of the film growth in the trench *during* the dosing step. For saturated conditions the thickness would be conformal by definition. Although the separation between the regimes is not sharply defined they can be described as follows (18):

1. Cases with $s << 16/AR^2$ are in the *reaction-limited* regime (Figure 5.2 (a)) (16). Due to the relatively low sticking probability s, particles can reach the bottom of the trench relatively easily and a (constant) particle density can in principle build up inside the trench. Therefore, growth occurs simultaneously throughout the entire trench until saturation is reached. Almost no increase in dose is required with increasing AR as long as this condition is satisfied.
2. Cases with $s >> 16/AR^2$ are in the *diffusion-limited* regime (Figure 5.2 (b)) (16). Due to the relatively high sticking probability s of the particles, the deeper parts of the trench will only be reached after the top part of the trench has become saturated. In this regime therefore, a moving deposition front is observed. An increase in *AR* leads to a strong increase in the required dose for saturation.
3. ALD growth with $AR\sqrt{r} \geq 1.3$ occurs in the *recombination-limited* regime (Figure 5.2 (c)) (18). Surface recombination losses make it more difficult for the particles to reach the deeper parts of the trenches. In this regime, growth occurs throughout the trench but the rate can be significantly reduced at places deeper in the trench, depending on r. Hence, the dose for saturation depends strongly on r.

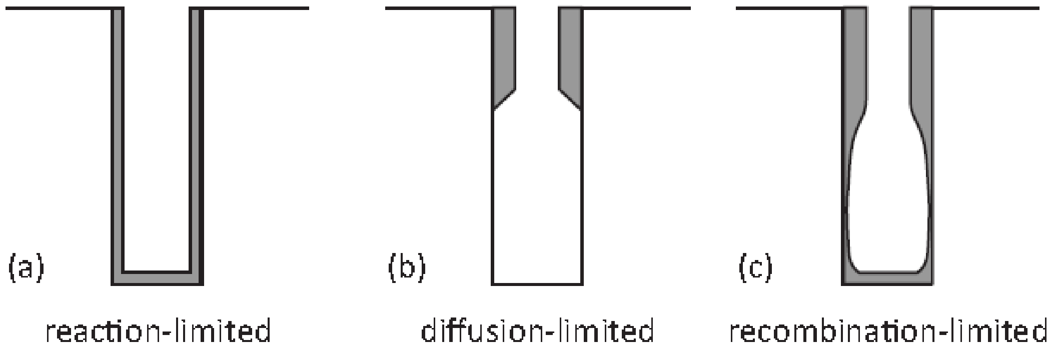

Figure 5.2. *Schematic representation of the three deposition regimes that can be distinguished for ALD in high aspect ratio features: (a) reaction-limited regime with growth occurring simultaneously in the entire trench until saturation is reached; (b) diffusion-limited regime in which a downward moving saturation front is observed; and (c) recombination-limited regime in which growth is reduced in the regions deeper in the trench due to surface recombination of radical species (in this case the condition of saturation is fulfilled last near the bottom of the trench) (18).*

As shown in Chapter 3, for planar surfaces the particle dose required to reach saturation of the surface reactions (i.e. saturation dose) scales with $1/s$ (i.e. s^{-1}), when $r = 0$. The impact of s on the saturation dose required for HAR trenches, is shown in Figure 5.3. The results were obtained by a Monte Carlo simulation similar to the one used by Knoops *et al.* (18). The solid lines in Figure 5.3 show the saturation dose normalized with respect to the dose required for $AR = 0$ (i.e. planar geometry) as a function of AR for $s = 1$ and $s = 0.001$. As can be seen, the normalized saturation dose for $s = 0.001$ hardly increases for increasing AR, while the normalized saturation dose for $s = 1$ shows a significant increase. Therefore, for relatively high values of s, the saturation dose for planar surfaces is relatively low, but the saturation dose for HAR features increases strongly as a function of AR. For relatively low values of s, the saturation dose for planar surfaces is relatively high (as it scales with s^{-1}), but the saturation dose does not increase strongly for higher *AR*s.

The second parameter that can have a large impact on achieving conformality in HAR structures for the case of plasma-assisted ALD is the surface recombination probability of plasma radicals r. For example, the reported surface recombination efficiency for O-radicals on Pt is 0.01 (19). Once these O-radicals have recombined they are lost and can no longer contribute to the ALD surface reactions. The formed O_2 however, can still participate in surface reactions (for certain ALD process) but no longer as a radical species. During their diffusion towards the bottom of a HAR trench, O-radicals will generally undergo several collisions with the trench wall, thereby increasing the overall probability of recombination. Knoops *et al.* have shown to what extent surface recombination losses may lead to non-conformality in HAR trenches (18). The influence of *r* on the normalized saturation dose as a function of *AR* is shown by the dashed lines in Figure 5.3. As shown, for an aspect ratio of 34, increasing *r* from 0 to 0.01 will increase the normalized saturation dose by a factor of ~5 for both *s* = 1 and 0.001.

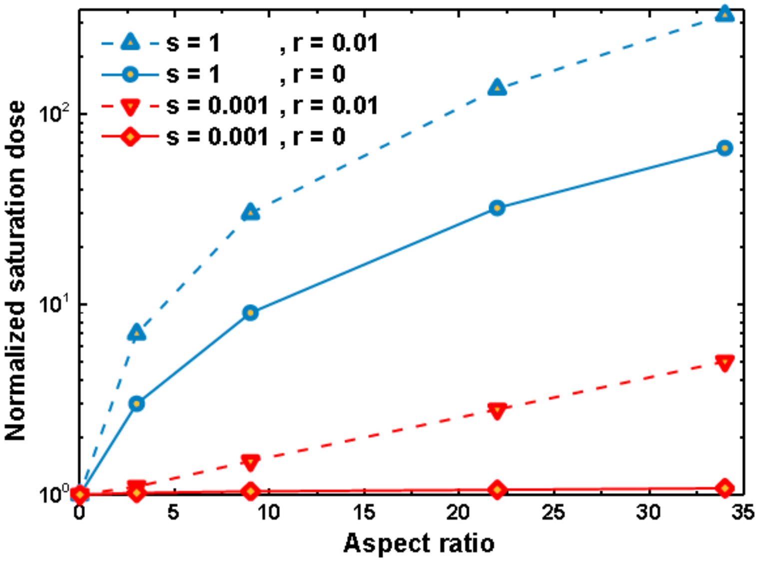

Figure 5.3. *The normalized saturation dose for particles with sticking probabilities s = 1 and s = 0.001, and surface recombination probabilities r = 0 and r = 0.01. The normalized saturation dose is shown as a function of the aspect ratio of the trench. The data have been obtained from Monte Carlo simulations similar to those described by Knoops et al. (18).*

The surface recombination probability *r* depends on the nature of the radical, on the material of the trench wall surface, and on the surface species present. The value of *r* can also vary with the substrate temperature. It has been reported that on metal oxides the recombination probabilities for O-radicals and H-radicals are generally lower than those on metals (18). Indeed, recent studies have shown that many metal oxides can be deposited conformally in HAR structures using plasma-assisted ALD. Table 5.1 lists several recent conformality data reported for various plasma-assisted ALD processes, alongside the reported surface recombination probabilities of the radicals (where available). The table shows some very good results for HAR features (*AR* ≥ 20) covered with metal oxides and nitrides. For pure metals however, only reasonable conformality for relatively low aspect ratio features (*AR* ≤ 5) was reported. To our knowledge, plasma-assisted ALD of Pt in HAR structures has not been reported yet.

Table 5.1. Overview of recent reports on the conformality reached using plasma-assisted ALD of several oxides, nitrides, and metals. The final column gives the recombination probability if reported.

Reference	Material	*AR*	Conformality*	Precursor	Plasma	Recombination probability (18)
(20)	SiO_2	60	Good	$SiH(N(CH_3)_2)_3$	O_2	0.0002
(20)	HfO_2	60	Perfect	$Hf(N(CH_3)(C_2H_5))_4$	O_2	
(20)	Al_2O_3	27	Good	$Al(CH_3)_3$	O_2	
(20)	TiO_2	27	Good	$Ti(OCH(CH_3)_2)_4$	O_2	0.0021
(20)	Ta_2O_5	20	Good	$Ta(OEt)_5$	O_2	
(20)	Ag	60	Very poor	$Ag(fod)(PEt_3)$	H_2	
(21)	RuTaN	7.5	Uniform	$Ru(EtCp)_2$	NH_3	
(22)	Al_2O_3	20	33 %	$Al(CH_3)_3$	O_2	0.0021
(22)	CoO_x	10	Very poor	$CoCp_2$	O_2	0.0049
(23)	Ru	4	0.86	$Ru(EtCp)_2$	NH_3	
(23)	Ru	4	0.97	$Ru(EtCp)_2$	NH_3	
(24)	TaN	7	100 %	$(CH_3)_3CNTa(NC_2H_5(CH_3))_3$	H_2	
(25)	TiN	20	100 %	$C_8H_{24}N_4Ti$	NH_3-Ar-H_2	
(26)	TaN_x	10	Almost 100 %	$C_{16}H_{39}N_4Ta$	H_2/N_2	
(27)	TiN	10	Excellent	$C_8H_{24}N_4Ti$	NH_3	
(28)	TaN	10	~ 100 %	$C_{16}H_{39}N_4Ta$	H	

* The nomenclature for conformality is shown here as reported by the authors of the different publications. We note here specifically, that different definitions of conformality are being used. Many studies do not provide a quantitative measure for or a universal definition of conformality. When numbers are provided, these are usually based on the layer thickness at the trench bottom compared to that at the planar top or the central part of the trench wall. Finally, care should be taken when comparing *AR* values from different studies, as some of the HAR trenches have slanted walls, resulting in an overestimation of the actual aspect ratio.

Experimental

The Pt depositions were performed in an open-load ALD reactor, consisting of a deposition chamber with a volume of ~0.009 m^3 that contained a substrate heating stage. On top of the chamber an inductively coupled plasma source was located. The deposition chamber is connected to a turbomolecular pump through a valve. The walls of the deposition chamber were heated to 80 ± 10 °C while the substrate stage was heated to 300 ± 5 °C during deposition.

Pt ALD films were deposited on Si trench-samples with trench arrays etched with deep reactive ion etching (DRIE) (29). The trenches had the following *AR*s and dimensions (depth [µm] x width [µm]): AR 3 (30 x 10), AR 9 (27 x 3), AR 22 (22 x 1), AR 34 (17 x 0.5). The Si trench-substrates were covered with approximately 100 nm of thermally grown SiO_2 after the etching of the trenches. Each of the samples had a planar top surface area of approximately 3 cm^2 and contained 80 trenches with a length of 4 mm of each aspect ratio. Therefore, the loading effect from the additional surface due to the presence of the trenches (~0.64 cm^2) in the samples is negligible compared to the total reactive surface in the deposition chamber (~0.2 m^2).

For ALD of Pt, saturation of planar surfaces can be achieved after a precursor pulse of 1 s, when the precursor container is heated to 30 °C and N_2 is used as a carrier gas. To obtain good conformality in the trenches for the plasma-assisted ALD process based on $(MeCp)PtMe_3$ and O_2, several parameters should first be evaluated. Experiments shown in Chapter 3 indicated that the $(MeCp)PtMe_3$ precursor has near unity sticking probability. For O-radicals, the sticking probability for chemisorption on single crystalline Pt (100) is reported to be 1 for O-coverage degrees that are typical for ALD (30). Therefore, we assume that the sticking probability for O-radicals during ALD of Pt is also close to 1. Furthermore, the reported recombination probability for O-radicals on Pt is 0.01 (19). On the basis of the results presented in Figure 5.3 it can be concluded that both the precursor and O_2 plasma doses for planar surfaces need to be increased for conformal deposition in HAR trenches.

To provide the increased precursor dose for the HAR depositions described in this work, the precursor step consisted of a 3 ± 0.1 s pulse with the precursor container being heated to 70 ± 5 °C and without making use of a carrier gas. Furthermore, during the precursor pulse the deposition chamber was closed off from the pump to increase the dose and ensure efficient precursor usage. The O_2 plasma exposure time that is usually employed for planar surfaces is 0.5 s. For the deposition in the HAR trenches, the O_2 plasma exposure time was increased to 3 ± 0.1 s.

Figure 5.4 shows cross-section SEM images of a trench with an *AR* of 22 which was coated with a Pt ALD film with a thickness of approximately 60 nm. Figure 5.4 (a) shows an overview of the entire trench with an *x,y,z* coordinate system that will be used throughout this work. In Figure 5.4 (b), a close-up of the top part of the trench is shown, where the Si substrate, the thermal SiO_2 layer, and the ALD-deposited Pt film are all indicated. As can be seen, the trench walls show a periodic roughness (so-called scallops) in the *z*-direction, which is characteristic for the Bosch DRIE etching process (29). The scallop curvature is most pronounced in the top part of the etched trench, but often it can still be seen in the bottom part of trenches, such as is clear from Figure 5.4 (c). Furthermore, a mask-induced line edge roughness in the y-direction can be seen. Thus, the deposited Pt layer displays scallops and line edge striations in the respective directions. Similar images showed that the trenches *with AR* = 34 had non-straight walls. Moreover, these trenches were often collapsed. This made an accurate determination of the conformality of the *AR* = 34 more challenging.

Results

Conformality studies using SEM

A deposition of 700 cycles was carried out with a 3 s precursor pulse and 3 s O_2 plasma. SE measurements performed on a simultaneously coated planar SiO_2 substrate showed a Pt film thickness of 33 ± 1 nm. This yields a GPC of 0.047 nm/cycle, consistent with values reported in the literature (14). By using SEM images similar to those in Figures 4 (b) and (c) at different positions along the trenches, thickness profiles for the trenches with *AR* = 3, 9, 22, and 34 were determined.

The results are shown in Figure 5.5. Each data point indicates the average of 3 thickness values measured in a single SEM image at a certain normalized trench depth, i.e. the depth divided by the total depth of the trench. The shaded area indicates the typical error in determining the thickness for each data point. As can be seen, for each trench the measurement error in determining the thickness is larger than the variation in the thickness as a function of trench depth. Therefore, the conformality for each trench was calculated by taking the average thickness based on the 6 data points for that trench, and dividing this average thickness by the thickness on the planar substrate (~33 nm as measured by SE). The results for the conformality are shown in Table 5.2 for the trenches with *AR* = 3, 9, 22, and 34. As Table 5.2 shows, for each aspect ratio the conformality is 100% within the error margin. The average error in measuring the film thickness by using SEM however, is relatively large: approximately 4 nm, corresponding to ~12 % of the average thickness. To get a more detailed measure of the conformality, the thickness of the deposited Pt film was determined with high precision, using a cross-sectional TEM sample.

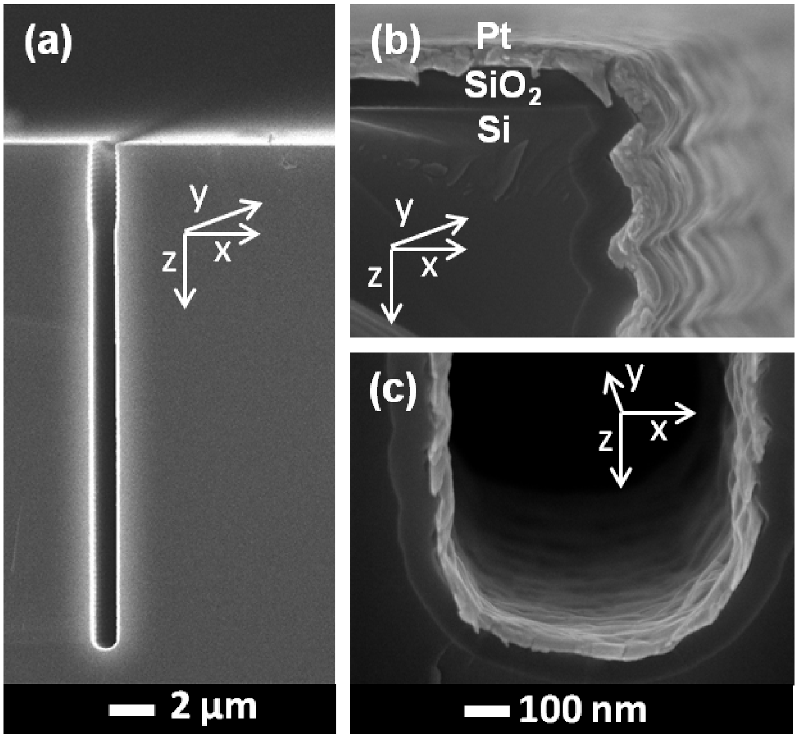

Figure 5.4. (a) Cross-section SEM image of a cleaved Si-wafer showing a trench with *AR* = 22. The y-axis is along the heartline of the trench. The wafer surface was thermally oxidized after etching the trenches. (b) Close-up SEM image of the top part of the trench. The Si-substrate, the thermally grown SiO_2 layer, and ALD Pt layer are all indicated. (c) Close-up SEM image of the bottom of the trench. Images (b) and (c) show scallops along the z-axis and line edge roughness along the y-axis.

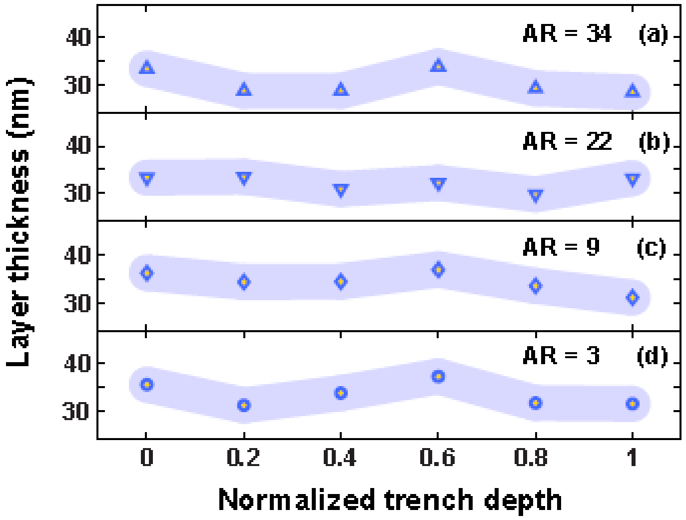

Figure 5.5. The thickness profile of the deposited Pt ALD film (700 cycles) as a function of the normalized trench depth for trenches with *AR* = 3, 9, 22, and 34. The gray-shaded areas indicate the average measurement error in the thickness values. A normalized trench depth of 0 corresponds to the area around and/or just inside the trench opening.

Table 5.2. The average Pt film thickness and conformality for each aspect ratio shown in Figure 5.5. The conformality is defined as the average thickness divided by the thickness of a planar reference sample, which was 33 nm. The error in the average thickness is the standard deviation, and the error in the conformality is the standard deviation divided by the thickness of the planar reference sample.

Aspect ratio	Average thickness (nm)	Conformality (%)
3	33.5 ± 2.5	102 ± 8
9	34.4 ± 2.1	104 ± 6
22	32.2 ± 1.5	98 ± 5
34	30.4 ± 2.5	92 ± 8

Conformality studies using TEM

To obtain more detailed information on the conformality of the Pt ALD layer, TEM analysis was performed for a trench with an *AR* of 22. This *AR* was chosen because of the structural imperfections of the trenches with an *AR* of 34. For the TEM analysis a deposition run with 1000 ALD cycles was carried out on a trench sample, with a precursor pulse of 3 s and a 1.5 s O_2 plasma. The shorter plasma exposure time (compared to the 3 s for the SEM sample) was considered sufficient since the goal of this deposition was the conformal deposition in trenches with an *AR* of 22 rather than the maximum *AR* of 34. SE measurements on a simultaneously deposited planar SiO_2 substrate showed a Pt thickness of 47.5 ± 1 nm, yielding a GPC of 0.048 nm/cycle. After ALD of Pt on the Si-trench sample, a TEM cross-section sample of a trench with *AR* = 22 was prepared by first cleaving the Si trench-substrate exactly through the trench heartline (y-z cleavageplane in Fig. 4). For imaging contrast purposes, the cleaved sample with the Pt film was covered with an SiO_2 layer (thickness ~ 25 nm) using electron beam induced deposition (EBID), followed by a protective carbon-rich Pt capping layer (thickness ~200 nm) using ion beam induced deposition (IBID). Subsequently, a lift-out TEM lamellar sample was prepared using focused ion beam (FIB) milling, orthogonal to the cleavage plane (i.e. in the x-z-plane). This provided a sample with the sidewall of the 22 µm deep trench being fully electron transparent, allowing a more accurate determination of the layer thickness as a function of trench depth using high angle annular dark field (HAADF) scanning TEM.

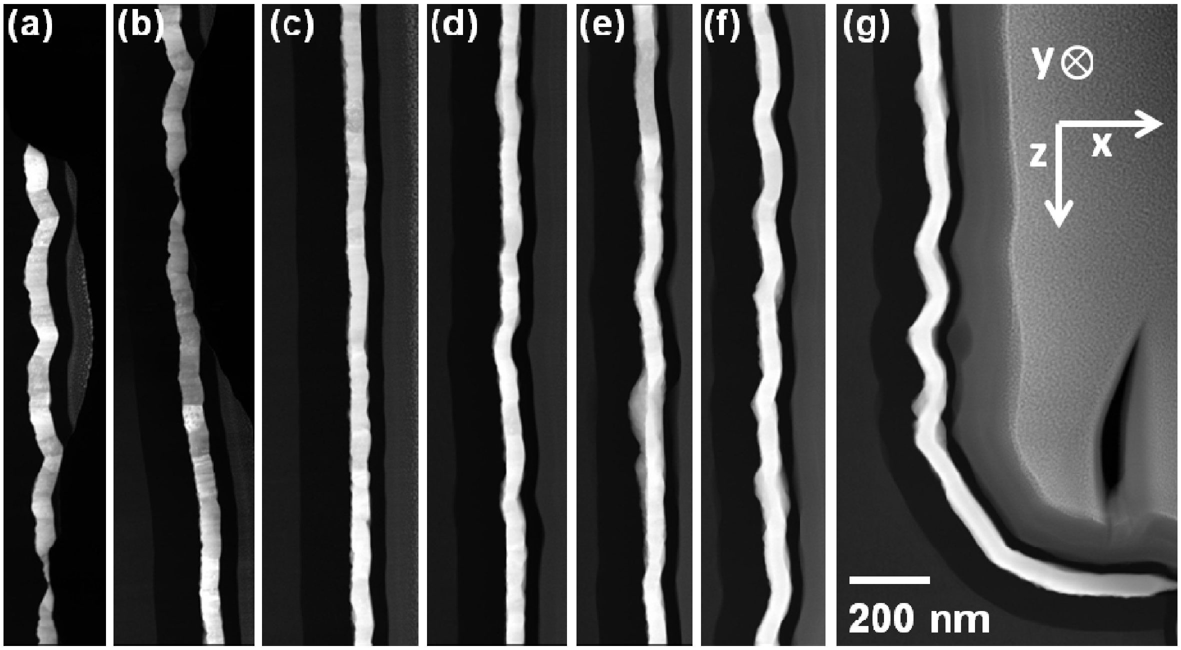

Figure 5.6. HAADF-STEM images of different segments along a trench with 22 µm depth and 1 µm width, showing segments near the top (a), at a trench depth of approximately 2 µm (b) , 3 µm (c), 10 µm (d), 16 µm (e), and 18 µm (f), and at the trench bottom (g).

A representative selection from a series of HAADF-STEM images of the plasma-assisted ALD deposited Pt layer in the trench with *AR* of 22 is shown in Figure 5.6 (a-g). Figure 5.6 (a) shows a segment near the top of the trench. The following cross-sectional images each show an increasingly deeper part of the trench, ending with the bottom part in Figure 5.6 (g). The deposited Pt layer appears as very bright, encapsulated in the darker thermally grown SiO_2 to its left, and the SiO_2 capping layer to its right. Figures 6 (a) and (b) both show the same small segment where the deposited Pt layer appears to be very thin. This is, however, not caused by poor conformality but by sample preparation: at this position, the protective EBID layer was locally milled away resulting in the removal of the Pt layer of interest. Some images, such as the one in Figure 5.6 (e) show somewhat blurry Pt segments, which is caused by the superposition of shifted segments caused by the periodic curvature of the trench walls in the y-direction. Figures 6 (a) and (b) furthermore show the individual grains of the deposited Pt. Above all, Figures 6 (a-g) show that Pt has been deposited conformally throughout the trench.

Figure 5.7 shows the thickness profile, i.e. the thickness of the deposited Pt as a function of trench depth for a trench with AR = 22. In determining the thickness, the orientation of a certain segment due to the scallops was taken into account. This orientation could be at positive, negative, or normal angle with respect to the y-z plane. Also, the thickness at the trench bottom is given. The conformality for each orientation was determined by taking the average thickness and dividing this by the thickness on the planar substrate (47.5 nm). The error in the conformality is determined by taking the standard deviation in the thickness divided by the thickness on the planar substrate. Table 5.3 shows the average thickness, conformality, and number of data points for each angle of the data points in Figure 5.7. As can be seen, 100 % conformality is within the error margin of the normal segments of the deposited Pt.

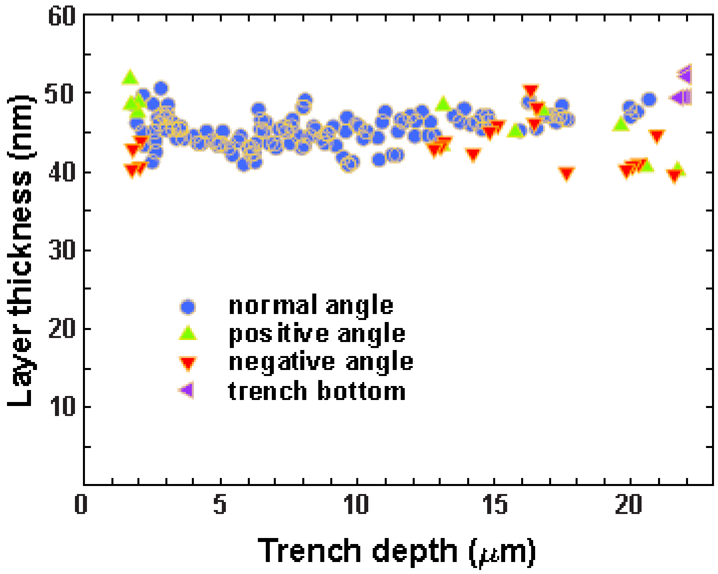

Figure 5.7. Thickness profile of the deposited Pt layer as a function of trench depth for a trench with AR = 22. The data points for the layer thickness, 160 in total, have been extracted from the TEM images shown in Figure 5.6. A distinction is made between segments with different sidewall angles or belonging to the trench bottom.

Table 5.3. Statistics on the data points shown in Figure 5.7. The average Pt film thickness, conformality, and number of data points is given for data points corresponding to film segments with normal, positive, and negative angle, and to the trench bottom. The conformality is defined as the average thickness divided by the film thickness on a planar reference sample, which was 47.5 nm thick. The error in the thickness is the standard deviation, and the error in the conformality is the standard deviation divided by the film thickness of the planar reference sample.

Angle	**Average thickness (nm)**	**Conformality (%)**	**Number of data points**
Normal	45.3 ± 2.7	95 ± 6	124
Positive	46.1 ± 3.6	97 ± 8	11
Negative	42.7 ± 3.8	90 ± 8	20
Bottom	50.6 ± 1.6	107 ± 3	5
Total	45.2 ± 2.8	95 ± 6	160

The average thickness, standard deviation, and the conformality for segments at normal angle are comparable to the values averaged over all the segments. This is due to the fact that the normal segments comprise 78 % of the total number of data points (124 out of 160). Segments with positive angle show a somewhat higher average thickness (46.1 nm) and also a higher standard deviation. For segments with negative angle the average thickness is lower (42.7 nm), with again a higher standard deviation. This could indicate that precursor (or oxygen) saturation may not be entirely complete, and that overhang of the scallops may cause a slight shadowing effect, reducing the particle flux towards negatively slanted segments. The average Pt thickness at the bottom of the trench is somewhat higher at 50.6 nm (based on 5 data points), which is within the 95 %-confidence interval of the thickness values measured on the trench wall (assuming a normal distribution of the measurement error). The average Pt film thickness inside the trench of 45.2 ± 2.7 nm yields a GPC of 0.045 nm/cycle for 1000 cycles, and corresponds well with the thickness of 47.5 ± 1 nm that was measured on the planar substrate using SE.

Discussion and conclusion

The goal of this work was to determine the conformality that could be reached in HAR trenches using plasma-assisted ALD based on (MeCp)PtMe$_3$ and O$_2$ plasma. The (MeCp)PtMe$_3$ molecules and O-radicals have close-to-unity sticking probabilities, and the recombination probability of O-radicals on Pt has been reported to be 0.01 (8). These relatively high sticking and recombination probabilities require a significant increase in the precursor and O$_2$ plasma doses in order to reach saturation of the surface reactions throughout HAR trenches. Based on cross-section SEM imaging, we conclude that using a precursor and O$_2$ plasma exposure time of 3 s, 100 % conformality can be achieved within the error margin in trenches with an aspect ratio of up to 34. Detailed TEM images showed that by using a precursor exposure time of 3 s and an O$_2$ plasma exposure time of 1.5 s, 100 % conformality is obtained within the error margin in trenches with an aspect ratio of up to 22.

We finally note here, that gaseous O$_2$ molecules comprise the majority of the plasma species. They are not hindered by recombination and will also contribute to Pt growth. This implies that the conformal deposition of Pt inside the trenches can be ascribed to a thermal ALD component in addition to a plasma ALD component. However, the Pt film thickness inside the trench shown in Figure 5.6 corresponds well with the measured thickness of ~47.5 nm on the planar substrate, and is consistent with a GPC of 0.045 nm/cycle for 1000 cycles. Figure 5.1 shows that without the contribution of O-radicals from the plasma (at least during the nucleation stage) the thermally deposited Pt film would be considerably thinner. Purely thermal ALD would have resulted in a Pt film thickness of only ~28 nm. Therefore, from the film thickness achieved from growth without a nucleation delay, one can conclude that the O-radicals have a genuine contribution to the film growth inside the trench.

Acknowledgments

This work has been carried out within the framework of NanoNextNL, a micro- and nanotechnology program of the Dutch Ministry of Economic Affairs, Agriculture and Innovation (EL&I) and 130 partners. This research has been supported financially by IMEC-NL, part of the Holst Centre, The Netherlands. The research of one of the authors (W.M.M. Kessels) is supported by the Netherlands Organization for Scientific Research (NWO) and the Technology Foundation STW through the VICI program on "Nanomanufacturing". Thanks are due to K. de Peuter for acquiring and analyzing the SEM images, and to J.J.A. Zeebregts, M.J.F. van de Sande, and J.J.L.M. Meulendijks for their technical support.

Bibliography

1. J. Hämäläinen, M. Ritala, and M. Leskelä, *Chem. Mater.* **26**, 786 (2013).
2. D. J. Comstock, S. T. Christensen, J. W. Elam, M. J. Pellin, and M. C. Hersam, *Advanced Functional Materials* **20**, 3099 (2010).
3. G. Pardon, H. K. Gatty, G. Stemme, W. van der Wijngaart, and N. Roxhed, *Nanotechnology* **24,** 015602 (2013).
4. P. Shrestha, D. Gu, N. Tran, K. Tapily, H. Baumgart, and G. Namkoong, *Atomic Layer Deposition Applications 6* **33**, 127 (2010).
5. D. Haridas, A. Chowdhuri, K. Sreenivas, and V. Gupta, *Sensors and Actuators B-Chemical* **153**, 89 (2011).

6. M. J. Weber, A. J. M. Mackus, M. A. Verheijen, C. van der Marel, and W. M. M. Kessels, *Chem. Mater.* **24**, 2973 (2012).
7. A. Mackus, S. Dielissen, J. Mulders, and W. M. M. Kessels, *Nanoscale* **4**, 4477 (2012).
8. H. Profijt, S. Potts, M. van de Sanden, and W. M. M. Kessels, *Journal of Vacuum Science & Technology A* **29**, 050801 (2011).
9. Erkens I.J.M., A. J. M. Mackus, H. C. M. Knoops, Smits P., van de Ven T.H.M., F. Roozeboom, and W. M. M. Kessels, *ECS Journal of Solid State Science and Technology* **1**, 255 (2012).
10. A. J. M. Mackus, D. Garcia-Alonso, H. C. M. Knoops, A. A. Bol, and W. M. M. Kessels, *Chem. Mater.* **25**, 1769 (2013).
11. Erkens I.J.M., H. C. M. Knoops, T. F. Landaluce, A. J. M. Mackus, M. Verheijen, F. Roozeboom, and W. M. M. Kessels, *Accepted for publication in Chemical Vapor Deposition* (2014).
12. A. J. M. Mackus, M. A. Verheijen, N. m. Leick, A. A. Bol, and W. M. M. Kessels, *Chem. Mater.* **25**, 1905 (2013).
13. L. Baker, A. Cavanagh, D. Seghete, S. George, A. Mackus, W. Kessels, Z. Liu, and F. Wagner, *J. Appl. Phys.* **109**, 084333 (2011).
14. H. C. M. Knoops, A. J. M. Mackus, M. E. Donders, M. C. M. van de Sanden, P. H. L. Notten, and W. M. M. Kessels, *Electrochem. Solid-State Lett.* **12**, G34 (2009).
15. H. C. M. Knoops, *Atomic Layer Deposition: from Reaction Mechanisms to 3D - Integrated Microbatteries, PhD thesis, Eindhoven University of technology, chapter 5* (2011).
16. J. W. Elam, D. Routkevitch, P. P. Mardilovich, and S. M. George, *Chem. Mater.* **15**, 3507 (2003).
17. R. G. Gordon, D. Hausmann, E. Kim, and J. Shepard, *Chem. Vap. Deposition* **9**, 73 (2003).
18. H. C. M. Knoops, E. Langereis, M. C. M. van de Sanden, and W.M.M. Kessels, *J. Electrochem. Soc.* **157**, G241-G249 (2010).
19. D. S. Hacker, S. A. Marshall, and M. Steinberg, *J. Chem. Phys.* **35**, 1788 (1961).
20. M. Kariniemi, J. Niinisto, M. Vehkamaki, M. Kemell, M. Ritala, M. Leskela, and M. Putkonen, *Journal of Vacuum Science & Technology A* **30,** 01A115 (2012).
21. T. Chakraborty and E. T. Eisenbraun, *Journal of Vacuum Science & Technology A* **30,** 020604 (2012).

22. J. Dendooven, D. Deduytsche, J. Musschoot, R. Vanmeirhaeghe, and C. Detavernier, *J. Electrochem. Soc.* **157**, G111 (2010).
23. B. H. Choi, Y. H. Lim, J. H. Lee, Y. B. Kim, H. N. Lee, and H. K. Lee, *Microelectron. Eng.* **87**, 1391 (2010).
24. D. K. Kim, B. H. Kim, H. G. Woo, D. H. Kim, and H. K. Shin, *Journal of Nanoscience and Nanotechnology* **6**, 3392 (2006).
25. Y. J. Lee, *Mater. Lett.* **59**, 615 (2005).
26. H. Kim, C. Detavenier, O. van der Straten, S. M. Rossnagel, A. J. Kellock, and D. G. Park, *J. Appl. Phys.* **98**, 014308 (2005).
27. H. Kim, C. Lavoie, M. Copel, V. Narayanan, D. G. Park, and S. M. Rossnagel, *J. Appl. Phys.* **95**, 5848 (2004).
28. J. S. Park, H. S. Park, and S. W. Kang, *J. Electrochem. Soc.* **149**, C28 (2002).
29. F. et. al. Lärmer, *in Handbook of Silicon Based MEMS Materials and Technologies (ed. V. Lindroos et al.),Elsevier (Oxford, 2010) p. 349.* (2010).
30. J. F. Weaver, H. H. Kan, and R. Shumbera, *Journal of Physics-Condensed Matter* **20** 184015 (2008).

Chapter 6

Plasma-assisted Atomic Layer Deposition of PtO_x from $(MeCp)PtMe_3$ and O_2 Plasma[*]

Abstract

Atomic layer deposition (ALD) using $(MeCp)PtMe_3$ and O_2 gas or O_2 plasma is a well-established technique for the deposition of thin films of Pt, but the potential of ALD to deposit PtO_x has not been systematically explored yet. This work demonstrates how PtO_x can be deposited by plasma-assisted ALD in a temperature window from room temperature (RT) to 300 °C by controlling the O_2 plasma and $(MeCp)PtMe_3$ exposure. With increasing substrate temperature, the thermal stability of PtO_x decreases and the reducing activity of the precursor ligands increases. Therefore, longer O_2 plasma exposures and/or lower $(MeCp)PtMe_3$ exposures are required to obtain PtO_x at higher temperatures. Furthermore, it has been established that during the nucleation stage, PtO_x ALD starts by the formation of islands that grow and coalesce during the initial ~40 cycles. Closed-layer thin-films of PtO_x with an O/Pt ratio of 2.5 can be deposited at 100 °C with a minimal thickness of only ~2 nm. It has also been demonstrated that a conformality of ~90 % can be reached for PtO_x films in trenches with an aspect ratio of 9, when using optimized O_2 plasma and precursor exposure times.

---

[*] Accepted for publication in Chemical Vapor Deposition (2014)

Introduction

ALD is becoming the method of choice for ultrathin film deposition in nanoscale technology such as in state-of-the-art microelectronics, and it also shows great potential for use in applications such as catalysis, energy scavenging and storage devices, and sensors (1-4). ALD processes are available for a large number of materials, most prominently metal oxides and nitrides, and also some processes are available for metals (5). With ALD, these materials can be deposited with sub-nanometer growth control, very high uniformity, and excellent conformality over demanding surface topologies. Due to a growing interest in ALD, much effort is invested into understanding and improving existing ALD processes, and into the development of new processes. There is also a continued effort to expand the number of materials that can be deposited with ALD.

Recently, it has been shown that platinum oxide (PtO_x) can also be deposited using ALD (6,7). The deposition of PtO_x is more challenging compared to other metal oxides because Pt, as a noble metal, has a relatively high resistance against oxidation. For example, the ALD process using $(MeCp)PtMe_3$ and O_2 gas yields metallic Pt rather than PtO_x, despite the fact that O_2 acts generally as an oxidizing reactant (8). For the Pt ALD process using O_2 gas, the O_2 molecules catalytically dissociate at the Pt surface. The dissociated O atoms combust the precursor ligand fragments remaining from the previous half-cycle, leading to the reduction of the Pt and the formation of a chemisorbed oxygen layer which facilitates precursor adsorption in the next half-cycle. The temperature window for this process spans from approximately 250 to 300 °C. For higher temperatures, the precursor starts to thermally decompose. The lower limit of the temperature window is determined by ineffective O_2 dissociation at temperatures below ~250 °C. This has been attributed to the formation of a carbonaceous layer by the precursor ligands during the precursor pulse which blocks the catalytic dissociation of O_2 (9). The lower limit of the temperature window can be reduced significantly however, by making use of an O_2 plasma rather than O_2 gas (7). Since reactive O radicals are supplied from the gas phase by the plasma, there is no need to first dissociate the O_2 at the surface in order to participate in surface reactions. This means that the carbonaceous layer formed by the precursor ligands can be combusted at much lower temperatures, and as a result, Pt can be deposited at temperatures as low as room temperature using plasma-assisted ALD (7,9,10).

Without the need for O_2 dissociation at the surface, nucleation of the Pt film also proceeds faster in the case of plasma-assisted ALD (11). Generally, achieving nucleation of Pt on oxide surfaces such as SiO_2 and Al_2O_3 is challenging because of the absence of catalytically-active Pt that induces O_2 dissociation during the initial cycles (12). Precursor adsorption on a bare oxide substrate is not likely to be the limiting factor during nucleation (9). However, this only results in the deposition of Pt precursor fragments leading to insufficient catalytic activity for effective O_2 dissociation. Mackus *et al.* have shown that prolonged exposure to O_2 gas facilitates the diffusion of Pt species across the oxide surface, leading to ripening of Pt islands (12). Once these Pt nanoparticles have formed O_2 dissociation and spillover of O atoms can occur which in turn facilitates island growth (11). Subsequently, the growth manifests itself by the formation of nanoparticles that grow and coalesce to eventually form a closed layer. For Pt, a fully closed film is typically not obtained until a film thickness of at least 8 nm is reached (13).

The oxidizing reactant clearly plays a key role in Pt ALD, both for the surface chemical reactions with the adsorbed precursor species and, independently thereof, for the nucleation of Pt on oxide surfaces. The importance of the oxidizing reactant becomes even more evident when considering the possibility to deposit PtO_x. As was mentioned before, O_2 gas is generally not reactive enough for ALD of PtO_x which calls for stronger oxidizing reactants. In 2008, Hämäläinen *et al.* were the first to report on an ALD process for PtO_x, which made use of $Pt(acac)_2$ and O_3 (6). Although O_3 proved reactive enough to form PtO_x with an O/Pt ratio of 1.67, higher oxidation states of Pt were not reached. Furthermore, above 130 °C only metallic films were deposited. The lower limit of the relatively narrow temperature window was 120 °C (the sublimation temperature of the $Pt(acac)_2$ precursor). In 2009, Knoops *et al.* reported that PtO_x films with an O/Pt ratio of 2 can be deposited by plasma-assisted ALD using $(MeCp)PtMe_3$ and O_2 plasma (7). In their work, Knoops *et al.* focused mainly on the deposition of metallic Pt using this process. Remarkably, Knoops *et al.* found that PtO_x can be obtained instead of Pt when relatively long O_2 plasma exposure times are used (5 s) in a temperature range of 100 to 300 °C.

A detailed investigation of the PtO_2 process and the dependence of the composition (Pt versus PtO_x) on process parameters was beyond the scope of the work of Knoops *et al.* Therefore, in the present work, a more comprehensive study on plasma-assisted ALD of PtO_x using (MeCp)$PtMe_3$ and O_2 plasma is presented. In order to add PtO_x to the ALD materials toolbox, the process window was first established. Since this ALD process can lead to the deposition of both Pt and PtO_x, the composition of the deposited material was determined as a function of substrate temperature (T_{sub}), O_2 plasma exposure (more specifically, the plasma exposure time t_{plasma}), and exposure to the (MeCp)$PtMe_3$ precursor during the precursor pulse (the precursor pressure p_{prec}). Good control over the composition was demonstrated, and PtO_x has been deposited in a temperature window ranging from 30 to 300 °C. The material properties of the deposited PtO_x were also studied.

Another aspect ALD that has been studied in this work is the nucleation of PtO_x deposited by ALD. As mentioned before, the Pt ALD process is characterized by the formation of nanoparticles during the initial stage of growth. In catalysis applications, nanoparticles are often favored over thin-films because of their increased reactivity and their high surface to volume ratio (3,14,15). On the other hand, the onset of layer closure is important because it determines the minimal thickness that can be used for thin-film applications (16-18). Therefore, the nucleation stage of the PtO_x process was studied extensively in this work. The formation, growth, and coalescence of nanoparticles during the initial growth stage may depend on the wetting condition of the substrate surface, which will differ for substrates with different surface energies. Therefore, several substrate materials (Si, SiO_2, TiO_2, Al_2O_3) were used to study and compare the nucleation behavior and growth of PtO_x ALD.

A final topic that will be treated in this work is the conformality that can be achieved for ALD of PtO_x. Good film conformality in high aspect ratio structures is one of the key features of ALD. Given the use of a plasma in PtO_x ALD, achieving good conformality may not be trivial due to radical losses at the sidewall surfaces of the high aspect ratio structures. For example, plasma-generated oxygen radicals can recombine with an O atom at the Pt surface forming gaseous O_2, such that the radicals can no longer contribute to the ALD surface reactions. Knoops *et al.* show that plasma radical loss due to recombination at the surface can be a cause of poor conformality, depending on the surface recombination probability of the radicals (19). Therefore, the conformality of PtO_x films deposited in trenches with an aspect-ratio of 9 was studied. Process conditions have been optimized to reach good conformality, and a thickness profile of the PtO_x layer inside a trench was determined.

Experimental

ALD reactor: All depositions were performed in an open-load ALD reactor which is pumped by turbomolecular pump through a gate valve. An inductively coupled plasma source is connected to the top of the reactor through another gate valve. The distance between this remote plasma source and the substrate stage, located in the center of the reactor, is approximately 30 cm. O_2 is introduced into the reactor through the plasma source which is operated at 100 W input power. The pressure inside the reactor varied from a base pressure in the order of 10^{-5} mbar during the pump-down step in the ALD cycle, to 0.08 mbar during the O_2 pulse. The temperature of the reactor walls (T_w) was kept at 80 °C for all depositions except those at 30°C, for which T_w was 30 °C as well. The substrate temperature (T_{sub}) was varied between 30 and 300 °C. The $(MeCp)PtMe_3$ precursor (98 % purity, Sigma-Aldrich) is injected into the reactor through a flange at the side of the reactor. The experimental conditions used for studying the process window, nucleation, and conformality are summarized in Table 6.1.

Process window study: The process window of the PtO_x ALD process has been determined in two sets of experiments, for which the experimental conditions are shown in the first two rows of Table 6.1. In the first set, T_{sub} (100-300 °C) and t_{plasma} (0.5-5 s) were varied, while p_{prec} was kept constant. The temperature of the precursor bubbler (T_{prec}) was set to 30 °C and Ar was used as carrier gas. The precursor exposure time (t_{prec}) was 5 s. These settings were chosen to reduce precursor consumption. Due to the carrier gas the partial pressure of the precursor could not be accurately determined. For the second set of experiments, T_{sub} was kept constant at 300 °C while t_{plasma} (2-5 s) and p_{prec} were varied. To vary p_{prec}, T_{prec} was set to 50 and 70 °C, and the precursor was vapor-drawn into the reactor for 3 s, followed by a 3 s wait. During this entire precursor step, the valve between the reactor and the turbomolecular pump was closed. The partial pressure of the precursor for the vapor-drawn injection (i.e. p_{prec}) was determined in the absence of a carrier gas or reaction products. This yielded a p_{prec} of 0.005 mbar for T_{prec} = 50 °C and 0.012 mbar for T_{prec} = 70 °C during the (MeCp)$PtMe_3$ pulse. For both experiment sets, Si(100) substrates covered approximately 450 nm thermally grown SiO_2 were used. Layer thicknesses were determined by in-situ spectroscopic ellipsometry (SE) using a J. A. Woollam, Inc. M2000U ellipsometer (20). For these SE experiments, all deposited films were at least 7 nm thick, to ensure a good fit from SE modeling (7). Pt and PtO_x have very distinct dielectric functions and therefore, SE could be used to determine the composition of the deposited material. The imaginary part of the dielectric function ε_2 of Pt can be described by a Drude-Lorentz parameterization whereas ε_2 of PtO_x can be described by a Tauc-Lorentz parameterization (7). In addition to the SE analysis, the film composition was confirmed by determining the four-point probe (4PP) resistivity of the deposited films: thin films of metallic Pt grown by ALD have a resistivity in the order of 15 µΩ.cm, whereas the resistivity of PtO_x was found to be larger than 10^8 µΩ.cm. Furthermore, the atomic composition and mass density of the deposited PtO_x at 30 and 100 °C were determined for selected samples by Rutherford backscattering spectrometry (RBS). In these measurements, carried out by AccTec B.V., a beam of 2 MeV $^4He^+$ ions is used under grazing incidence conditions.

Table 6.1. *Overview of the conditions for the experiments carried out in this work. Spectroscopic ellipsometry (SE), Rutherford backscattering (RBS), four-point probe (4PP), and X-ray photoelectron spectroscopy (XPS) analysis were carried out on films deposited on SiO_2 substrates. XRR was carried out on films deposited on Si, Al_2O_3, and TiO_2. LEIS and TEM analysis was carried out on films prepared on TiO_2 covered Si.*

Experiment	T_{sub} (°C)	t_{plasma} (s)	(s)	p_{prec} (mbar)	T_{prec} (°C)	Precursor dosing	Analysis techniques
Material study (T_{sub} and t_{plasma})	30, 100 -300	<5	5	~10^{-3}	30	Ar carrier gas	SE, RBS, 4PP
Material study (p_{prec})	300	<5	3 (dosing) + 3 (wait)	0.005, 0.012	50, 70	Vapor drawn	SE, 4PP
Nucleation study	100	5	3	0.012	70	Vapor drawn	SE, XRR, LEIS, TEM, XPS
Conformality study	100	20	10	~10^{-3}	30	Ar carrier gas	SEM

Nucleation study: Another series of depositions was carried out to study the nucleation and growth of PtO_x by ALD. These depositions were carried out at T_{sub} = 100 °C and t_{plasma} = 5 s. In this case, T_{prec} was kept at 70 °C and the precursor was vapor-drawn into the reactor without any carrier gas (t_{prec} = 3 s). Individual samples were deposited in a series of 2, 4,..., 20, 30,..., 90, 150, 400, and 1000 cycles on 4 different substrates: Si(100) substrates with ~1 nm native oxide; Si(100) substrates with 450 nm thermal SiO_2; Si(100) substrates with 50 nm ALD prepared Al_2O_3; and Si(100) substrates with 30 nm ALD prepared TiO_2. The substrates received a 10 s O_2 plasma pre-treatment prior to Pt or PtO_x ALD to remove organic contaminants possibly present on the surface. The samples were analyzed using spectroscopic ellipsometry (SE), X-ray photoelectron spectroscopy (XPS), X-ray reflectivity (XRR), and low-energy ion scattering (LEIS). The XPS experiments in which chemical composition was determined were performed on a Thermo Scientific K-Alpha KA1066 spectrometer with monochromatic Al K_α X-ray sources ($h\nu$ = 1486.6 eV). Photoelectrons were collected at a take-off angle of 60°, as measured from the surface normal. A 400 μm diameter X-ray spot was used in the analyses, and possible sample charging was avoided by a flood gun. The XRR measurements were performed on an X'Pert Pro MRD diffractometer from PANalytical. The XRR data was modeled using *X'Pert Reflectivity* software where the thickness, density, and roughness were determined directly from the fitted curve. Low-energy ion scattering (LEIS) was performed at IONTOF on an IONTOF Qtac^{100} system for high-sensitivity LEIS, using LEIS surface spectrometry with 3 keV $^4He^+$ ions. Prior to the LEIS measurements the surface was treated for 20 minutes with O-atoms from a plasma to remove surface hydrocarbon contaminations. To study the nucleation behavior of PtO_x on TiO_2, several 30 nm thick Si_3N_4 membranes were first covered with approximately 3 nm TiO_2 by means of ALD, after which 10, 30, 40, 90, and 150 cycles of PtO_x ALD were applied. Transmission electron studies studies were performed using an FEI Tecnai F30ST operated at 300 kV in high angle annular dark field (HAADF) - scanning TEM (STEM) mode.

Film conformality: The conformality of the PtO_x ALD process was examined by depositing PtO_x layers in trenches that were dry-etched in Si. These trenches had an aspect-ratio of 9, i.e. a width of 3 µm and a depth of 27 µm, and were covered with 100 nm of thermally grown SiO_2. The thickness of the deposited PtO_x was determined by imaging cleaved samples using cross-sectional scanning electron microscopy (SEM) on a JEOL 7500 FA system. For the deposition in trenches, t_{prec} was 10 s, and t_{plasma} was 20 s.

Results

Process window

Figure 6.1 shows the results obtained for the process window of the PtO_x ALD process, i.e. the composition in terms of Pt or PtO_x of the deposited films as a function of T_{sub} and t_{plasma}, and p_{prec}. The first panel in Figure 6.1 shows the composition of the films obtained for conditions where the precursor was carried into the reactor by Ar gas. The second and third panels show the composition at 300 °C for conditions with vapor-drawn precursor injection with p_{prec} = 0.005 mbar and p_{prec} = 0.012 mbar. The composition was determined using spectroscopic ellipsometry (SE) in combination with four-point probe (4PP) resistivity analysis: the imaginary part of the dielectric function ε_2 of Pt films could be fitted well using a Drude-Lorentz model and the films had a resistivity of approximately 15 µΩ.cm; ε_2 of PtO_x films could be fitted well by a Tauc-Lorentz model and had a resistivity greater than 10^8 µΩ.cm. Figure 6.2 shows ε_2 for Pt and PtO_x for comparison.

Figure 6.1 shows that for carrier gas injection at 100 °C, PtO_x is deposited independent of t_{plasma} in the range of 0.5-5 s. Between 150 and 250 °C an increase is observed in the O_2 plasma exposure time that is required to oxidize the films, from 1 s (150-200 °C) to 5 s (250 °C). Figure 6.1 furthermore shows that at 300 °C, only metallic Pt was deposited for t_{plasma} up to 5s when using carrier gas injection. We therefore conclude that at higher temperatures the films have a tendency to be metallic Pt instead of PtO_x. This is consistent with the findings of Knoops *et al.* (7). It is also consistent with the findings of Hämäläinen *et al.* who observed an O/Pt ratio between 1.47 and 1.67 at 130 °C and a ratio of 0.09 at 200 °C (6). A similar transition with T_{sub} was reported by Kim *et al.* who studied the dependence of the transition from Ir to IrO_2 on deposition temperature and oxygen pressure (21). The right panels in Figure 6.1, containing the data for vapor-drawn injection, reveal the influence of p_{prec} on the composition of the deposited material at 300 °C. For the relatively higher p_{prec} of 0.012 mbar, Pt is deposited for t_{plasma} from 2-5 s, which is similar to the case for carrier gas injection. If p_{prec} is lowered to 0.005 mbar, however, PtO_x is deposited at 300 °C instead of Pt. Clearly, the composition of the deposited material also depends on p_{prec}.

To determine whether the growth per cycle (GPC) of PtO_x depends on T_{sub}, t_{plasma}, and/or p_{prec}, the GPC of the depositions shown in Figure 6.1 was determined by SE. The GPC varied between 0.047 and 0.057 nm per cycle, but no clear dependence on T_{sub}, t_{plasma}, or p_{prec} could be found. These values are similar to those reported by Knoops *et al.* for PtO_x (0.0 47nm per cycle) and Pt (0.045 nm per cycle) (7). The similarity of the GPC of PtO_x to that of Pt is remarkable, given that the density of Pt atoms in metallic Pt is approximately twice the Pt atom density in PtO_x. This implies that during ALD of Pt, twice as much Pt is deposited during the precursor cycle compared to ALD of PtO_x.

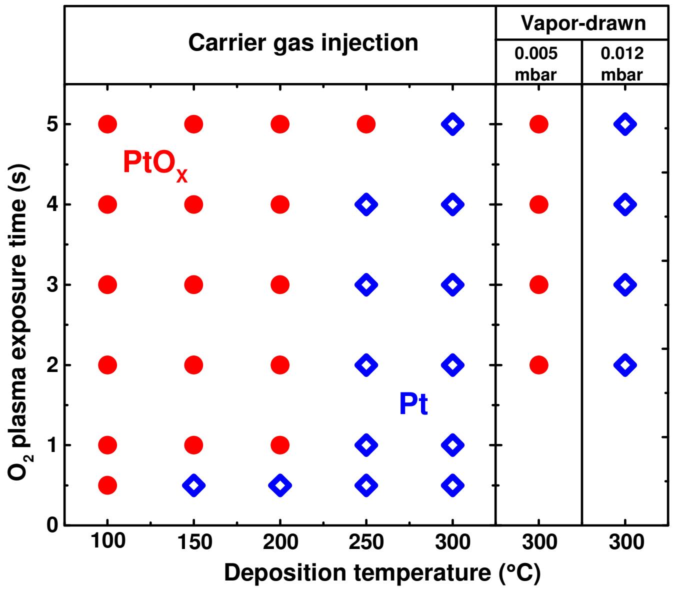

Figure 6.1. *The composition of the deposited ALD films (Pt versus PtO$_x$) for various combinations of O$_2$ plasma exposure time, substrate temperature, and precursor pressure. Closed circles indicate PtO$_x$, open diamonds represent Pt. Film composition was determined using SE and 4PP analysis, and the minimum film thickness was 7 nm. For the first panel (labeled "carrier gas injection") the precursor was carried into the reactor using Ar gas. For carrier gas injection, PtO$_x$ is deposited at 100 °C and Pt is deposited at 300 °C independently of O$_2$ plasma exposure time. Between 150 and 250 °C an increasingly longer O$_2$ plasma exposure time is required to deposit PtO$_x$ instead of Pt. For the second and third panels (labeled "vapor-drawn") the precursor was vapor-drawn into the reactor, resulting in a precursor pressure of 0.005 mbar and 0.012 mbar, respectively. At 300 °C, Pt is deposited for a precursor pressure of 0.005 mbar, while PtO$_x$ is deposited for 0.012 mbar.*

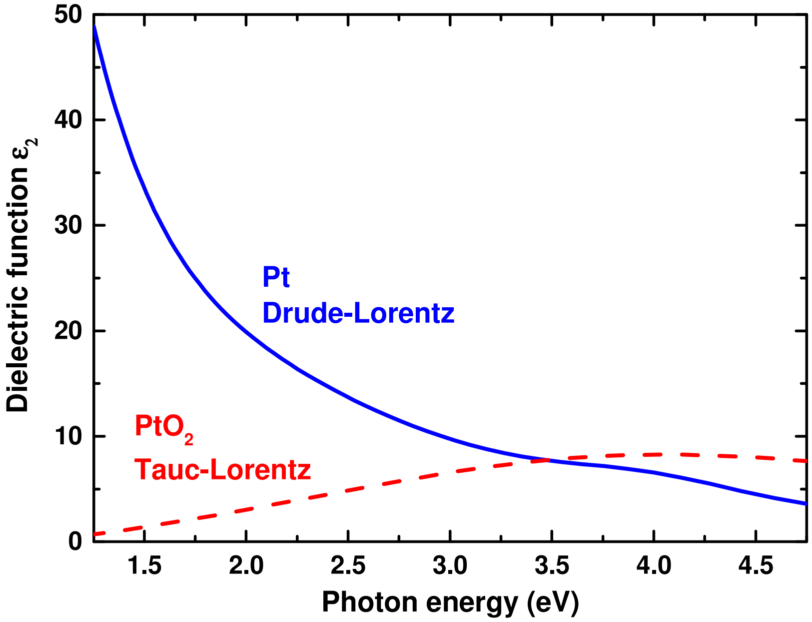

Figure 6.2. *The imaginary part of the dielectric function (ε_2) for Pt and PtO_x as derived from SE measurements. For Pt and PtO_x Drude-Lorentz and Tauc-Lorentz parameterizations were assumed respectively.*

Material properties

On the basis of the results in Figure 6.1, t_{plasma} = 5 s and T_{sub} = 100 °C (T_{prec} = 30°C, using Ar as a carrier gas, and 5 s exposure time) were used as standard settings for the deposition of PtO_x films to determine the material properties. These properties are given in the second row of Table 6.2. RBS measurements revealed a density of 9.5 ± 0.5 g/cm^3, which agrees nicely with the value reported by Knoops *et al.* (8.9 ± 0.5 g/cm^3). RBS measurements also revealed that at 100 °C the O/Pt ratio is 2.5 ± 0.2, which is somewhat higher than the ratio of 2.2 that was previously reported by Knoops *et al*. (7) for T_{sub} = 300 °C. The ratio of 2.5 suggests a mixture of stable oxides of platinum. For example, the ratio of 2.5 has been reported for electrodeposited platinum oxide, where it was assumed that the ratio could be ascribed to a combination of PtO_2 with (possibly oxygen-deficient) PtO_3 (22)-(23). For both PtO_2 and PtO_3, the oxidation state of Pt is 4. Another explanation for the high O/Pt ratio could be the formation of $PtO_2.H_2O$ (Pt in oxidation state 4).(24) The incorporation of H_2O in the matrix can be related to the H_2O formed as a reaction product from the combustion of the precursor ligands, which is well-known for Pt ALD (9,25). In the work of Hämäläinen *et al.* an O/Pt ratio between 1.09 and 1.66 has been reported. This is significantly lower than the value of 2.5 found in this work, and is most likely due to the fact that an O_2 plasma is a stronger oxidizing reactant than ozone (26). We note however, that Hämäläinen *et al.* also used $Pt(acac)_2$ as a precursor instead of $(MeCp)PtMe_3$.

Table 6.2. *The material properties of PtO_x films deposited by plasma-assisted ALD using $(MeCp)PtMe_3$ and O_2 plasma. The substrate was SiO_2 and the substrate temperature was 30 and 100 °C. The growth per cycle (GPC, unit: nm/cycle) was determined using SE; the atomic composition, the GPC (unit: $at/cm^2\cdot cycle$) and O/Pt ratio were determined using RBS. The mass density was determined by combining the RBS data with the film thickness data determined by SE. For RBS, typical experimental relative errors in the atomic composition and the GPC (unit: $at/cm^2\cdot cycle$) are 3 %.*

Temperature (°C)	GPC (nm/cycle)	GPC ($at/cm^2\cdot cycle$)	Density (g/cm^3)	Atomic composition (%)			O/Pt ratio
				Pt	O	C	
30	0.059 ± 0.004	$1.25\cdot10^{14}$	8.3 ± 0.5	26	72	2	2.7 ± 0.2
100	0.052 ± 0.004	$3.06\cdot10^{14}$	9.5 ± 0.5	29	71	-	2.5 ± 0.2

ALD at room temperature

In an attempt to extend the lower limit of the temperature window for plasma-assisted ALD of PtO_x using $(MeCp)PtMe_3$ and O_2 plasma to room temperature (RT), T_{sub} and T_{wall} were set to 30 °C. Under these conditions, PtO_x was obtained with saturation of the GPC at 0.059 nm/cycle occurring at t_{prec} = 3 s and t_{plasma} = 4 s. The precursor exposure (T_{prec} = 30 °C, Ar carrier gas) and O_2 plasma exposure times were 5 s. The O/Pt ratio determined by RBS was 2.7 ± 0.2, and the PtO_x had a density of 8.3 ± 0.5 g/cm^3, as can be seen in the first row of Table 6.2. This O/Pt ratio at 30 °C is higher than at 100 °C, which is consistent with the higher O/Pt ratios at lower temperatures reported in the previous section. The fact that the density of the PtO_x deposited at 30 °C is somewhat lower compared to that at 100 °C, can be attributed to the higher O/Pt ratio. It is likely that this lower density is also the cause of the higher GPC at RT.

PtO_x nucleation

The nucleation of PtO_x at 100 °C has been studied in some detail. Figure 6.3 shows the thickness of the PtO_x films grown on SiO_2, as measured by in-situ SE as a function of cycle number. The inset of the figure shows the first 70 cycles. As can be seen, the curve does not take off linearly at the origin. The offset of ~20 cycles can be attributed to a nucleation delay that is also known to occur during the initial growth of metallic Pt. The fit shows a linear increase of thickness as a function of cycle number after approximately 30-50 cycles, which indicates that *layer-by-layer* growth may occur after the film has reached a thickness of approximately 2 nm. The GPC was 0.052 ± 0.004 nm, which agrees with the results from Knoops *et al.* (0.060 ± 0.004 nm at 100 °C).

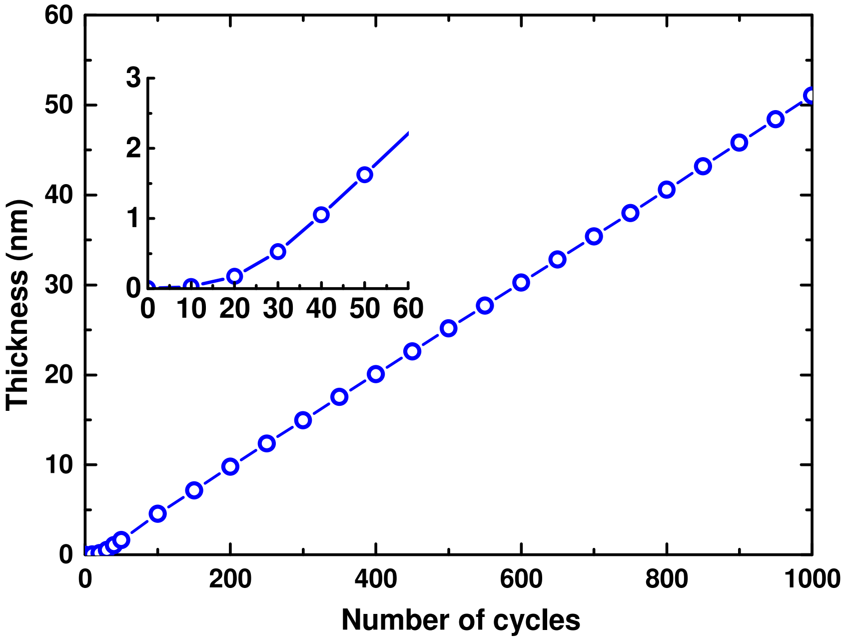

Figure 6.3. *The thickness of the PtO_x films deposited on SiO_2 as a function of the number of cycles, as measured with SE. The inset shows the initial growth during the first 70 cycles.*

Figure 6.4 shows the thickness of PtO_x films grown on Si, TiO_2, and Al_2O_3 surfaces as determined by XRR. Similar to the results shown in Figure 6.3, a nucleation delay of approximately 10-20 cycles can be observed for all substrates. Nucleation appears to proceed somewhat faster on TiO_2, where a thickness of 2.5 nm is reached after 50 cycles, compared to 60 and 70 cycles for Si and Al_2O_3, respectively. After approximately 50 cycles, growth appears to be linear and the GPC was determined to be 0.060, 0.057, and 0.056 ± 0.006 nm/cycle for, respectively, Si, TiO_2, and Al_2O_3.

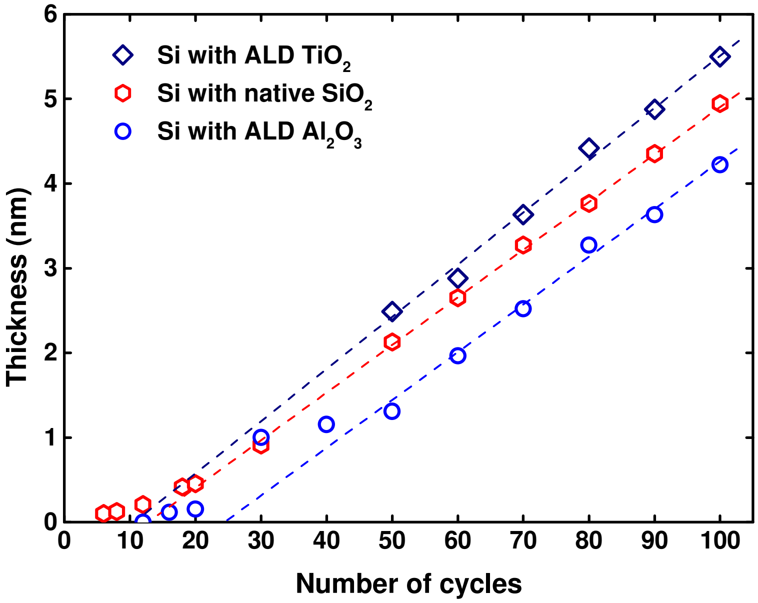

Figure 6.4. *The thickness of the PtO_x films deposited on an ALD TiO_2 film, Si with native oxide, and an ALD Al_2O_3 film as a function of the number of cycles as determined from XRR analysis. Lines serve as a guide to the eye.*

XPS was used to determine the stoichiometry of the PtO_x and therefore films deposited with different number of cycles were analyzed (27,28). Since Pt is in oxidation state 4 in PtO_2, PtO_3, and $PtO_2.H_2O$, it is challenging to distinguish between these phases using XPS and therefore we only distinguish Pt in oxidation state 4 (labeled PtO_2) and Pt in oxidation state 2 (labeled PtO) for simplicity in this analysis. In Figure 6.5(a), the XPS spectrum of the Pt 4f doublet is shown for a PtO_x film deposited in 90 cycles on SiO_2. The two peaks of the PtO 4f7/2 and 4f5/2 orbitals and those of the PtO_2 4f7/2 and 4f5/2 orbitals can be clearly distinguished. As can be seen, the constructed envelope function fits the measured data very well, yielding a fraction of 0.16 for PtO and 0.84 for PtO_2.

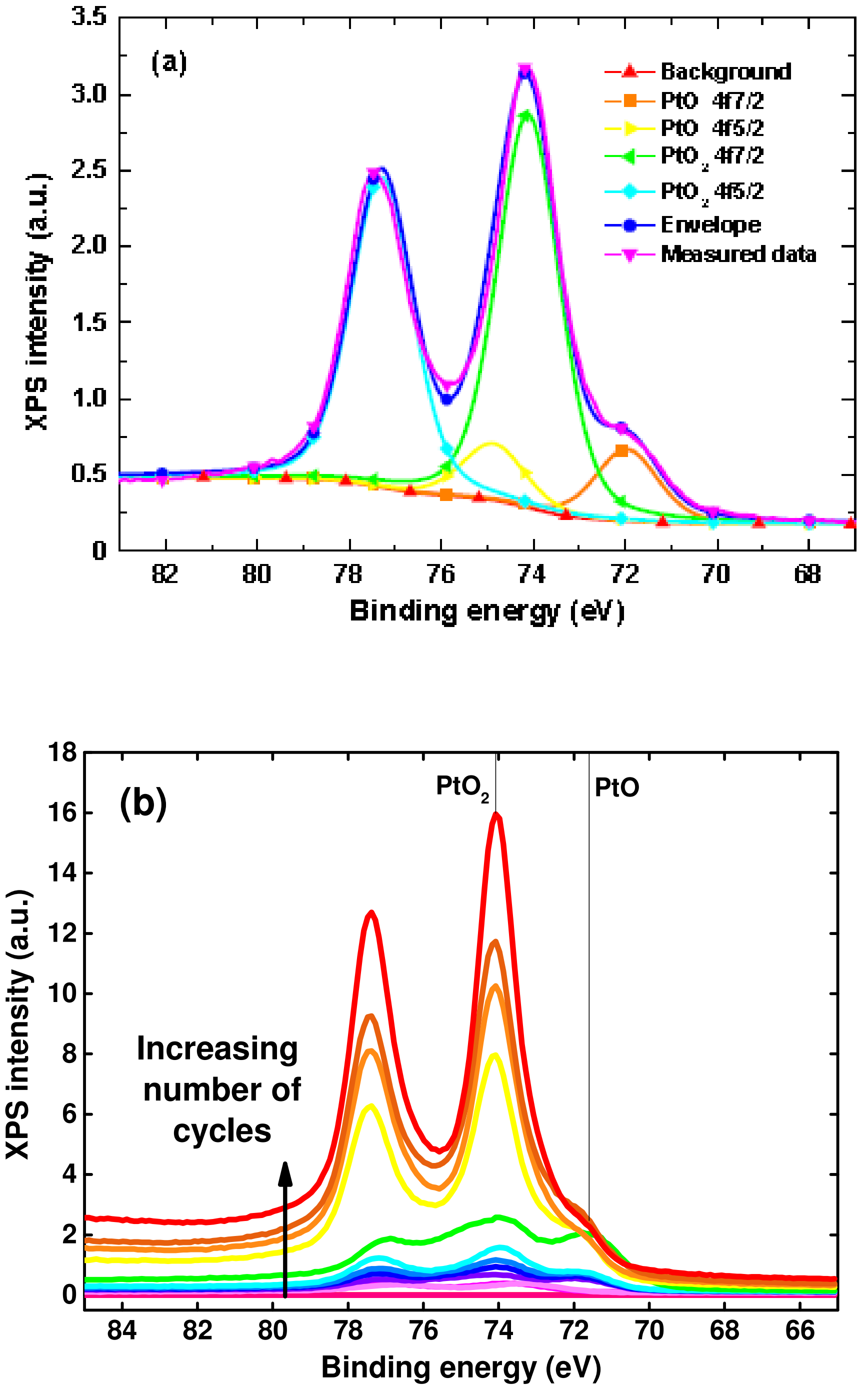
(a)
3.5
3.0
2.5
2.0
1.5
1.0
0.5
0
XPS intensity (a.u.)
82
80
78
76
74
72
70
68
Binding energy (eV)
Background
PtO 4f7/2
PtO 4f5/2
PtO_2 4f7/2
PtO_2 4f5/2
Envelope
Measured data
(b)
18
16
14
12
10
8
6
4
2
0
XPS intensity (a.u.)
PtO_2
PtO
Increasing number of cycles
84
82
80
78
76
74
72
70
68
66
Binding energy (eV)

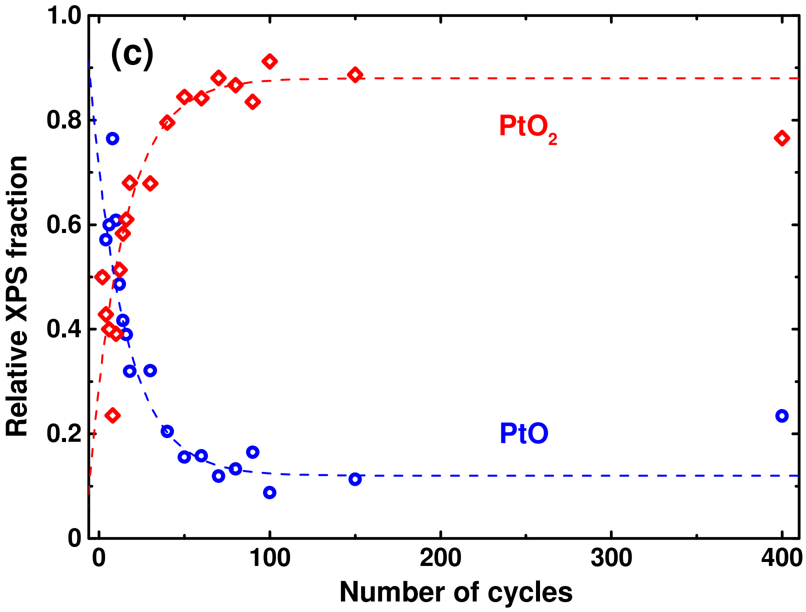

Figure 6.5(a). *The measured and fitted XPS intensity after 90 cycles ALD of PtO_x on a SiO_2 substrate. The doublets for PtO and PtO_2 can clearly be distinguished.* ***(b).*** *The measured XPS intensity for 2, 4, 6, 8, 10, 12, 14, 16, 18, 20, 30, 40, 50, 60, 70, 80 , 90, 150, and 400 cycles of PtO_x ALD on SiO_2 substrates. The 4f7/2 peaks for PtO_2 and PtO are labeled for clarity.* ***(c).*** *The relative XPS fractions of PtO_2 and PtO as a function of number of cycles on SiO_2 substrates. The dotted lines serve as guides to the eye. Each data point represents a separate sample.*

Figure 6.5(b) shows the Pt4f doublet for PtO_x films deposited on SiO_2 with a number of cycles ranging from 2 to 400. From the data, which clearly show that the ratio between PtO and PtO_2 changes as the number of cycles increases, the relative XPS fractions of PtO and PtO_2 are extracted and plotted as a function of number of cycles in Fig. 5(c). As can be seen from this figure, the fraction of PtO during the initial 10 cycles ranges somewhere between 0.6 and 0.8. Between 2 and 100 cycles the PtO fraction decreases rapidly until it reaches the relatively constant value of ~0.15. Given the limited escape depth of XPS of several nanometers, the decrease of the PtO fraction points to the presence of a PtO overlayer with a constant thickness located on top of the film while the bulk consists of PtO_2. Angle-resolved XPS (AR-XPS) data (not shown here) confirmed that the PtO is indeed located mainly in the top part of the film. The PtO overlayer is most likely caused by the reduction of the top layers of the deposited PtO_x films by reducing vapors such as water (29). Despite this reduction, the XPS data do indicate that platinum oxide is deposited during the first cycles and not only after, e.g., a closed layer has been formed. This implies that the initial nanoparticles that are formed during nucleation, as addressed below, also consist of PtO_x.

PtO_x island formation and layer closure

To study the initial growth regime and confirm the formation of PtO_x islands before film closure, TEM images were made of TiO_2-covered Si_3N_4 membranes after 10, 30, 40, 90, and 150 cycles of PtO_x ALD, as can be seen in Figure 6.6. Figure 6.6 (a) shows the formation of PtO_x islands at the surface after 10 ALD cycles. These islands, basically nanoparticles, have an average size of approximately 1 nm^2 and a particle density of ~$5 \cdot 10^{12}$ cm^{-2}. After 30 cycles, in Figure 6.6 (b), the islands can be seen to have increased in size and to start coalescing. Figure 6.6 (c) shows that after 40 cycles the surface is almost completely covered by a film, with the exception of perhaps a few small dark areas which comprise less than 5 % of the surface. Figures 6 (d) and (e) indicate that after 90 cycles a completely closed layer is formed, with a non-negligible surface roughness.

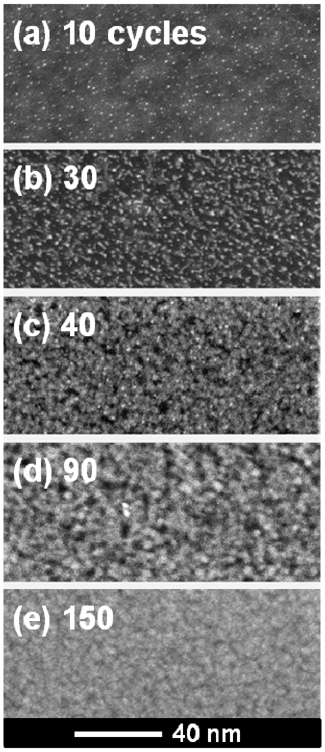

Figure 6.6. *Planar view high angle annular dark field STEM images after (a) 10, (b) 30, (c) 40, (d) 90, and (e) 150 cycles of plasma-assisted ALD of* PtO_x *on a* TiO_2 *film deposited on a* Si_3N_4 *membrane.*

To confirm that layer closure occurs after ~40 cycles for ALD of PtO_x, low energy ion scattering spectroscopy (LEIS) measurements were performed on PtO_x deposited on TiO_2 samples. Figure 6.7 shows the LEIS spectrum of bulk TiO_2 alongside the spectra of the TiO_2 (30 nm) substrates that have undergone, respectively 0, 10, 30, 40 and 90 cycles of PtO_x ALD. Peaks in the LEIS spectrum are caused by scattering of primary ions and, therefore, indicate species present at the surface. Any raised background signal (i.e. a shoulder) on the lower energy side of a peak is caused by secondary re-ionized ions and indicates that a species is present in the subsurface layers. Considering the spectrum for bulk TiO_2 and starting from the high energy tail, the Ti peak at 2100 eV can first be distinguished, indicating the presence of Ti (from TiO_2) at the surface. The raised background signal at lower energies beyond the Ti peak originates from Ti in the subsurface layers. The peak caused by surface oxygen was detected at 1100 eV, followed by a raised background signal from the subsurface oxygen. The slight shift of the oxygen peak with respect to those of the other measurements can be ascribed to a difference in sample charging during the measurement. Compared to the bulk spectrum, the spectrum for the reference TiO_2 substrate (0 cycles) shows a lower Ti peak at 2100 eV, while a Si peak at 1680 eV appears. This indicates the presence of some surface contamination, which is believed to be Si from pump oil from the reactor. The fact that the trend of the background signal is not altered by the Si peak indicates that Si is only present at the surface.

After 10 PtO_x ALD cycles the peak for this Si contamination is still present, while the Ti peak has disappeared. Furthermore, a Pt peak at 2700 eV has become visible. This indicates that after 10 cycles most of the TiO_2 has been covered with PtO_x. The increase of the signal from 2100 eV downwards is caused by the presence of TiO_2 in the subsurface layers. In the spectrum after 30 cycles, the silicon peak has completely disappeared. The Pt peak has almost reached its maximum size, which suggests that most of the surface is now covered with PtO_x. Analysis of the peak distribution based on an energy loss of 160 eV per nm for 3 keV He^+ ions in PtO_x was performed to determine PtO_x thickness. This revealed a maximum PtO_x thickness of 2 nm, not accounting for the presence of particles. After 40 cycles, a clear shoulder besides the Pt peak can be seen. This shoulder indicates that the PtO_x layer has grown beyond the surface layer. Analysis of the peak distribution revealed a maximum PtO_x layer thickness of 3.5 nm. Finally, the spectrum for 90 cycles shows the Pt peak around 2700 eV, accompanied by a plateau from approximately 2600-2100 eV, after which the signal steadily declines down to approximately 1750 eV. This indicates a PtO_x thickness between 3 and 6 nm. The LEIS results therefore corroborate the TEM observations of layer closure after ~40 cycles, corresponding to a film thickness of approximately 2 nm.

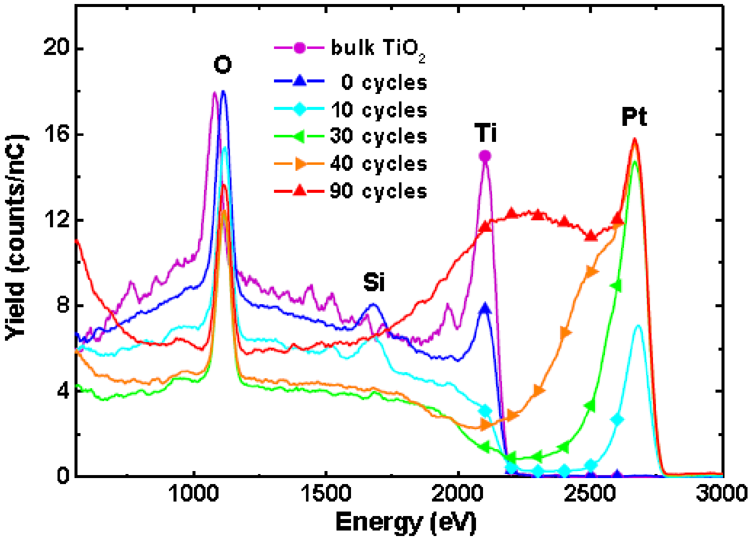

Figure 6.7. *LEIS spectra of bulk TiO_2, and TiO_2 films exposed to 0, 10, 30, 40, and 90 cycles of plasma-assisted ALD of PtO_x (data markers are only indicated between 2000 and 2500 eV for clarity). The oxygen peak at 1100 eV of the bulk TiO_2 is shifted slightly compared to that of the other samples due to a difference in sample charging during the measurement. The Ti peak at 2100 eV for 0 cycles PtO_x is lower due to some Si contamination on the surface, observed at 1700 eV. After 10 cycles of ALD of PtO_x, the Ti peak has almost disappeared and the Pt peak at 2650 eV has appeared. After 30 cycles, both the Si and Ti peak have almost completely disappeared, and the Pt peak has reached almost its full height. After 40 cycles the entire surface is covered with PtO_x.*

To further study growth during the initial 100 cycles, XRR data were used to calculate the roughness and density of PtO_x deposited on Si and Al_2O_3 as a function of the number of cycles. Based on the data (not shown here), 3 regimes could be distinguished. During the first 20 cycles the roughness increased from 0 to ~1 nm, while the density was relatively low at ~7.5 g/cm^3. Both an increasing roughness and a low density are consistent with the formation of nanoparticles. Between 20 and 40 cycles the roughness decreased to ~0.5 nm while the density increased to 10 g/cm^3, which indicates the growth and coalescence of the islands. After 40 cycles both the roughness (0.5 nm) and density (10 g/cm^3) remained constant, in good agreement with values reported earlier by our group (7). This is further evidence of the formation of a closed layer with bulk density values and the start of *layer-by-layer* growth after approximately 40 cycles, which corresponds to a layer thickness of approximately 2 nm. In comparison, for plasma-assisted ALD of metallic Pt on Al_2O_3, linear growth has been reported to start after a layer thickness of 2-3 nm, although bulk density values were reached only after a layer of 4-5 nm in thickness was deposited (11).

Conformality in high aspect-ratio trenches

In order to study the conformality of the films, PtO_x with a nominal thickness of ~88 nm was deposited in trenches of aspect ratio of 9 (T_{sub} = 100°C, t_{prec} = 10 s, t_{plasma} = 20 s). A cross-sectional SEM image of a trench with PtO_x is given in Figure 6.8 (a). Figures 8 (b-d) are higher magnification images of the top, center, and bottom part of the trench, respectively. On top of the Si, two separate layers of approximately 100 nm can be distinguished. The bottom layer is a 100 nm thick film of SiO_2 that was thermally grown after etching the trench, while the top layer is the PtO_x deposited by ALD. From the higher magnification images in Figure 6.8 (b-d) as well as some other similar images at other locations in the trench, the thickness of the PtO_x ALD layer in the trench was determined. The results are shown in Figure 6.9, where the thickness of the PtO_x layer is plotted as a function of trench depth. The thickness of the deposited PtO_x film is ~88 nm at the entrance of the trench, and gradually drops to ~73 nm when going down into the trench. The normalized average thickness of the PtO_x film in the trench was (90 ± 10) % of the thickness on top of the wafer, revealing a conformality of ~90% for PtO_x in trenches with an aspect ratio of 9.

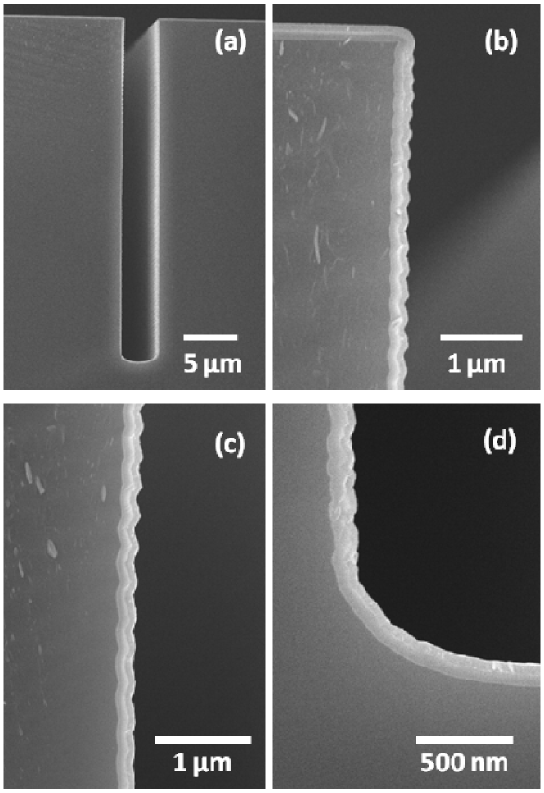

Figure 6.8. *SEM images of* PtO_x *deposited in a trench etched in Si with aspect ratio of 9. The trench surface is covered with a 100 nm thermally grown* SiO_2 *film. The images show side views of* ***(a)*** *the full trench,* ***(b)*** *the top part of the trench,* ***(c)*** *the middle part of the trench, and* ***(d)*** *the bottom part of the trench.*

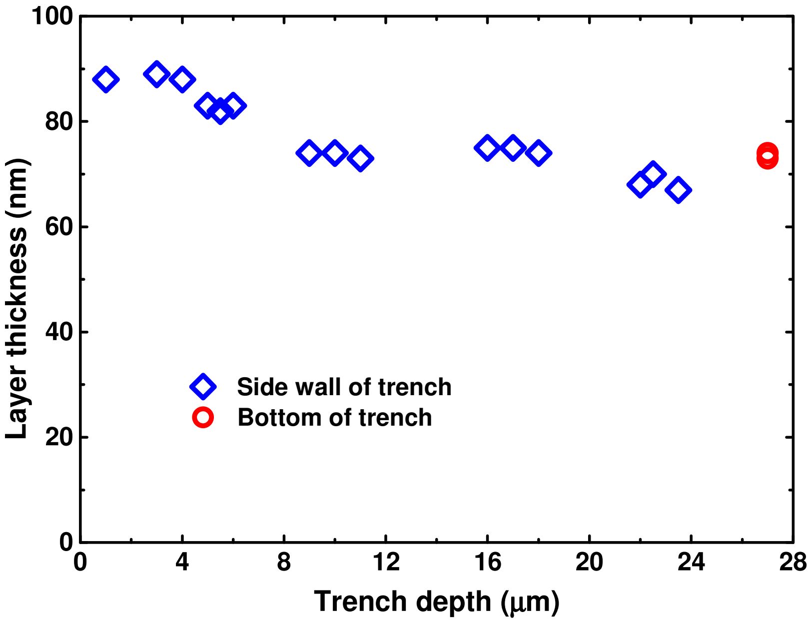

Figure 6.9. *Thickness profile of the PtO_x film inside the trench with an aspect ratio of 9 as deduced from the SEM images in Figure 6.8. The error in the PtO_x thickness is 4 nm, the error in the trench depth is 1 µm.*

Discussion

The results presented in this work, in particular in Figure 6.1, show that the composition of the deposited material for plasma-assisted ALD using (MeCp)$PtMe_3$ and O_2 plasma depends on t_{plasma}, T_{sub}, and p_{prec}. For increasing T_{sub}, longer t_{plasma} and/or lower p_{prec} are required to obtain PtO_x. In this section, the manner in which these three process parameters influence the reaction mechanism leading to either metallic Pt or PtO_x will be examined more closely. We note here, that although t_{plasma} and p_{prec} were varied in our experiments, it is the O-radical *dose* and the precursor particle *dose* (i.e. the time integral of the particle flux) that actually govern the surface reactions. Since the O-radical dose depends directly on t_{plasma}, and the precursor particle dose directly on p_{prec} however, we will continue to use these terms for clarity and simplicity.

We will first consider reports on the oxidation of Pt in the literature. Although the reaction mechanism of PtO_x ALD has not been examined in great detail before, many surface science studies have been performed on the oxidation of Pt in view of the relevance of this material in catalysis. These studies mostly deal with the oxidation of single-crystalline Pt(111), often under ultrahigh vacuum (UHV) conditions. Based on these surface science studies, the following general mechanisms for Pt oxidation can be proposed.

The leading parameter in the oxidation of Pt is the oxygen surface coverage, typically expressed in monolayers (ML), where 1 ML on Pt(111) corresponds to a surface atom density of $1.51 \cdot 10^{15}$ cm^{-2}. The oxygen surface coverage that can be reached when exposing Pt(111) to oxidizing species depends on experimental conditions such as the nature of the oxidizing species (O_2, NO_2, O_3, atomic O, etc.), exposure, and temperature. When O_2 gas is used in a temperature and pressure range that is typical for ALD, an oxygen coverage of 0.25 ML is reached for Pt(111).(30) Higher surface coverages have been reported for more reactive oxidizing species: 0.75 for NO_2,(31) 2.4 for O_3,(32) and 2.9 for gas-phase atomic O.(26) These coverages do not depend greatly on temperature for temperatures in the range typically used for ALD (26,30). The oxidation of Pt(111), and similarly of Pt(100) (33), can generally be classified to occur in two stages: the development of a chemisorbed oxygen layer at low coverage, followed by the growth of bulk-like PtO_x patches once the oxygen coverage exceeds approximately 0.75 ML. In order to form the oxide however, kinetic barriers resulting from restructuring of the oxidizing surface, must be overcome. The strongly repulsive interaction between the oxygen atoms within the high-coverage oxygen domains may act to overcome these kinetic barriers. Once the oxide is formed, these kinetic barriers stabilize the oxide against decomposition.(34) The standard enthalpies of formation for bulk PtO and PtO_2 are -71 kJ/mol and -134 +/- 42 kJ/mol, respectively, indicating bulk PtO_2 has a higher stability than PtO (27).

The oxidation of Pt is reversible, and PtO_x can be reverted to metallic Pt through thermal decomposition. The thermal decomposition of PtO_2 in UHV is reported by Abe *et al.* to occur between 300 °C and 350 °C, while decomposition in air occurs at 550 °C (28). Other sources report thermal decomposition at 400 °C in UHV and 650 °C in ambient pressures (35,36). PtO_x can also be reduced to metallic Pt by means of reducing reactants such as H_2 or NO (35,36). Bernardi *et al.* show that the reduction process depends strongly on temperature and partial pressure of the reducing reactant, where the reduction of PtO_x occurs more readily for higher temperatures and/or higher reducing reactant pressures (37,38). The presence of a reducing reactant can also influence PtO_x formation. Getman *et al.* show that the conditions that lead to PtO_x formation in the presence of NO are shifted towards higher oxygen pressure and lower temperature (30).

We will now discuss the formation of platinum oxide during ALD, starting with the role of the oxidizing reactant. Three oxidizing reactants have been used for ALD of Pt and PtO_x. These are, in increasing order of reactivity: O_2 (7), O_3 (6), and O_2 plasma (7). On Pt(111) these oxidizing species can reach oxygen surface coverages of 0.25, 2.3, and 2.7, respectively. This could explain that Pt is obtained for O2 whereas PtO_x films with O/Pt ratios of ~1.6 and 2.7 are obtained for O_3 and O_2 plasma, respectively. Clearly, the strength of the oxidizing reactant determines the oxidation state that can be reached, presumably by reaching higher oxygen surface coverages. The precise oxygen surface coverage that can be reached using O_2 plasma, appears to depend directly on t_{plasma}. After all, between 150 and 250 °C PtO_x is only deposited for sufficiently long O_2 plasma exposure times, as shown in Figure 6.1.

Next, we will consider the reduction of platinum oxide during ALD, and the role of the precursor as a reducing reagent. Figure 6.1 shows that at 300 °C, PtO_x could be deposited when p_{prec} was lowered from 0.012 to 0.005 mbar. This is a clear indication that during each O_2 plasma step the surface layer of the film is oxidized. For sufficiently high precursor exposure however, the precursor can act as a reducing reagent, reducing the PtO_x that is formed during the plasma step into Pt. Reduction by the (MeCp)$PtMe_3$ precursor during initial growth of Pt by ALD has also been reported by Setthapun *et al.*, who performed a detailed study into the state of the Pt during ALD using (MeCp)$PtMe_3$ and O_2 gas (39). They observed that after an O_2 pulse at 300 °C, the Pt was converted from the precursor-bound state to the oxidized state of PtO_x. During the subsequent precursor pulse, performed at 100 °C however, most of the PtO_x was reduced into Pt. This reduction was ascribed to the organic precursor ligands, which can react with the oxygen (25).

Summarizing, the formation of PtO_x during plasma-assisted ALD appears to depend on a balance between oxygen radicals acting as an oxidizing reactant driving the process towards the deposition of PtO_x, and the precursor ligands acting as a reducing reagent driving the process towards the deposition of metallic Pt. Based on our results it can be assumed that for $100 \leq T_{sub} \leq 300$ °C, the surface layer of the deposited film is oxidized during each O_2 plasma step. If this oxidized layer is reduced by a sufficiently high precursor exposure during the subsequent precursor step, Pt is deposited. If the precursor dose is not sufficient to reduce the oxidized layer, PtO_x is deposited. The stability of the oxidized surface layer against reduction by the precursor appears to depend on t_{plasma}. Consider for example the fact that at 250 °C, PtO_x is deposited for t_{plasma} = 5 s, but Pt is deposited for t_{plasma} = 4 s. As mentioned, it is assumed that during the O_2 plasma steps of the deposition of both films, the surface layer is oxidized. During the precursor steps however, both films are also exposed to identical precursor exposures, while only the film with t_{plasma} = 4 s is reduced. Apparently, the oxide layer created by the longer plasma exposure is more stable against reduction.

Another important parameter in PtO_x formation during ALD is T_{sub}. Figure 6.1 clearly shows that for higher temperatures, a longer plasma exposure time is required to obtain PtO_x. This indicates a decrease in the ability of the deposited material to withstand reduction by the precursor for higher temperatures. Apparently, reduction occurs at higher rates for higher temperatures. Purely temperature-driven spontaneous reduction does not appear to occur for $T_{sub} \leq 300$ °C, since PtO_x can be deposited even at 300 °C. This agrees with reports in the literature where thermal decomposition of PtO_x was observed to occur above 300 °C (28,35,36). Another way in which T_{sub} may influence the formation of PtO_x is through the O/Pt ratio of the deposited material. From our results and reports in literature it can be concluded that for lower temperatures, material with a higher O/Pt ratio is obtained. At a T_{sub} of respectively 30, 100, and 300 °C, PtO_x films with an O/Pt ratio of 2.7, 2.5, and 2.2 were deposited (7). Therefore, it can be concluded that the (MeCp)$PtMe_3$ precursor and the O_2 plasma counteract each other in terms of PtO_x formation. An increase in O_2 plasma exposure will promote the formation of PtO_x, while an increase in the precursor exposure will promote the formation of Pt. The reaction mechanism behind the formation of PtO_x depends on temperature through the temperature dependence of the reduction of PtO_x by the precursor and/or through the temperature dependence of the obtained O/Pt ratio.

Conclusions

A comprehensive study of PtO_x formation by the ALD process using $(MeCp)PtMe_3$ and O_2 plasma has been presented. We demonstrated that by controlling O_2 plasma exposure time and precursor pressure, PtO_x can be deposited in a temperature window ranging from 30 to 300 °C. At higher substrate temperature, longer O_2 plasma exposure and/or lower precursor exposure is required to obtain PtO_x. Whether PtO_x or Pt is deposited, therefore appears to be governed by a temperature dependent balance between the oxidation by the O_2 plasma, and reduction by the organic ligands of the $(MeCp)PtMe_3$ molecules. The initial growth regime of the PtO_x is characterized by the formation of PtO_x nanoparticles, which form, grow, and finally coalesce. A closed layer with a density approaching the bulk density (10 g/cm^3) is formed after approximately 40 cycles, corresponding to a minimum thickness of only ~2 nm. The nucleation delay and GPC were found to be very similar on all investigated surface materials (Si, SiO_2, TiO_2, and Al_2O_3). In-depth analysis of the deposited material at 100 °C showed a GPC of 0.052 nm/cycle, an O/Pt ratio of 2.5, and a density of 9.5 g/cm^3. The bulk of the deposited films consists of PtO_2 (possibly mixed with PtO_3 and/or $PtO_2.H_2O$), while the Pt in the surface layer is more bonded as PtO, most likely through exposure to reducing gasses in the ambient. The material properties of the PtO_x deposited at 30 °C were comparable to those at 100 °C, although a slightly higher O/Pt ratio (2.7), a higher GPC (0.059 nm/cycle), and a lower density (8.3 g/cm^3) were found. Finally, the conformality of the PtO_x films deposited at 100 °C was found to be 90 % for trenches with an aspect ratio of 9.

Acknowledgments

This work is supported by NanoNextNL, a micro and nanotechnology program of the Dutch Ministry of economic affairs, agriculture and innovation (EL&I) and 130 partners. This research has also been supported financially by IMEC-NL, the Netherlands. The research of one of the authors (W.M.M. Kessels) is supported by the Netherlands Organization for Scientific Research (NWO) and the Technology Foundation STW through the VICI program on “Nanomanufacturing”. Thanks are due to K. de Peuter, K.K.

Schakenraad, and K.W.C.A. van der Straten for their experimental work, and to J.J.A. Zeebregts, M.J.F. Van de Sande, and J.J.L.M. Meulendijks for their technical support. Special thanks are due to prof. H.H. Brongersma and dr. T. Grehl (IONTOF, Germany) for the LEIS measurements and their assistance in the data analysis.

Bibliography

1. G. N. Parsons, S. M. George, and M. Knez, *Mrs Bulletin* **36**, 865 (2011).
2. C. Marichy, M. Bechelany, and N. Pinna, *Adv. Mater.* **24**, 1017 (2012).
3. F. Raimondi, G. G. Scherer, R. Kotz, and A. Wokaun, *Angewandte Chemie-International Edition* **44**, 2190 (2005).
4. D. S. Kang, S. K. Han, J. H. Kim, S. M. Yang, J. G. Kim, S. K. Hong, D. Kim, H. Kim, and J. H. Song, *Journal of Vacuum Science & Technology B* **27**, 1667 (2009).
5. V. Miikkulainen, M. Leskelä, M. Ritala, and R. L. Puurunen, *J. Appl. Phys.* **113**, 021301 (2013).
6. J. Hämäläinen, F. Munnik, M. Ritala, and M. Leskelä, *Chem. Mater.* **20**, 6840 (2008).
7. H. C. M. Knoops, A. J. M. Mackus, M. E. Donders, M. C. M. van de Sanden, P. H. L. Notten, and W. M. M. Kessels, *Electrochem. Solid-State Lett.* **12**, G34 (2009).
8. T. Aaltonen, M. Ritala, T. Sajavaara, J. Keinonen, and M. Leskelä, *Chem. Mater.* **15**, 1924 (2003).
9. I.J.M. Erkens, A. J. M. Mackus, H. C. M. Knoops, P. Smits, T.H.M. van de Ven, F. Roozeboom, and W. M. M. Kessels, *ECS Journal of Solid State Science and Technology* **1**, 255 (2012).
10. A. J. M. Mackus, D. Garcia-Alonso, H. C. M. Knoops, A. A. Bol, and W. M. M. Kessels, *Chem. Mater.* **25**, 1769 (2013).
11. L. Baker, A. Cavanagh, D. Seghete, S. George, A. Mackus, W. Kessels, Z. Liu, and F. Wagner, *J. Appl. Phys.* **109**, 084333 (2011).
12. A. J. M. Mackus, M. A. Verheijen, N. M. Leick, A. A. Bol, and W. M. M. Kessels, *Chem. Mater.* **25**, 1905 (2013).
13. S. T. Christensen, J. W. Elam, B. Lee, Z. Feng, M. J. Bedzyk, and M. C. Hersam, *Chem. Mater.* **21**, 516 (2009).
14. S. Guo and E. Wang, *Nano Today* **6**, 240 (2011).

15. M. J. Weber, A. J. Mackus, M. A. Verheijen, C. van der Marel, and W. M. M. Kessels, *Chem. Mater.* **24**, 2973 (2012).
16. Q. Liu, T. Fukaya, S. Cao, C. Guo, Z. Zhang, Y. Guo, J. Wei, and J. Tominaga, *Optics Express* **16**, 213 (2008).
17. D. Haridas, K. Sreenivas, and V. Gupta, *Sensors and Actuators B-Chemical* **133**, 270 (2008).
18. N. Sabourault, G. Mignani, A. Wagner, and C. Mioskowski, *Organic Letters* **4**, 2117 (2002).
19. H. C. M. Knoops, E. Langereis, M. C. M. van de Sanden, and W. M. M. Kessels, *J. Electrochem. Soc.* **157**, G241-G249 (2010).
20. E. Langereis, S. B. S. Heil, H. C. M. Knoops, W. Keuning, M. C. M. van de Sanden, and W. M. M. Kessels, *J. Phys. D: Appl. Phys.* **42**, 073001 (2009).
21. S. W. Kim, S. H. Kwon, D. K. Kwak, and S. W. Kang, *J. Appl. Phys.* **103**, 023517 (2008).
22. J. S. Mayell and S. H. Langer, *J. Electrochem. Soc.* **111**, 438 (1964).
23. J. S. Mayell, *J. Electrochem. Soc.* **113**, 385 (1966).
24. Y. Gong and M. Zhou, *Chemphyschem* **11**, 1888 (2010).
25. W. M. M. Kessels, H. C. M. Knoops, S. A. F. Dielissen, A. J. M. Mackus, and M. C. M. van de Sanden, *Appl. Phys. Lett.* **95**, 013114 (2009).
26. J. F. Weaver, J. J. Chen, and A. L. Gerrard, *Surf. Sci.* **592**, 83 (2005).
27. L. Ono, B. Yuan, H. Heinrich, and B. Cuenya, *J. Phys. Chem. C* **114**, 22119 (2010).
28. Y. Abe, M. Kawamura, and K. Sasaki, *Jpn. J. Appl. Phys.* **38**, 2092 (1999).
29. J. J. Blackstock, D. R. Stewart, and Z. Li, *Applied Physics A-Materials Science & Processing* **80**, 1343 (2005).
30. R. B. Getman, Y. Xu, and W. F. Schneider, *J. Phys. Chem. C* **112**, 9559 (2008).
31. D. H. Parker, M. E. Bartram, and B. E. Koel, *Surf. Sci.* **217**, 489 (1989).
32. N. Saliba, Y. L. Tsai, C. Panja, and B. E. Koel, *Surf. Sci.* **419**, 79 (1999).
33. J. F. Weaver, H. H. Kan, and R. Shumbera, *Journal of Physics-Condensed Matter* **20**, 184015 (2008).
34. M. Salmeron, L. Brewer, and G. A. Somorjai, *Surf. Sci.* **112**, 207 (1981).
35. K. Hauff, U. Tuttlies, G. Eigenberger, and U. Nieken, *Appl. Catal. B* **123**, 107 (2012).

36. K. Hauff, H. Dubbe, U. Tuttlies, G. Eigenberger, and U. Nieken, *Appl. Catal. B* **129**, 273 (2013).
37. F. Bernardi, M. C. Alves, A. Traverse, D. O. Silva, C. W. Scheeren, J. Dupont, and J. Morais, *J. Phys. Chem. C* **113**, 3909 (2009).
38. F. Bernardi, M. C. Alves, and J. Morais, *J. Phys. Chem. C* **114**, 21434 (2010).
39. W. Setthapun, W. D. Williams, S. M. Kim, H. Feng, J. W. Elam, F. A. Rabuffetti, K. R. Poeppelmeier, P. C. Stair, E. A. Stach, F. H. Ribeiro, J. T. Miller, and C. L. Marshall, *J. Phys. Chem. C* **114**, 9758 (2010).

Chapter 7

Controlling the Composition of Pt/PtOx ALD Films in High Aspect Ratio Trenches by tuning the Precursor Doses

Abstract

By controlling the substrate temperature and the (MeCp)$PtMe_3$ vapor and O_2 plasma doses, atomic layer deposition (ALD) can be used to deposit both Pt and PtO_x. The coating of high aspect ratio trenches poses an additional challenge to the control of the composition, as the precursor and plasma doses depend on the depth position inside the trench. Cross-section scanning electron microscopy (SEM) and energy dispersive x-ray spectroscopy (EDX) studies confirmed that at 100 °C under the dosing conditions chosen, spatially separated Pt and PtO_x can be simultaneously deposited in single trenches with aspect ratios of 9 and 22. Furthermore, it was demonstrated that the composition profile (Pt or PtO_x) of the deposited material inside HAR trenches can be tuned through the precursor and O_2 plasma exposure times.

Introduction

Pt thin films have many applications in the fields of catalysis, microelectronics, and sensing (1-4). Depending on its O/Pt ratio, PtO_x has several additional applications. For example, PtO_2 has been examined for catalytic oxidation of ethanol and CO, and PtO has been shown to catalytically enhance the performance of gas sensors (5,6). Many of these applications for Pt and/or PtO_x would benefit greatly from the use of high aspect ratio (HAR) nanostructured surfaces because of their increased surface-to-volume ratio (7). However, it is not trivial to deposit thin films of these materials with precise thickness control, and good uniformity in 3-D structures.

Atomic layer deposition (ALD) has proven to be a technique capable of depositing thin layers conformally on substrates containing HAR 3D topologies. Recently, we have demonstrated that ALD based on $(MeCp)PtMe_3$ and O_2 plasma offers the possibility to deposit planar thin films of both Pt and PtO_x ($2.2 < x < 2.7$) (8,9). Given the relatively high resistance of Pt against oxidation however, depositing Pt and PtO_x requires good control over both the O-radical dose and the $(MeCp)PtMe_3$ dose. As we have demonstrated, the composition of the deposited material depends on a careful balance between the oxidizing influence of the O-radicals and the reducing influence of the precursor molecules (9). During each O_2 plasma step, the surface layer of the deposited film is oxidized, provided the O_2 plasma exposure is sufficiently high. If this oxidic surface layer is not subsequently reduced, PtO_x is deposited. If the precursor dose is sufficiently high however, the oxidized surface layer that was formed during the O_2 plasma step can be reduced into metallic Pt by the precursor ligands. In this case Pt is deposited. The tendency of the deposited film to oxidize or reduce depends on the temperature. With increasing substrate temperature, the reducing activity of the precursor ligands will increase. Correspondingly, a higher O_2 plasma dose and/or lower $(MeCp)PtMe_3$ dose are required to obtain PtO_x at higher temperatures.

The deposition of Pt or PtO_x on planar substrate surfaces is therefore not trivial because of the dependency of the composition on temperature, and precursor and O_2 plasma doses. The challenge to deposit Pt or PtO_x films conformally on substrates with demanding 3D topology becomes even more challenging since precursor and O-radical doses may vary inside these 3D structures. For the deposition inside HAR structures, the precursor and co-reactant doses are generally optimized to ensure that saturation of the surface reactions is achieved throughout the features. However, it is also necessary that the delivered doses lead to the desired conformality as well as composition across the entire feature depths. Here, four aspects have to be considered.

Firstly, as described in Chapter 5, the (MeCp)PtMe$_3$ precursor and the O-radicals have close-to-unity sticking probability *s*. As a result, the wall collisions profile (i.e. the particle dose as a function of position inside the trench) depends on the position inside the trench and will change during the diffusion-limited deposition (10). In order to deliver the saturation dose to the deeper parts of the trench, a relatively large dose needs to be delivered to the more shallow parts of the trench. Secondly, considering the recombination probability *r* of 0.01 (see also Chapter 5), O-radicals can recombine at the Pt surface with O- atoms with a and be lost, whereas (MeCp)PtMe$_3$ molecules do not recombine (11). Thirdly, the required O-radical dose is much greater than the precursor dose, since approximately 20 O-radicals are required to combust the ligands of one (MeCp)PtMe$_3$ molecule (12). The collisions profile for precursor particles is therefore very different from that of O-radicals, which may have significant consequences for the composition of the deposited material inside HAR trenches. Finally, as discussed in Chapter 6, there are restrictions to the choice of precursor and O$_2$ plasma exposure doses as their interplay affects the composition (i.e. Pt vs. PtO$_x$) of the deposited film.

To gain control over the composition and compositional profile of Pt and PtO$_x$ inside HAR trenches, the influence of the (MeCp)PtMe$_3$ precursor and O$_2$ plasma exposures on the composition of ALD-deposited films inside HAR trenches has been studied in this work. The composition of films deposited in trenches with aspect ratios of 9 and 22 has been examined using a combination of cross-section scanning electron microscopy (SEM) and energy dispersive X-ray spectroscopy (EDX). The obtained composition profiles will be interpreted, and the implications for ALD of Pt and PtO$_x$ will be discussed. The insights gained here are also relevant for other noble metal ALD processes for which the composition of the deposited material depends on precursor and/or reactant doses, such as Ir/IrO$_x$ and Ru/RuO$_x$ (13-15).

Experimental setup

All depositions were performed in an open-load ALD reactor as described before (12). The deposition chamber containing the substrate heating stage is connected to a turbomolecular pump through a gate valve. An inductively coupled plasma source, operated at 100 W input power, is located approximately 30 cm above the heating stage. This remote plasma source is connected to the deposition chamber through another gate valve. Oxygen is fed into the reactor through the plasma source. The pressure inside the deposition chamber varied from a base pressure in the order of $7.5 \cdot 10^{-3}$ mTorr during the pump-down step in the ALD cycle, to 75 mTorr during the O_2 pulse. The temperature of the reactor walls was kept at 80 °C for all depositions. The substrate temperature was always 100 °C. The $(MeCp)PtMe_3$ precursor (98 % purity, Sigma-Aldrich) was kept at 30 °C and was injected into the reactor through a back flange using Ar as a carrier gas at a pressure of ~7.5 mTorr.

Films were deposited on Si trench-samples with trench arrays etched with deep reactive ion etching (DRIE) (16). The trenches had the following *AR*s and dimensions (depth [µm] x width [µm]): *AR* 9 (30.4 x 3.4), *AR* 22 (22 x 1). After the trench etching the Si trench-substrates were covered with approximately 100 nm of thermally grown SiO_2. The ALD process using $(MeCp)PtMe_3$ and O_2 plasma was used for 4 separate deposition series (labelled A,B,C, and D) with the following O_2 plasma and precursor exposure times in seconds: A: 5/5, B: 10/5, C: 10/10, D: 20/10. During each deposition, both the *AR* 9 and *AR* 22 trenches were coated simultaneously. In the discussion below, the individual trench samples are named according to their O_2 plasma/precursor exposure label and their aspect ratio, e.g. A9 refers to the sample with *AR* 9 with 5 s O_2 plasma and 5 s precursor exposure. Each deposition consisted of 1500 cycles.

Cross-section SEM images were used to characterize the films deposited in each of the trenches of interest. Trench samples were imaged after they were cleaved perpendicular to the trench heartline as illustrated in Figure 7.1 (a). SEM images were made on a high-resolution JEOL 7500 FA microscope using secondary electron imaging mode. In addition, energy dispersive X-ray spectroscopy (EDX) was used to determine the composition of the deposited material of trench A9. EDX measurements were carried out perpendicular to the cleavage plane, using an EDAX spectrometer with an

SUTW window installed on an FEI Nova 600 DualBeam system. The X-rays were collected at a take-off angle of 35°. For each film segment, an EDX spectrum was obtained by measuring at a fixed position in the center of the deposited layer for 30 seconds with constant beam current (0.4 nA at a voltage of 5 kV). The radius of the spot size was in the order of 20 nm, while the thickness of the deposited layer of trench A9 was ~90 nm at the trench top and ~80 nm at the trench bottom. Therefore, some of the collected X-rays may originate from the SiO_2 underlayer on which the ALD layer was deposited.

Aspect ratio depth

In this work, we will often compare features inside trenches with different aspect ratios and dimensions. A convenient unit for these comparisons is the *normalized position* defined as the aspect ratio depth (*ARD*):

$ARD = D/W.$ (Equation 7.1)

Here, *D* is the depth position along the trench wall and *W* is the width of the trench. *ARD* therefore represents the position along the trench wall, normalized for the width of the trench. For example, a feature located 15.3 µm down trench A9 (*W* = 3.4 µm) has an *ARD* of 4.5. However, a feature located 15.3 µm down trench A22 (*W* = 1 µm) has an *ARD* of 15.3.

Using *ARD* when comparing features between trenches with different dimensions is convenient since only the aspect ratio determines the shape of the particle dose profiles (10). After all, the composition of the deposited films depends on the precursor and O-radical dose delivered to the surface. According to kinetic theory, the mean free paths of the diffusing gas particles at their respective pressures of 75/7.5 mTorr are larger than the dimensions of the trenches used here, which means that the particles can be considered to be in the molecular flow. As a result, particles can be assumed to only interact with the walls and not with each other, such that only the aspect ratio of the trench influences the collision profiles.

Results

SEM

We will first discuss the results for sample A9 quite extensively since it can serve as an example for the other samples. The SEM images for sample A9 are shown in Figure 7.1. Figure 7.1 (a) shows an overview of the entire trench. Figures 1 (b-h) show close-ups of cross-sections of the trench from the trench opening down to the bottom. Figure 7.1 (b) shows the top part of the trench which displays a periodic roughness (so-called scallops), which is characteristic for the Bosch DRIE etching process (16). The scallop curvature is most pronounced in the top part of the etched trench, but it can also be seen in the other images for parts deeper in the trench. In Figure 7.1 (d) the Si substrate, the thermal SiO_2 layer, and the ALD-deposited layer are all indicated for clarity.

In Figures 1 (b-d), the deposited layer is very similar in brightness to the SiO_2 layer, and appears relatively dark. Figure 7.1 (e) shows a section of the trench wall halfway down the trench. Remarkably, a transition in the brightness of the deposited layer can be observed, as indicated by the arrow in image (e). In the top half of Figure 7.1 (e), the deposited layer appears dark, similar to the thermally-grown SiO_2 layer underneath. In the bottom half of the image however, the deposited layer appears much brighter, and a clear brightness distinction can be observed between the deposited layer and the SiO_2. This change in contrast indicates a change in the composition of the deposited material, since the contrast depends on the number of detected secondary electrons. The escape probability of the secondary electrons depends on the work function of the imaged material, and therefore, on the composition (17). Figures 1 (f-g) show sections located further down the trench. In these images, the deposited layer also appears relatively bright compared to the underlying SiO_2 layer. In Figure 7.1 (h), the lowest part of the trench wall and part of the trench bottom are shown. As can be seen, the layer deposited on the trench wall appears bright, while the layer deposited on the actual trench bottom appears darker. Based on these and additional images (not shown here) it was established that the deposited material appeared darker from the top of the trench down to *ARD* 4.5. For $4.5 < ARD < 9$, the material deposited on the trench walls appeared bright white, while on the trench bottom (*ARD* = 9) the deposited material appeared dark. The brightness profile showed a clear symmetry with respect to the trench heartline, i.e. the transition in brightness was observed at the same height for both sidewalls of the same trench. This therefore suggests that two distinct materials with different composition were deposited inside trench A9. This hypothesis has been confirmed by performing EDX studies, as will be discussed below.

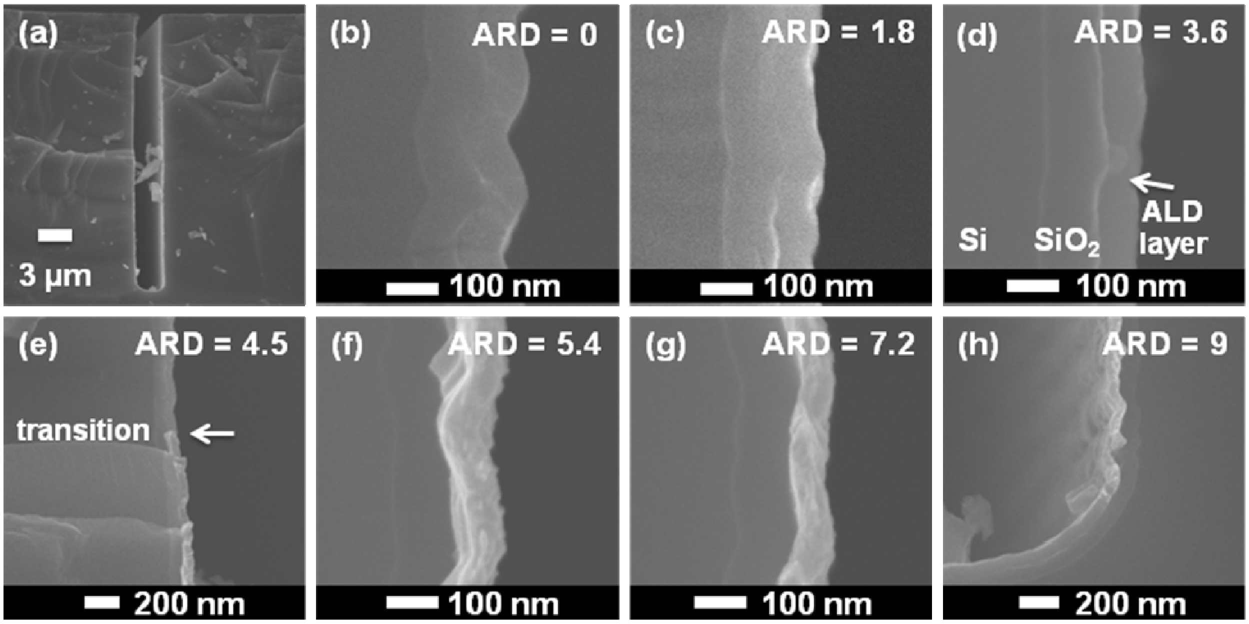

Figure 7.1. *SEM images of an ALD film deposited using 1500 cycles of (MeCp)PtMe*$_3$ *(5 s exposure) and O*$_2$ *plasma (5 s exposure) in a trench that has an aspect ratio of 9 (trench A9). The trench is etched in Si, and then covered with a 100 nm thermally grown SiO*$_2$ *film. The images show the side views of (a) the full trench, and (b-h) a subsequent series of images from trench top to trench bottom.*

A similar trend in the transition in brightness of the deposited layer as a function of height were made for trench A22. Figure 7.2 shows cross-section SEM images of trench A22. Figure 7.2 (a) shows an overview of the entire trench, while Figures (b-g) show higher magnification images from the entrance of the trench down to the bottom. In Figure 7.2 (b) the deposited layer appears dark, while in Figure 7.2 (c) a transition can be seen from dark in the top part, towards brighter white in the lower part. In Figure 7.2 (d-g) the deposited layer appears bright white, even on the trench bottom. Again, based on these and additional images it was established that the deposited layer appears dark from the top of the trench down to *ARD* 5.5, and bright white from *ARD* = 5.5 down to the trench bottom.

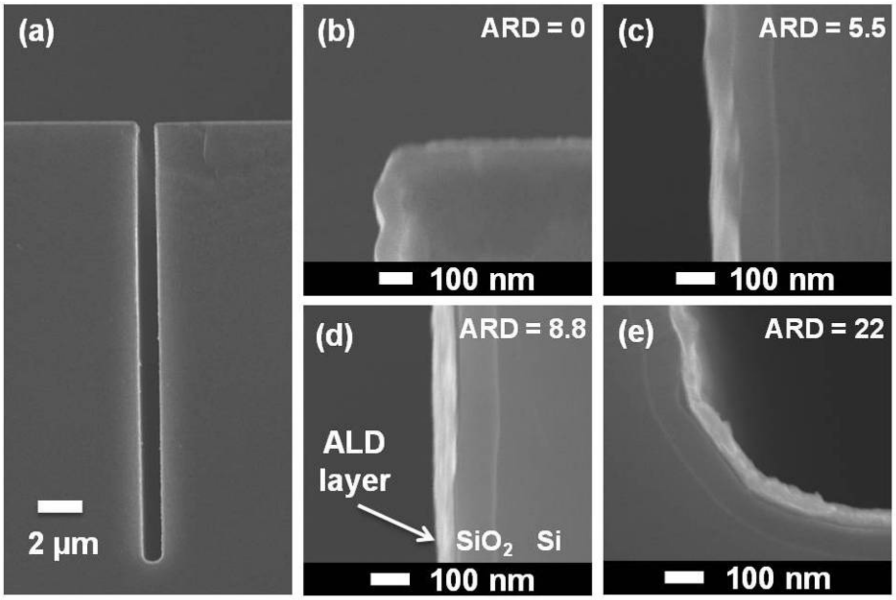

Figure 7.2. *SEM images of an ALD film deposited using 1500 cycles of (MeCp)PtMe$_3$ (5 s exposure) and O$_2$ plasma (5 s exposure) in a trench (trench A22). The trench has an aspect ratio of 22 and is etched in Si, covered with a 100 nm thermally grown SiO$_2$ film. The images show the side views of (a) the full trench, and (b-e) a subsequent series of images from trench top to trench bottom.*

EDX

EDX measurements were performed to determine the composition of the deposited material along the trench walls and bottom of trench A9. As an example, two spectra that were measured 13 µm down the trench (*ARD* = 3.8) and 24 µm down the trench (*ARD* = 7) are shown in Figure 7.3 (a) and (b), respectively. Both spectra display the Pt Mα peak originating from the deposited ALD-film, the Si Kα peak originating from the SiO$_2$ layer on which the ALD-film was deposited, and the O Kα peak from both the ALD-film and the SiO$_2$ layer. The peaks of the C Kα signal (0.28 keV) and the Pt N signal (0.25 keV) are challenging to assign due to their overlap. The spectrum shown in Figure 7.3 (a), displays a relatively intense O-peak and weaker Pt-peak compared to the spectrum shown in Figure 7.3 (b). The Si-peaks in both spectra have similar intensity. This indicates that the ALD-film consists of PtO$_x$ at *ARD* = 3.8, while it consists of oxygen-poor Pt at *ARD* = 7. From these EDX studies, one cannot unambiguously prove that the oxygen-poor regions consist of metallic Pt. However, taking into account the difference of nearly an order of magnitude in oxygen peak heights between the oxygen-rich and -poor regions and the fact that no stable platinum oxides have been reported with an O/Pt ratio below 1, we conclude that the oxygen-poor regions to consist of metallic Pt. The small oxygen-peak measured in these regions most likely originates from the SiO_2 substrate layer.

In Figure 7.4, the intensity of the O-peak (corrected for background signal) is plotted as a function of trench depth. In the upper part of the trench the intensity is high, indicating the presence of PtO_x. At an ARD of approximately 4.4, the O-peak intensity drops, indicating a relatively sharp transition from PtO_x to Pt. The intensity is low for the entire lower part of the trench, with the exception of the very trench bottom, where the intensity increases again.

If the results from Figure 7.4 are compared to the images from Figure 7.1, it becomes apparent that the dark film segments in Figure 7.1 (b-d) correspond to PtO_x films. The transition from dark to bright film segments in Figure 7.1 (e) coincides with the decrease in O-peak intensity in Figure 7.4. Clearly, the composition of the deposited film changes from PtO_x to Pt at this point. Based on both Figure 7.1 (e) and Figure 7.4, the distance over which the transition in composition takes place seems confined to several µm. The bright film segments in Figure 7.1 (f, g) are clearly of Pt deposited in the region from *ARD* = 4.5 down to *ARD* = 9. The transition in brightness near the trench bottom shown in Figure 7.1 (h) coincides with the increase in O-peak intensity in Figure 7.4 and is clearly due to a transition from Pt to PtO_x.

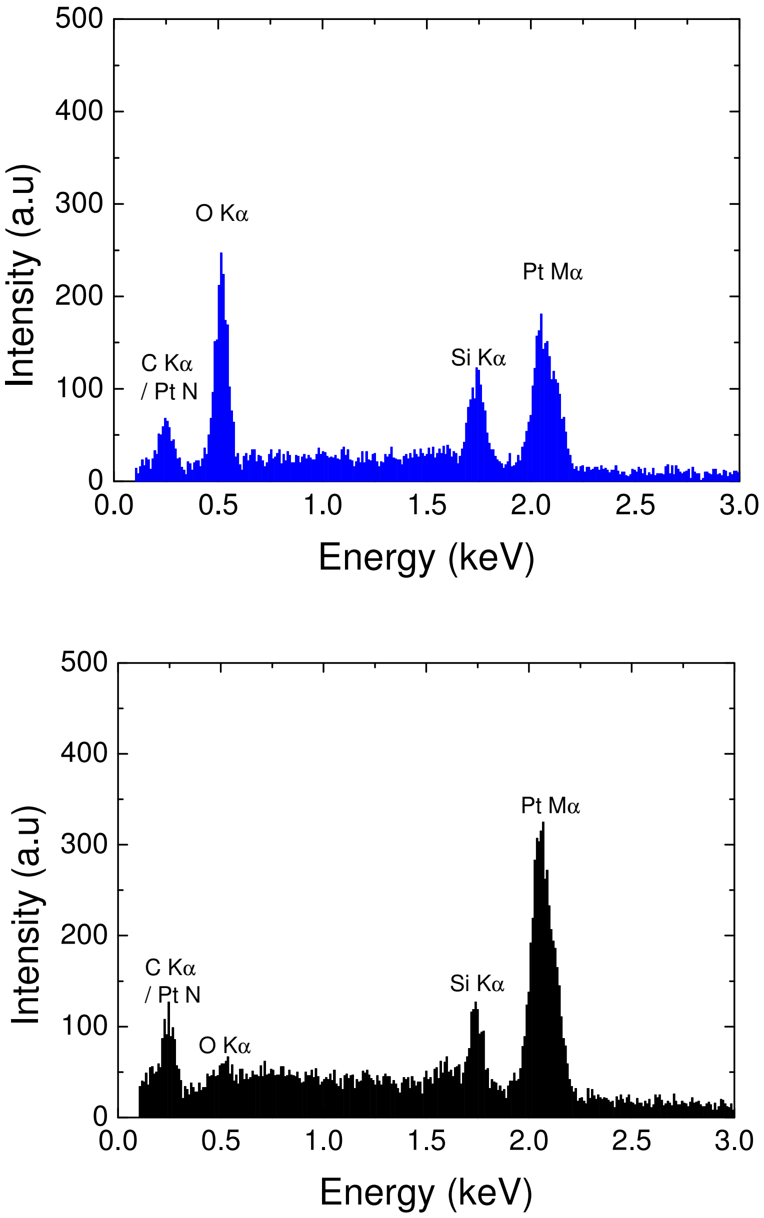

Figure 7.3. *EDX spectra acquired by spot analysis halfway the thickness of the deposited Pt/PtOx layer, measured (a) at ARD = 3.8 in trench A9, and (b) at ARD = 7 in trench A9. Both spectra display the Pt-Mα peak from the ALD-film, the Si-Kα peak originating from the* SiO_2 *layer on which the ALD-film was deposited, and O Kα peaks from either the ALD-film or the* SiO_2 *layer. The peak that appears at approximately 0.25 keV is that the position of C Kα (0.28 keV) and Pt N (0.25 keV) and can therefore not be uniquely assigned.*

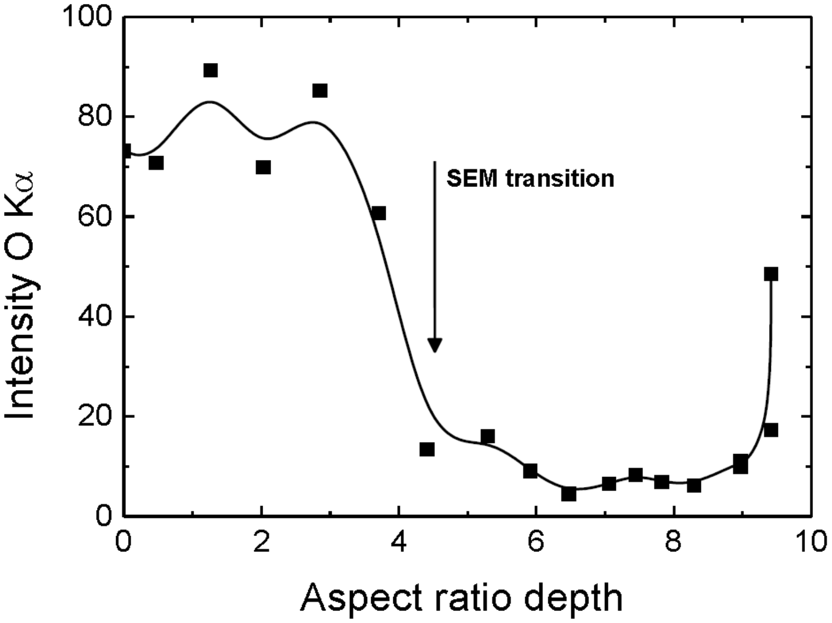

Figure 7.4. Intensity of the O-Kα peak as measured using EDX, as a function of depth for trench A9. The line serves as a guide to the eye.

Given the agreement between the EDX results and the brightness profiles visible in the SEM images, the composition of the deposited layer for the other trenches (series B, C, and D) was determined based solely on SEM images. A more elaborate and representative selection of these SEM images can be found in the Appendix. Schematically represented results as a function of *ARD* for all the deposition experiments are summarized in Figure 7.5. In this figure, the composition is indicated by color for each trench: red for PtO_x and blue for Pt. Each trench is depicted schematically, and only the left part of each trench is shown, since the deposition profiles were symmetric. For clarity, the precursor and O_2 plasma exposure times are indicated above. The black braces indicate these trench areas for which it was more challenging to determine the composition due to peel-off of the deposited layers that occurred in sample preparation for SEM inspection. This peeling is due to the poor adhesion between the Pt / PtO_x layer and the SiO_2. Despite this peeling however, the composition could still be determined with reasonable certainty.

Figure 7.5 shows that for trenches A9 and A22, PtO_x is deposited in the top part of the trench for 0 < *ARD* < ~5. This illustrates the advantage of comparing the deposition profiles in terms of *ARD*. In both trenches Pt is deposited down the remainder of the trench, with the exception that for A9

PtO_x is deposited at the very bottom. The similarity in the composition profiles (when regarded as a function of *ARD*) can be attributed to the identical precursor and O_2 plasma exposures that were used for both trenches. This is evidence for the assumption that for trenches of these dimensions, the collision profile of the particles is determined by the aspect ratio rather than the actual dimensions of the trench.

Figure 7.5 furthermore shows that when the O_2 plasma exposure time is increased to 10 s, PtO_x is deposited throughout both trenches, as indicated for B9 and B22. If then the precursor exposure time is also increased to 10 s (C9 and C22), Pt is again deposited for *ARD* > ~5 with the exception of the trench bottoms. Finally, precursor and O_2 plasma exposure times of 10 and 20, respectively, again result in the deposition of PtO_x throughout both trenches.

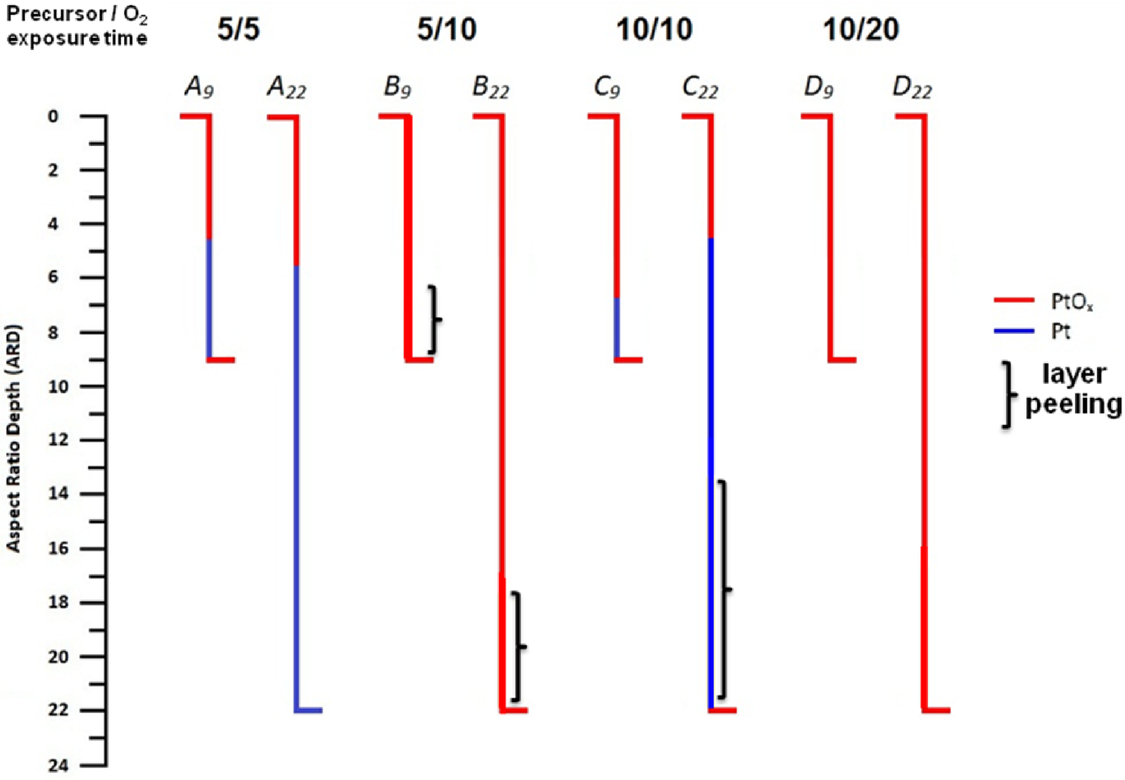

Figure 7.5. *Schematic representation of the composition profiles of the ALD-films in the trenches, indicating the deposition of either* PtO_x *(red) or Pt (blue). The black braces indicate trench segments where layer peeling occurred during SEM sample preparation. The precursor and* O_2 *plasma exposure times (in s) are indicated for clarity.*

Discussion

For ALD using (MeCp)PtMe$_3$ vapor and O$_2$ plasma, the composition of the deposited material depends on the balance between the O-radical dose and the precursor dose. The composition of the deposited material tends to be PtO$_x$ for higher O-radical doses and/or lower precursor doses. Figure 7.5 shows that for a precursor and O$_2$ plasma exposure time of 5 s, PtO$_x$ is deposited in the top parts of the trenches (0 < *ARD* < ~5). Clearly, the O-radical dose in this segment is high enough to create stable PtO$_x$. In the lower parts of the trench (*ARD* > ~5) Pt is deposited, with the exception of the bottom of trench A9. The deposition of Pt in the lower parts of the trench can be ascribed to a change in the ratio of the precursor/plasma doses. This change in the ratio can be due to either an increase in the precursor dose, or to a decrease in the O-radical dose as a function of *ARD*. Given that both the precursor and O-radical doses will decrease as a function of *ARD*, the formation of Pt is apparently due to a decrease in the O-radical dose. Deposition of PtO$_x$ on the bottom of trench A9 can be explained by the O-radical dose that is caused by O-radicals impinging on the bottom without first interacting with the walls (i.e. direct *line-of-sight* impact) (10).

The assumption that the deposition of Pt can be ascribed to a reduced O-radical dose is consistent with the observation that for an increased O$_2$ plasma exposure time PtO$_x$ is deposited throughout both trenches. This is shown in Figure 7.5 for trenches B9 and B22, where the O$_2$ plasma exposure time was increased to 10 s. This demonstrates again that the composition of the deposited material inside the trenches can be controlled using the O$_2$ plasma exposure time.

For the deposition in trenches C9 and C22, the precursor exposure time was increased to 10 s. This led to a composition profile that is roughly the same as that of deposition A. Given that the O$_2$ plasma exposure times for depositions B and C are the same and only the precursor exposure time changed, this is clear evidence of the reducing activity of the precursor. This experiment also demonstrates that the O$_2$ plasma and precursor exposure times can be used independently to control the composition of the deposited material inside the trenches. This is demonstrated once more by the composition profiles of trenches D9 and D22, which are virtually identical to those of B9 and B22.

We furthermore note that the deposition of Pt is remarkable since plasma-assisted ALD of Pt without any additional reducing gasses at 100 °C has not been reported before to the best of our knowledge. Clearly, the O-radical dose in the trenches can be tuned such that it is high enough to saturate Pt ALD-surface reactions but low enough to prevent the formation of stable PtO_x at 100 °C.

Our findings emphasize that in order to deposit either Pt or PtO_x inside HAR features, the O-radical and precursor dose must be well controlled to ensure the desired composition of the deposited material. This can be done directly by controlling the O_2 plasma and precursor exposure times. For the deposition of Pt inside HAR features, it may be necessary to deposit either at higher substrate temperatures, or make use of an additional reducing gas/plasma (i.e. H_2). For the deposition of PtO_x sufficiently high O-radical doses are required, preferably with minimal precursor doses.

Finally, we note that the observations reported here may also be relevant for other noble metal (oxide) ALD processes such as Ir/IrO_x and Ru/RuO_x (13-15). For example, the composition of the deposited material in the Ir/IrO_2 ALD process has also been shown to depend on temperature and oxygen pressure (13).

Conclusion

Both Pt and PtO_x can be deposited inside high aspect ratio trench structures using plasma-assisted ALD at 100 °C. The composition and compositional profile were found to depend on the $(MeCp)PtMe_3$ precursor and O_2 plasma doses, which can be tuned by controlling the precursor and O_2 plasma exposure times. This stems from the fact that inside HAR trenches, the O-radical and precursor doses depend on the vertical depth position inside the trench (i.e. the aspect ratio depth (*ARD*)). At the conditions under which both materials were deposited inside the same trench, PtO_x was deposited in the upper parts of the trench, while Pt was deposited in the lower parts. By increasing the O_2 plasma exposure time the transition from PtO_x to Pt could be shifted deeper into the trench. Conversely, by increasing the precursor exposure time this transition could be shifted towards the upper parts of the trench. Furthermore, this work demonstrates that Pt can be deposited using plasma-assisted ALD at 100 °C without additional reducing gasses.

Bibliography

1. N. Fu, X. Xiao, X. Zhou, J. Zhang, and Y. Lin, *J. Phys. Chem. C* **116**, 2850 (2012).
2. L. C. Tien, P. W. Sadik, D. P. Norton, L. F. Voss, S. J. Pearton, H. T. Wang, B. S. Kang, F. Ren, J. Jun, and J. Lin, *Appl. Phys. Lett.* **87**, 222106 (2005).
3. A. L. Marsh and J. L. Gland, *Surf. Sci.* **536**, 145 (2003).
4. C. T. Hsieh, Y. Y. Liu, D. Y. Tzou, and W. Y. Chen, *J. Phys. Chem. C* **116**, 26735 (2012).
5. M. D. Ackermann, T. M. Pedersen, B. L. M. Hendriksen, O. Robach, S. C. Bobaru, I. Popa, C. Quiros, H. Kim, B. Hammer, S. Ferrer, and J. W. M. Frenken, *Phys. Rev. Lett.* **95**, 255505 (2005).
6. D. Haridas, K. Sreenivas, and V. Gupta, *Sensors and Actuators B-Chemical* **133**, 270 (2008).
7. G. Pardon, H. K. Gatty, G. Stemme, W. van der Wijngaart, and N. Roxhed, *Nanotechnology* **24**, 015602 (2013).
8. H. C. M. Knoops, A. J. M. Mackus, M. E. Donders, M. C. M. van de Sanden, P. H. L. Notten, and W. M. M. Kessels, *Electrochem. Solid-State Lett.* **12**, G34 (2009).
9. I. J. M. Erkens, H. C. M. Knoops, T. F. Landaluce, A. J. M. Mackus, M. Verheijen, F. Roozeboom, and W. M. M. Kessels, *Accepted for publication in Chemical Vapor Deposition* (2014).
10. H. C. M. Knoops, E. Langereis, M. C. M. van de Sanden, and W. M. M. Kessels, *J. Electrochem. Soc.* **157**, G241-G249 (2010).
11. D. S. Hacker, S. A. Marshall, and M. Steinberg, *J. Chem. Phys.* **35**, 1788 (1961).
12. I.J.M. Erkens, A. J. M. Mackus, H. C. M. Knoops, P. Smits, T.H.M. van de Ven, F. Roozeboom, and W. M. M. Kessels, *ECS Journal of Solid State Science and Technology* **1**, 255 (2012).
13. S. W. Kim, S. H. Kwon, D. K. Kwak, and S. W. Kang, *J. Appl. Phys.* **103**, 023517 (2008).
14. T. Aaltonen, P. Alen, M. Ritala, and M. Leskelä, *Chem. Vap. Deposition* **9**, 45 (2003).
15. K. G. Kreider, M. J. Tarlov, and J. P. Cline, *Sensors and Actuators B-Chemical* **28**, 167 (1995).

16. F. Lärmer et al., *in Handbook of Silicon Based MEMS Materials and Technologies (eds. V. Lindroos et al.),Elsevier (Oxford, 2010) p. 349.* (2010).
17. J. Cazaux, *Journal of Electron Microscopy* **61**, 261 (2012).

Appendix: SEM images

Figure 5 shows a schematic representation of the composition profiles of ALD films deposited inside the trenches A9 through D22. Each segment is indicated to consist of either PtO_x or Pt. The composition has been determined on the basis of the brightness of the deposited film compared to the brightness of the thermally grown SiO_2 layer underneath in SEM images of the respective trenches. In this appendix, we show a representative selection of these images for trenches B9 through D22. As mentioned before, the individual trench samples are named according to their O_2 plasma/precursor exposure times (A: 5/5, B: 10/5, C: 10/10, D: 20/10) and their aspect ratio, e.g. A9 refers to the sample with *AR* 9 with 5 s O_2 plasma and 5 s precursor exposure.

SEM images for trench B9

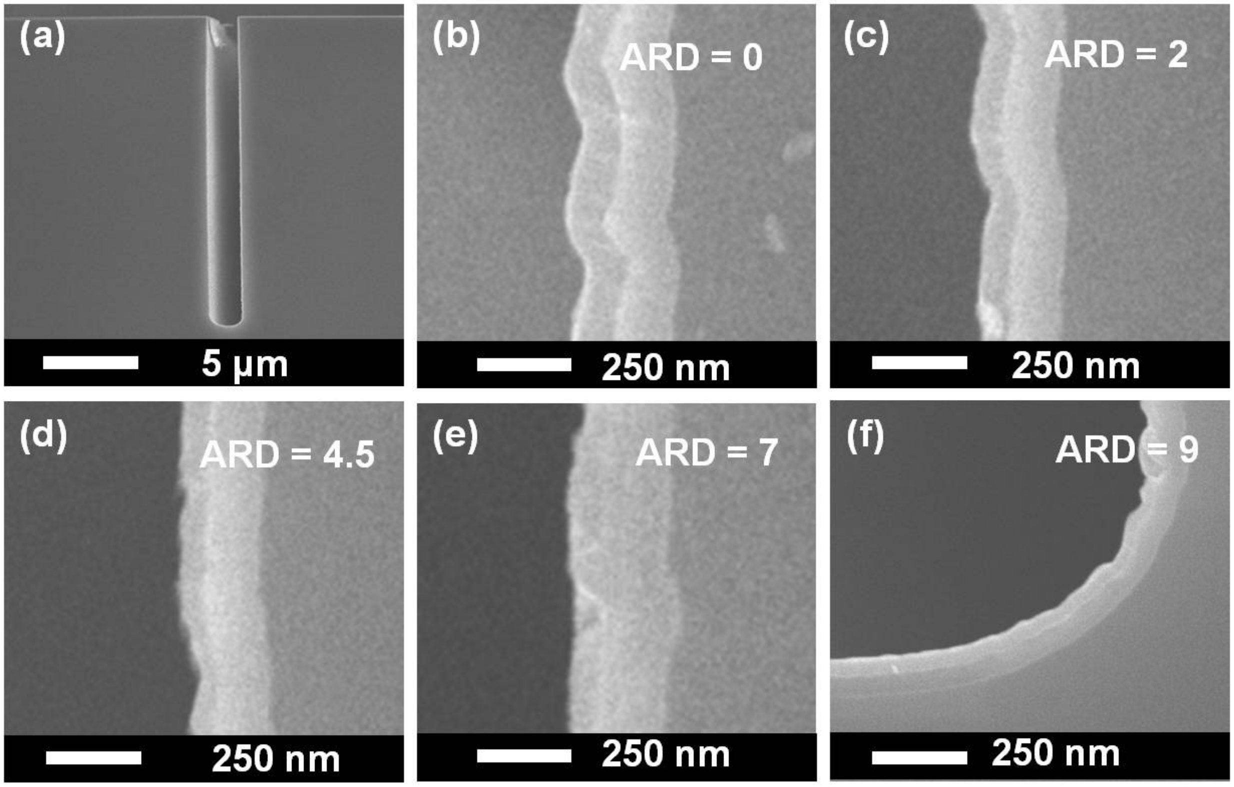

Figure 7.6. *SEM images of an ALD film deposited using 1500 cycles of (MeCp)PtMe₃ (5 s exposure) and O_2 plasma (10 s exposure) in the trench. The trench has an aspect ratio of 9 and has been etched in Si, covered with a 100 nm thermally grown SiO_2 film. The images show the side views of (a) the full trench, and (b-f) a subsequent series of images from trench top to trench bottom, their*

positions indicated by the aspect ratio depth (ARD). In this trench, PtOx is observed along the entire trench wall.

SEM images for trench B22

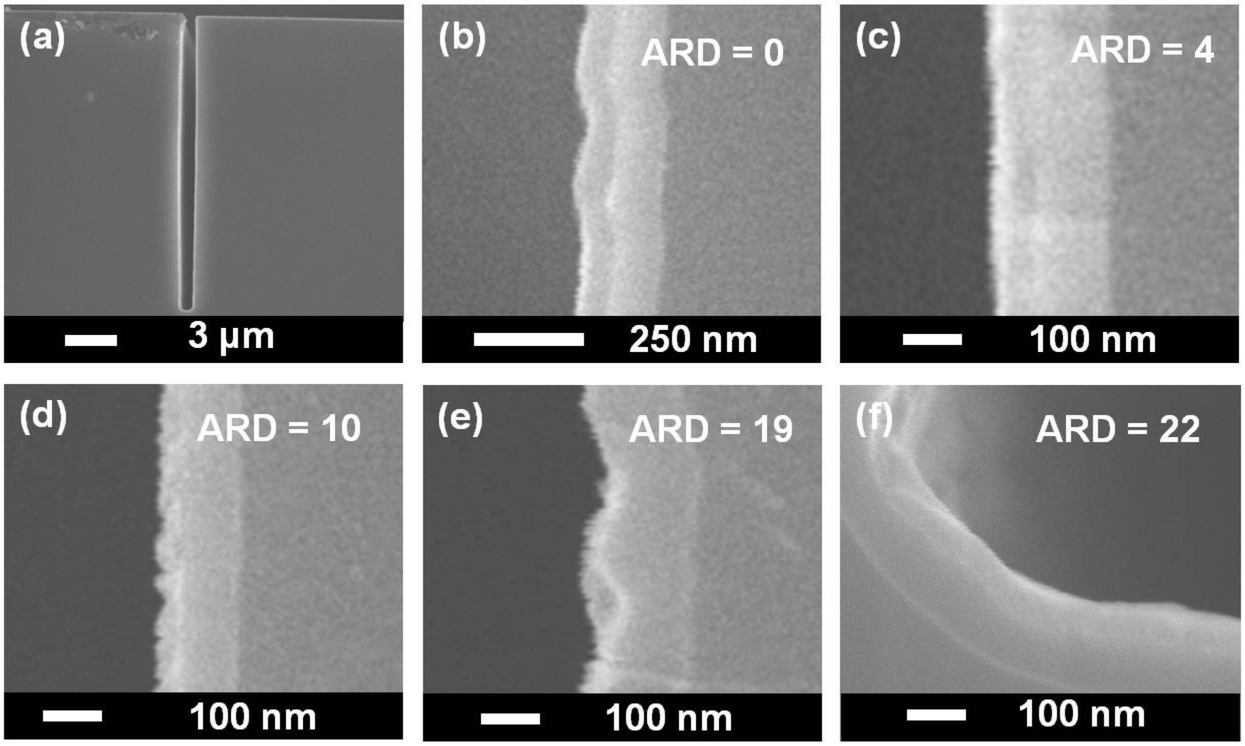

Figure 7.7. *SEM images of an ALD film deposited using 1500 cycles of (MeCp)PtMe$_3$ (5 s exposure) and O$_2$ plasma (10 s exposure) in the trench. The trench has an aspect ratio of 22 and has been etched in Si, covered with a 100 nm thermally grown SiO$_2$ film. The images show the side views of (a) the full trench, and (b-f) a subsequent series of images from trench top to trench bottom. In this trench, PtOx is observed along the entire trench wall.*

SEM images for trench C9

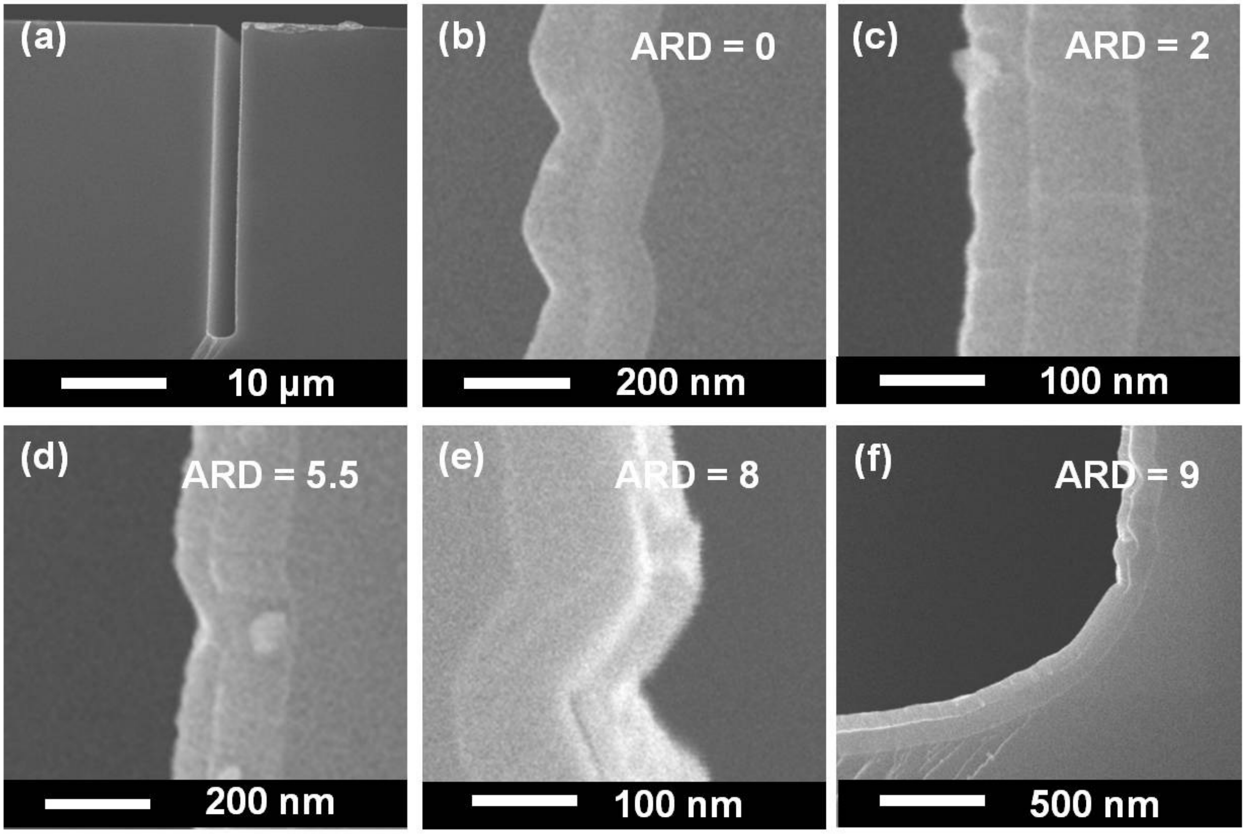

Figure 7.8. *SEM images of an ALD film deposited using 1500 cycles of (MeCp)PtMe*$_3$ *(10 s exposure) and O*$_2$ *plasma (10 s exposure) in the trench. The trench has an aspect ratio of 9 and has been etched in Si, covered with a 100 nm thermally grown SiO*$_2$ *film. The images show the side views of (a) the full trench, and (b-f) a subsequent series of images from trench top to trench bottom. In this trench, a higher brightness region is observed in image (e).*

SEM images for trench C22

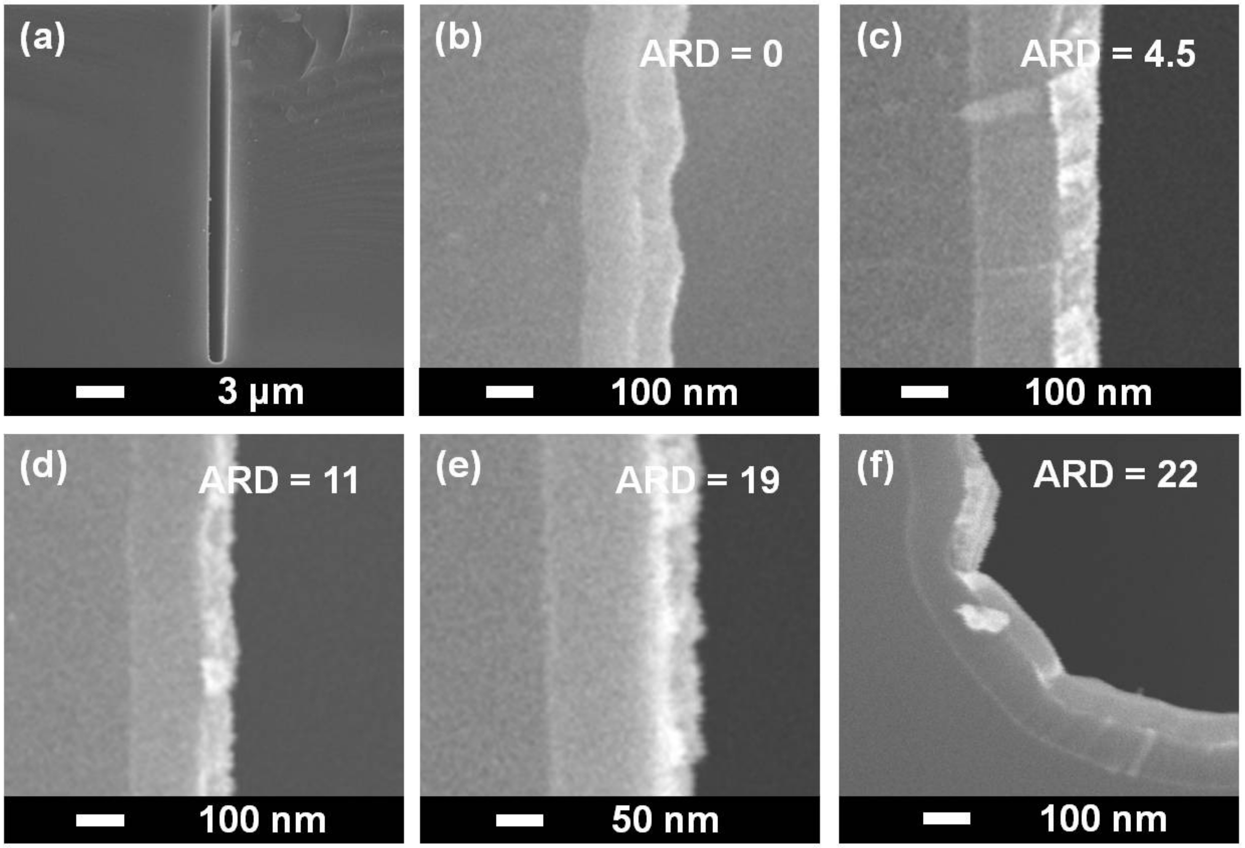

Figure 7.9. *SEM images of an ALD film deposited using 1500 cycles of (MeCp)PtMe$_3$ (10 s exposure) and O$_2$ plasma (10 s exposure) in the trench. The trench has an aspect ratio of 22 and has been etched in Si, covered with a 100 nm thermally grown SiO$_2$ film. The images show the side views of (a) the full trench, and (b-f) a subsequent series of images from trench top to trench bottom. In this trench, a higher brightness region is observed stretching from ARD = 4.5 to 22.*

SEM images for trench D9

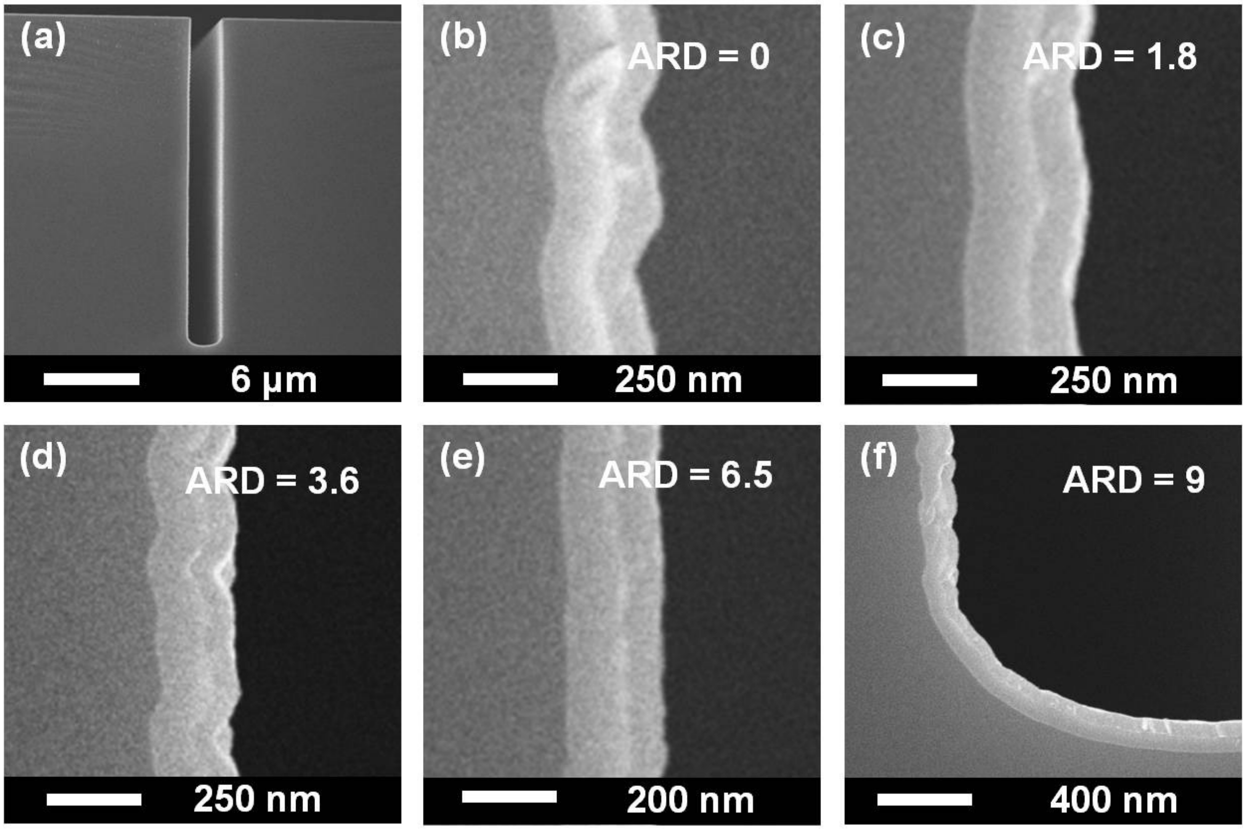

Figure 7.10. *SEM images of an ALD film deposited using 1500 cycles of (MeCp)PtMe$_3$ (10 s exposure) and O$_2$ plasma (20 s exposure) in the trench. The trench has an aspect ratio of 9 and has been etched in Si, covered with a 100 nm thermally grown SiO$_2$ film. The images show the side views of (a) the full trench, and (b-f) a subsequent series of images from trench top to trench bottom. In this trench, PtOx is observed along the entire trench wall.*

SEM images for trench D22

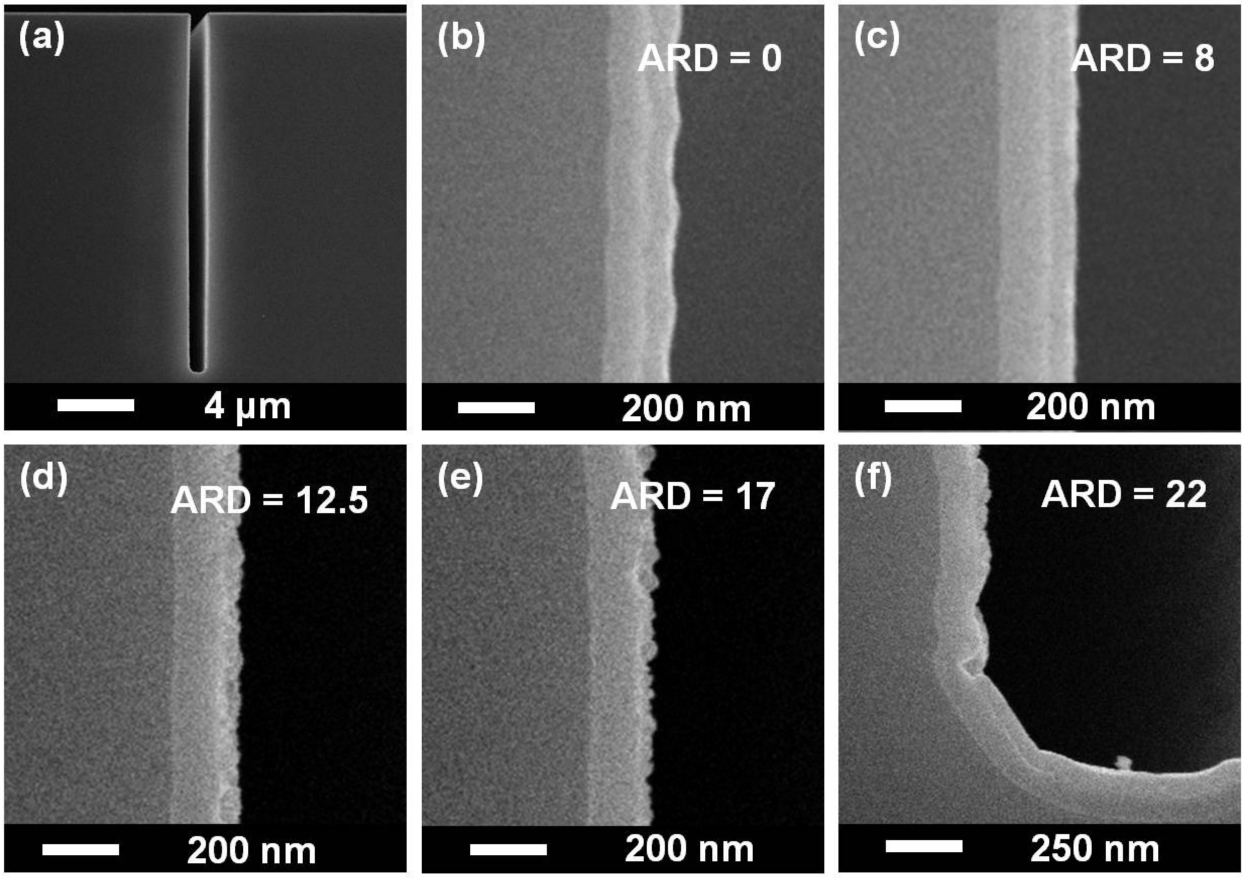

Figure 7.11. *SEM images of an ALD film deposited using 1500 cycles of (MeCp)PtMe*$_3$ *(10 s exposure) and O*$_2$ *plasma (20 s exposure) in the trench. The trench has an aspect ratio of 22 and has been etched in Si, covered with a 100 nm thermally grown SiO*$_2$ *film. The images show the side views of (a) the full trench, and (b-f) a subsequent series of images from trench top to trench bottom. In this trench, PtOx is observed along the entire trench wall.*

Chapter 8

Room Temperature Sensing of O_2 and CO by Atomic Layer Deposition Prepared ZnO Films Coated with Pt Nanoparticles*

Abstract

Ultralow-power gas sensing devices need to operate without an energy consuming heater element. This requires the design of sensing devices that are so efficient that they can operate at room temperature (RT). Here, we report on the RT sensing performance of atomic layer deposition (ALD) prepared *i*-ZnO and Al-doped ZnO sensing devices. The sensitivity of these devices has been catalytically enhanced with ALD Pt nanoparticles (NPs). It was shown that the size distribution of the Pt NPs can be controlled by the number of Pt-ALD cycles. The Pt-enhanced sensing devices showed a reversible, proportional change in current response at RT upon exposure to O_2 and CO. O_2 could be detected, diluted in N_2, down to 0.5%. CO could be detected, diluted in N_2 in the presence of O_2 and H_2O, down to 20 ppm. Reference devices without Pt NPs showed no response, indicating the importance of the Pt NPs for the sensing mechanism.

*Published as: I.J.M. Erkens, M.A. Blauw, M.A. Verheijen, F. Roozeboom and W.M.M. Kessels, *ECS transactions* **58,** 203 (2013)

Introduction

Metal-oxide (MO) thin-film gas sensors have attracted a lot of attention due to their low cost, simple fabrication, and long life (1). Zinc oxide (ZnO) is considered one of the most promising materials for gas-sensing applications, because of its chemical sensitivity to many gases, high chemical stability, suitability to doping, non-toxicity, and low cost (2). The working principle of most MO-based gas sensors depends on the change in conductivity of the MO layer upon a change in concentration of oxidizing or reducing gases in the environment of the sensor (1,3). The sensing mechanism is mainly governed by oxygen vacancies on the surface which are electrically and chemically active. In an n-type semiconductor MO, the majority charge carriers are electrons. When a layer of the MO is exposed to charge-accepting molecules such as O_2, oxygen species (O_2^-, O^-, O^{2-}) are ionosorbed on the surface, where they will trap electrons from the conduction band of the MO layer (4). The trapping of electrons leads to a reduction of the conductivity of the MO layer, proportional to the concentration of the oxidizing gas (1,3). Therefore, by measuring the change in conductivity, the gas concentration can be determined. Similarly, reducing molecules can be detected, provided ionosorbed surface oxygen species are available (from O_2 in the ambient). In this case, molecules such as CO and H_2 can react with the surface-adsorbed oxygen thereby releasing trapped electrons and increasing the conductance. For e.g. O_2 and CO the gas sensing responses by an n-type MO can therefore be represented as follows:

Oxidizing response: $O_2\,(g) + e^- \rightarrow O_{2\,surface}^-$. (Equation 8.1)

Reducing response: $CO\,(g) + O^-_{surface} \rightarrow CO_2\,(g) + e^-$ (Equation 8.2)

For p-type MO films where the majority charge carriers are holes, the reaction mechanism with respect to reducing/oxidizing response will be reversed: the trapping of electrons (oxidizing response) will lead to an increase in the number of holes, and therefore to an increased conductivity (5,6). Although it is generally accepted that this mechanism describes MO sensing, it is recognized that effects of the microstructure of the MO, such as the ratio of surface area to volume, grain size, pore size, and film thickness play an important role (3).

The key parameters of a sensor are its sensitivity, response time, and recovery time. The sensitivity S is generally defined as the ratio of change of resistance for the test gas mixture R_t, to the resistance in a reference gas mixture R_r (1):

$$S = |R_r - R_t| / R_r \,. \qquad \text{(Equation 8.3)}$$

The response time of a sensor can be defined as the 1/e time required for the transition from R_r to R_t upon exposure to a certain test gas concentration. Similarly, the recovery time can be defined as the 1/e time required for returning from R_t to R_r.

The sensitivity, response time, and recovery time of ZnO thin-film sensing devices depend strongly on the operation temperature of the sensing layer, because adsorption and desorption are temperature-activated processes. The optimal operating temperature in conventional ZnO sensing devices is usually between 200 and 500°C. This requires a heating element next to the sensing layer, leading to extra power consumption in the order of several mW. This is too high for application in autonomous ultralow power systems which operate preferably at ~100 µW. Therefore, in order to reduce power consumption, the sensitivity of these devices needs to be increased, preferably such that room temperature (RT) operation becomes possible.

One way to increase the sensitivity of a ZnO layer to gases is to increase its surface to volume ratio, e.g. by making use of ZnO ultrathin-films (7,8). The smallest practical ZnO film thickness is approximately 40 nm, which is the critical thickness with respect to the resistivity (9). Below this critical value, the resistivity increases abruptly due to the scattering of electrons at grain boundaries. A higher sensitivity can also be achieved by nanostructuring the ZnO sensing devices (10,11). For example, high aspect ratio ZnO nanowires show a significant increase in response at room temperature compared to thin films (10). Another method to optimize the sensitivity of sensing devices at RT is to make use of doping. For example, if ZnO is doped with Al, its conductivity is increased. We note, that the level of Al doping is very important and needs to be controlled precisely (12).

Another method for optimizing the sensitivity of sensing devices is by catalytic enhancement. Several studies have shown remarkable improvement in gas sensing performance upon loading the sensing layer with metallic catalyst such as Pt, Pd, Ag, etc. (11,13-17). To explain the performance enhancement by the catalytic materials, two effects are mentioned (14):

Firstly, the work function of noble metal catalysts is generally higher than that of the semiconducting MO layer. This work function may lead to the formation of a space charge barrier at the metal -semiconductor interface due to the transfer of electrons from the MO into the noble metal. This has been shown to lead to an increased value of R_r at room temperature for SnO_2-metal catalyst structures, improving the R_r / R_t response (14).

Secondly, another property of noble metals that is mentioned regarding their use in gas sensors, is their ability to dissociate many molecular bonds. This has led not only to a wide use in catalytic reduction and oxidation processes but also to the detection of reducing or oxidizing gases (18). After dissociation, the molecular fragments can spillover from the noble metal to the MO, where they can adsorb on the surface and/or react with the surface species. For the application of catalysts to the surface of an MO sensing layer, the surface coverage, size distribution, and shape of the added catalytic material are very important (16). Noble metal nanoparticles (NPs) have a high catalytic activity due to nano-size effects and their high surface to volume ratio. Therefore, they are often employed in catalysis (19).

Opportunities for ALD in sensing

Atomic layer deposition (ALD) is a thin-film deposition technique, consisting of self-limiting chemical reactions between volatile precursor or reactant molecules and surface groups, carried out in a cycle-wise fashion. Due to the unique merits of ALD, it shows great potential for gas sensing applications. Firstly, ALD offers sub-nanometer thickness control with high uniformity over large substrates. Precise thickness control is very important since the sensitivity in thin-film sensing devices depends on film thickness, and shows an optimum when dimensions are in the order of the Debye length (9). Doping by ALD is also relatively straightforward, due to the cycle-wise fashion of the process. This enables the use of super cycles, in which dopant cycles are carried out in between the cycles of the MO matrix. In this manner, ALD can be used to deposit, e.g. both *i*-ZnO and Al-doped ZnO with excellent material properties (20,21). High quality Pt can also be deposited using ALD, with the ability to deposit Pt NPs as well as thin films (19,22,23). Pt NPs can catalytically enhance sensing devices. Furthermore, due to the self-limiting nature of the ALD half-reactions, extremely conformal layers can be deposited in 3-D substrates such as high aspect ratio trenches and anodized aluminum oxide (AAO) substrates. For example, conformal ALD ZnO films have been deposited in AAO pores with aspect ratio well over 100, and for plasma-assisted ALD of Pt, trenches with aspect ratios up to 22 have been coated conformally (24,25). All these aspects make ALD a promising technique to fabricate ZnO thin-film sensing devices and to coat these devices with Pt nanoparticles.

ALD can be used to deposit *i*-ZnO by subsequently exposing a substrate to diethyl Zn (DEZ, $Zn(C_2H_5)_2$) and deionized water vapor:

$$ZnOH^* + Zn(C_2H_5)_2 \rightarrow ZnOZn(C_2H_5)^* + C_2H_6 \qquad \text{(Equation 8.4)}$$

$$Zn(C_2H_5)^* + H_2O \rightarrow ZnOH^* + C_2H_6, \qquad \text{(Equation 8.5)}$$

where asterisks denote surface species (21). Between the exposure to the precursor and the deionized water vapor, purge steps are applied to remove excess gases and reaction products. Each ALD cycle consists therefore of a precursor step, a purge step, a de-ionized water vapor step, and another purge step. The growth per cycle (GPC) for ZnO at 250°C is typically 0.16 nm/cycle. Al-doped ZnO can also be deposited using ALD by working in super cycles. This basically means that the DEZ is replaced by trimethyl aluminum (TMA, $AlMe_3$) after a certain number "*n*" DEZ cycles (20). An Al-doped ZnO supercycle can therefore be defined as *n* cycles with DEZ, plus 1 cycle with TMA, where *n* is referred to as the cycle ratio. The GPC of a single Al_2O_3 cycle on a ZnO matrix is 0.15 nm/cycle. By tuning *n*, the Al concentration in the Al-doped ZnO can be controlled very precisely.

For the deposition of thin films of Pt the ALD process using $(MeCp)PtMe_3$ and O_2 gas has become very popular (26-32). As a result, the reaction mechanism has been studied quite extensively, and can be expressed through an overall expression such as (29,30):

2 $(MeCp)PtMe_3(g)$ + 3 O(ads) →

2 $(MeCp)PtMe_2(ads)$ + $CH_4(g)$ + $CO_2(g)$ + $H_2O(g)$ (Equation 8.6)

2 $(MeCp)PtMe_2(ads)$ + 24 $O_2(g)$ →

2 Pt(s) + 3 O(ads) + 16 $CO_2(g)$ + 13 $H_2O(g)$. (Equation 8.7)

Instead of O_2 gas, an O_2 plasma can also be used as a reactant. The advantages of using an O_2 plasma rather than O_2 gas are an extended temperature window (RT-300°C), faster nucleation on oxidic surfaces, and the possibility to deposit PtO_x as well as metallic Pt. During the nucleation stage, the Pt ALD process is characterized by a Volmer-Weber growth mode, where Pt NP islands form, grow, and coalesce during the initial cycles. A fully closed layer of Pt is not formed until a thickness of approximately 7 nm is reached in the case of the plasma-assisted process (23,31). This makes it possible to use ALD to deposit Pt NPs as well as thin films with control over the NP size distribution through the number of cycles. The nucleation of the Pt ALD process depends on the wetting condition of the substrate surface, and may therefore differ from one substrate material to another.

The primary goal of this work was to demonstrate that ALD can be used to fabricate ZnO sensing devices with Pt NPs, and to evaluate the RT sensing performance of these devices for O_2 and CO. Since to the best of our knowledge, the deposition of ALD Pt NPs onto *i*-ZnO has not been studied to date, we also report on the nucleation behavior of Pt ALD on ZnO. We note here, that combining Pt and Zn-based materials in a stacked layer does not necessarily yield two well separated material systems. The reason is that the diffusion of Zn through Pt has been reported in the literature, both when Pt was deposited on Zn-based materials and vice versa (33-35). The diffusion coefficient for Zn into Pt is estimated to be $5\cdot10^{-15}$ cm^2sec^{-1} at 100 °C, while the diffusion coefficient for Zn into e.g. Cu is $4\cdot10^{-22}$ cm^2sec^{-1} (36).

Furthermore, Zn and Pt are reported to be able to form alloy phases of different stoichiometries, e.g. PtZn and Pt_3Zn (37).

Experimental setup

The *i*-ZnO layers that were used to study the nucleation and growth of Pt NPs consisted of 40 nm ZnO films deposited on Si substrates with 450 nm thermally grown SiO_2 on top. Diethyl-Zn ($Zn(C_2H_6)_2$) was used as precursor and de-ionized water vapor as reactant and the substrate temperature was 250°C. The ZnO films were deposited on an open-load Oxford Instruments OPAL^{TM} reactor. Pt was deposited onto the ZnO films using (MeCp)$PtMe_3$ precursor (98% purity, Sigma-Aldrich) and O_2 plasma at 300°C, in a home built open-load reactor, described elsewhere (28). Prior to each Pt deposition, the ZnO samples received a 60 s O_2 plasma pre-treatment to remove any possible organic contaminants.

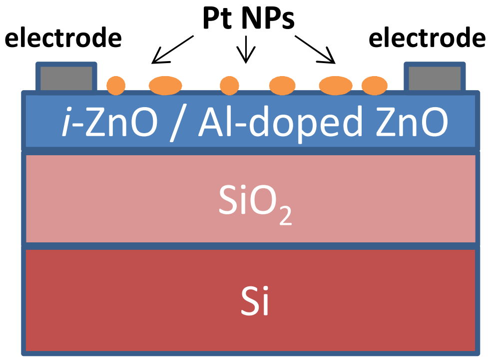

Figure 8.1. *Schematic of the gas sensing device. More details are described in Refs. (7,8).*

The thickness of the deposited Pt and ZnO layers was determined using a J. A. Woollam, Inc. M2000U ellipsometer. The Pt layers were modeled using a Drude-Lorentz parameterization, while the model for the ZnO layer contained a Drude term and a PSemi-M0 oscillator. To study the formation of Pt nanoparticles on ZnO, several TEM windows (14 nm thick Si_3N_4 membranes) were first coated with approximately 3-5 nm thick ZnO film using the same ALD process as used for the SiO_2/Si substrates. Next, 30, 60, 75, 250, 350, and 500 cycles of Pt ALD were applied on these TEM windows. TEM studies were performed using an FEI Tecnai F30ST microscope operated at 300 kV in high angle annular dark field (HAADF) - scanning TEM (STEM) mode. XPS experiments were performed on a Thermo Scientific K-Alpha KA1066 spectrometer with monochromatic Al K_α X-ray sources ($h\nu$ = 1486.6 eV).

A schematic of the gas sensing devices is shown in Figure 8.1. The *i*-ZnO films were deposited at 360°C in an ASM reactor with an EmerALD module. Al-doped ZnO films with a thickness of 40 nm were deposited by alternating 20 cycles DEZ and water vapor with 1 cycle of TMA and water vapor at 180°C (20). The ZnO films were deposited on substrates consisting of 500 nm thermal SiO_2 on Si. To measure the conductivity of the ZnO layer (sample area approximately 1 cm^2), Al electrodes (200 nm thick and 500 µm wide) were deposited on the ZnO layer using a shadow mask. Rapid thermal annealing (RTA) at 400°C in flowing N_2 was used for 60 s to decrease the contact resistance and improve the ZnO conductivity. Pt nanoparticles were deposited on both the *i*-ZnO and Al-doped ZnO sensing devices using 30, 50, and 70 cycles of Pt ALD. After the deposition of the Pt NPs, the devices were again treated with an RTA at 400°C for 60 s in N_2. The performance of reference sensing devices (without Pt NPs) was compared to that of Pt enhanced sensing devices.

The sensitivity of the ZnO sensing devices to O_2 and CO was tested in a gas-tight probe station, where a constant gas flow of 1 slm was maintained. O_2 and CO concentrations in the probe station were prepared by mixing a synthetic air flow with pure O_2 or CO (0.1% volume percentage in N_2). The humidity in the probe station was regulated by bubbling the main gas flow through bubblers containing distilled water. The O_2 concentrations could be mixed with accuracy of 0.1% (volume percentage). The CO concentrations with an accuracy of below 1 ppm could be maintained and the relative humidity could be varied from 0 to 100%. The current response of the ZnO layer was measured at a constant DC voltage of 1 V by using a semiconductor parameter analyzer (Agilent B1500A). All the gas sensing experiments were performed at room temperature.

Results

Pt ALD on ZnO

Figures 2 (a-g) show TEM images of the ZnO-covered TEM windows after 0, 30, 60, 75, 250, 350, and 500 cycles of plasma-assisted ALD of Pt. Figure 8.2

(c) shows a zoomed in section of Figure 8.2 (b) (30 cycles) as indicated by the black square. In these images, the formation and subsequent coalescence of Pt NPs becomes apparent. In Figure 8.3, the size distribution of the NPs for 30, 60, and 75 cycles is plotted. In Figure 8.4, the total surface coverage (a), average particle size (b), and the particle density (c) of the deposited Pt NPs are plotted as a function of number of cycles between 0 and 250 cycles.

Figure 8.2 (a) shows the bare ZnO-covered TEM window (0 cycles Pt ALD), where the ZnO grains can clearly be seen. After 30 cycles of ALD (Figure 8.2 (b)), Pt NPs can be distinguished as bright spots on top of the granular ZnO background (see also the zoomed in section in Figure 8.2 (c)). Figure 8.3 and 4 show that there is a relatively large number of small particles at the surface (no NPs with an area larger than 4 nm^2 were detected), that cover only a small part (~5 %) of the surface. After 60 cycles, these NPs have grown (average size is ~7 nm^2) and started to coalesce. The ZnO grains in the background can hardly be discerned anymore. After 75 cycles (Figure 8.2 (e)), the NPs have continued to grow and coalesce into islands-like structures. After 250 cycles, Figure 8.2 (f) shows almost 70 % of the ZnO substrate covered with Pt. In Figure 8.2 (g) (350 cycles) the Pt layer completely covers the surface and has formed relatively large granular structures. The darker regions in Figure 8.2 (g) are believed to be due to differences in height of the Pt layer, rather than indicating uncovered ZnO. The same holds for Figure 8.2 (h), where the same granular structure appears after 500 cycles. The projected area of the Pt grains in both Figure 8.2 (g) and (h) is approximately 35 nm^2.

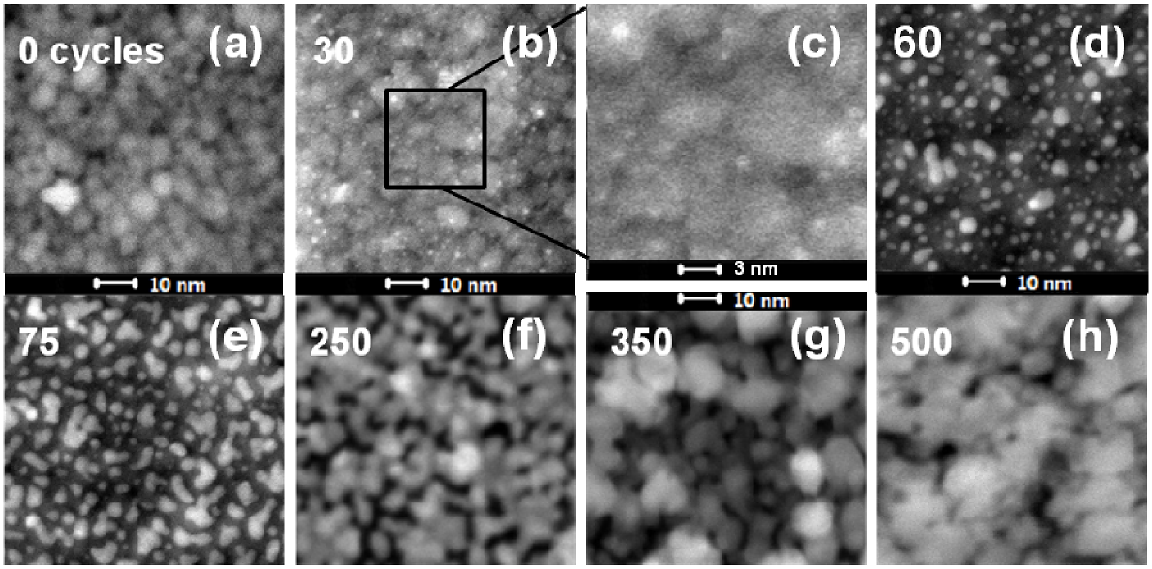

Figure 8.2. *HAADF-STEM images of 4 nm thick ZnO covered TEM windows with, 0, 30, 60, 75, 250, 350, and 500 cycles of plasma-assisted ALD of Pt carried out on top. Panel (c) shows a zoomed in section of panel (b) (30 cycles) as indicated by the black square.*

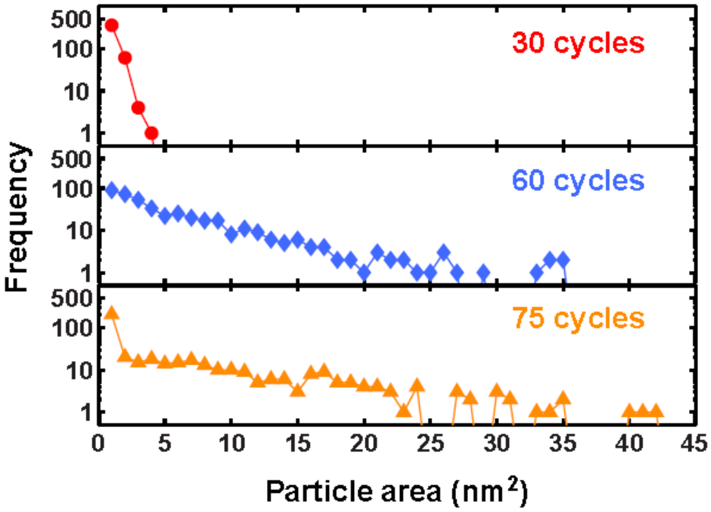

Figure 8.3. *The size distribution on a logarithmic scale for Pt nanoparticles deposited on ZnO using 30, 60, and 75 ALD cycles.*

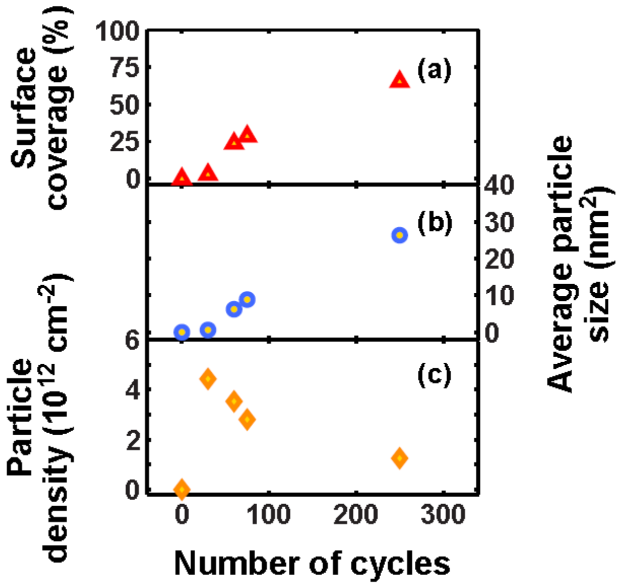

Figure 8.4. *The total surface coverage (a), average particle size (b), and the particle density (c) of the Pt nanoparticles deposited on ZnO as a function of the number of Pt-ALD cycles.*

To investigate the diffusion of Zn through Pt, XPS analysis was carried out on Pt films prepared by 2 to 2000 ALD cycles. The data (not shown here) showed the presence of both Zn and Pt for each sample, even for those with Pt films with a thickness of over 90 nm (XPS penetration depth ~10 nm). This clearly indicates the diffusion of Zn through the ALD-deposited Pt films. The diffusion behavior of Zn in the presence of Pt NPs requires further study.

Gas sensing measurements

into the for Figure sex underground Figure 8.5 shows the current response of Al-doped ZnO sensing devices to exposure to O_2 diluted in pure N_2 at RT, with Pt NPs (a), and without Pt NPs (b). The Pt NPs were deposited using 50 cycles of Pt ALD. During the experiments, different O_2 levels were admixed to the N_2 gas, as indicated by the dotted lines. Each O_2 dose lasted 1 hour. Although Figure 8.5 (a) and (b) have different baselines, the displayed range in both graphs is the same. As can be seen, the sensing device without Pt NPs shows no discernible current response to exposure to O_2 at RT. The sensing device with Pt NPs however, shows a clear proportional increase in current response upon exposure to O_2. For a fraction of 0.5 % the baseline current response (I_b) is ~4.21 (arbitrary units) at the onset of O_2 dosing and increases until the saturation current response (I_s) of 4.45 is reached. The sensitivity can now be defined as:

$S = |I_s - I_b|/I_b$, (Equation 8.8)

yielding a sensitivity of 5.7 % for a fraction of 0.5 %. For higher oxygen fractions the sensitivity was also calculated, and the results are shown in Figure 8.6 (a). Since for an oxygen fraction of 5 % and higher, I_s is not reached within the 1-hour oxygen flow period, the sensitivity was calculated by replacing I_s by the maximum current response I_m. This will however lead to an underestimation of the sensitivity and the response and recovery times.

Figure 8.6 (b) shows the response and recovery times as a function of oxygen fraction. Response time is defined as the time it takes the current response to transit from I_b to $I_b+(1-1/e)\cdot(I_s-I_b)$ where I_s may be replaced by I_m when appropriate; in short, the response time is the time required to reach ~63% of the saturation current response or the maximum current response. The recovery time is defined as the time it takes the current response to go from I_s to $I_b+(1/e)\cdot(I_s-I_b)$. The response and recovery times are relatively similar in magnitude and show that the sensing mechanism is relatively slow. Even for low oxygen fractions, response/recovery time is of the order of minutes.

The sensing devices with 30 and 70 cycles of Pt ALD also showed a response although both displayed a lower sensitivity than those with 50 cycles of Pt ALD: the sensitivities for 20% O_2 fraction was 15% for 30 cycles, and 4% for 70 cycles. The response of the sensing devices with 50 cycles of Pt ALD was also tested in the presence of H_2O (40% relative humidity), which showed a slight increase in the sensitivity compared to the results in pure N_2: ~55% for an O_2 fraction of 20%. The *i*-ZnO sensing devices with NPs also showed a similar response to O_2 at RT with a sensitivity of ~7% for an O_2 fraction of 20%. Compared to the Al-doped ZnO devices, the response and recovery times of the *i*-ZnO devices were somewhat longer.

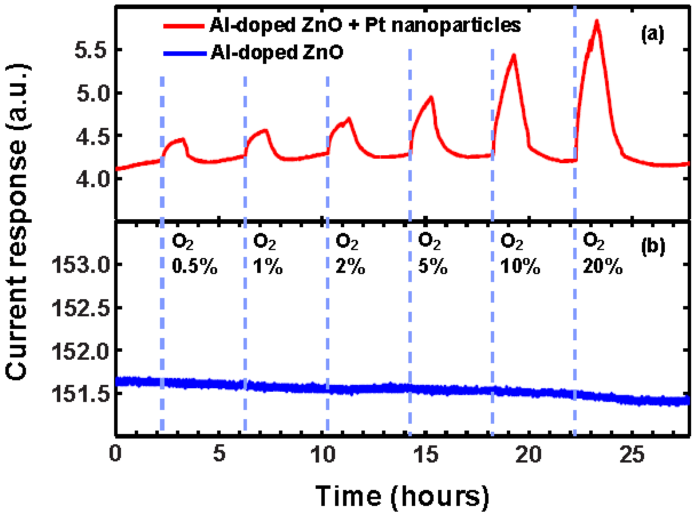

Figure 8.5. *Current response upon exposure to different levels of O_2 in N_2 at room temperature for Al-doped ZnO with (a) Pt nanoparticles, and without (b) Pt nanoparticles. Dotted lines indicate when the O_2 gas flow was turned on. The O_2 percentages ranged from 0.5 to 20 %.*

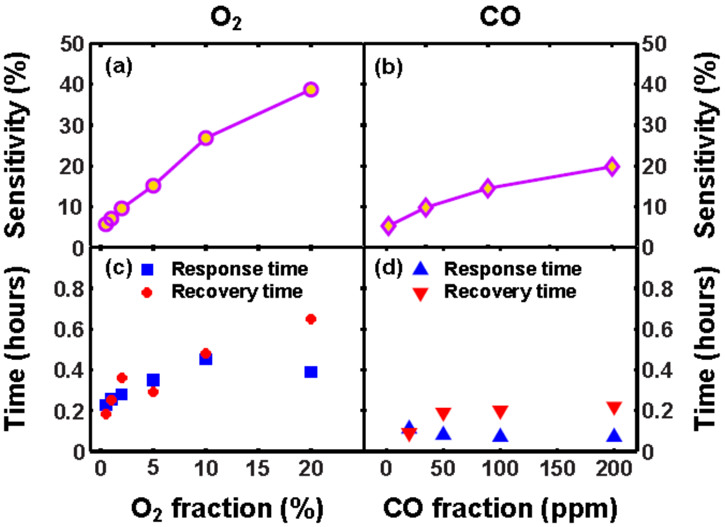

Figure 8.6. *Sensitivity, response time, and recovery time as a function of the gas fractions (O_2 and CO) to be detected for the Al-doped ZnO sensing devices operated at room temperature.*

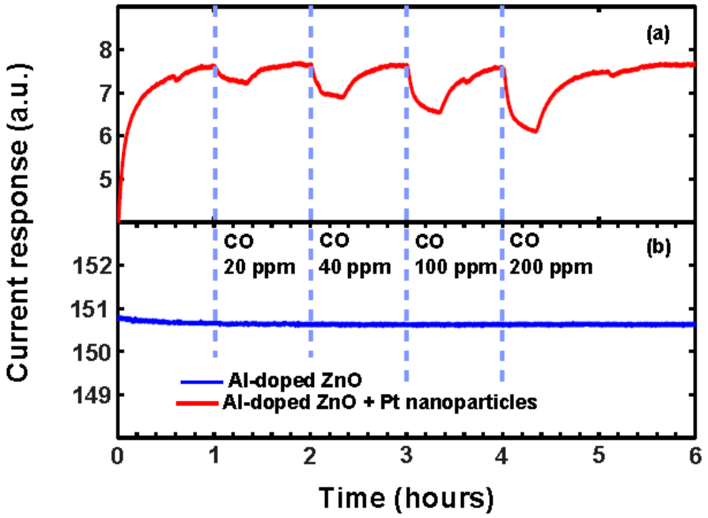

Figure 8.7. *Current response upon exposure to different levels of CO in N_2 mixed with 20% O_2 and H_2O at 40% relative humidity at room temperature for Al-doped ZnO with Pt nanoparticles (a), and without Pt nanoparticles (b). CO fractions are indicated alongside the dotted lines that indicate when the CO gas flow was turned on.*

Figure 8.7 shows the change in current response of an Al-doped ZnO sensing device with Pt NPs (50 ALD cycles) for CO exposure. At t = 0, pure N_2 is mixed with 20 % O_2 and H_2O at 40 % relative humidity. This causes an increase in the current response which stabilizes after approximately 1 hour. CO was added to this gas mixture at 20, 50, 100, and 200 ppm for 0.35 hours (21 minutes) as indicated by the dotted lines, causing a proportional and reversible decrease in current response. The sensitivity for CO as a function of CO fraction is given in Figure 8.6(b), and the response and recovery times are given in Figure 8.6 (d).

Conclusions

It was demonstrated that coating ALD-prepared *i*-ZnO and Al-doped ZnO sensing devices with ALD-deposited Pt nanoparticles enables room temperature sensing of O_2 and CO. It was shown that the size distribution of the Pt nanoparticles, deposited on ZnO, can be controlled through the number of ALD cycles. The Pt-enhanced sensing devices showed a reversible, proportional change in current response at room temperature upon exposure to O_2 and CO. The Al-doped ZnO device with 50 cycles of plasma-assisted ALD of Pt carried out on top could detect O_2, diluted in N_2, down to 0.5%. The sensitivity for O_2 was almost 40% for an O_2 fraction of 20%, with a response time of 0.4 hours and a recovery time of 0.65 hours. CO could be detected, diluted in N_2 in the presence of O_2 andH_2O, down to 20 ppm. The sensitivity for CO was 20% for a CO fraction of 200 ppm, with a response time of 0.05 hours and a recovery time of 0.2 hours. Reference devices without Pt nanoparticles showed no response at room temperature, indicating the importance of the Pt nanoparticles for the sensing mechanism.

Acknowledgments

This work is supported by NanoNextNL, a micro and nanotechnology program of the Dutch Ministry of Economic Affairs, Agriculture and Innovation (EL&I) and 130 partners. This research has also been supported financially by IMEC-NL, the Netherlands. The research of one of the authors (W.M.M. Kessels) is supported by the Netherlands Organization for Scientific Research (NWO) and the Technology Foundation STW through the VICI program on “Nanomanufacturing”. Thanks are due to M.F.J. Vos for his experimental work, and to J.J.A. Zeebregts, M.J.F. Van de Sande, and J.J.L.M. Meulendijks for their technical support.

Bibliography

1. G.Eranna, Metal Oxide Nanostructures as Gas Sensing Devices (CRC Press, Boca Raton, 2012).
2. M. Suchea, S. Christoulakis, K. Moschovis, N. Katsarakis, and G. Kiriakidis, *Thin Solid Films* **515**, 551 (2006).
3. M. E. Franke, T. J. Koplin, and U. Simon, *Small* **2**, 36 (2006).
4. K. M. Sancier, *J. Catal.* **9**, 331 (1967).
5. C. Cantalini, M. Post, D. Buso, A. Guglielmi, and A. Martucci, *Sensors and Actuators B-Chemical* **108**, 184 (2005).
6. Y. N. Xia, P. D. Yang, Y. G. Sun, Y. Y. Wu, B. Mayers, B. Gates, Y. D. Yin, F. Kim, and Y. Q. Yan, *Adv. Mater.* **15**, 353 (2003).
7. M.A. Blauw, V.A.T. Dam, M. Crego-Calama, S.H. Brongersma, J. Musschoot, and C. Detavernier, *10th IEEE Conf. on Sensors*, Limerick, Ireland, Oct. 28-31, (2011), p. 1416.

8. V. Dam, M. Blauw, S. Brongersma, and M. Crego-Calama, *Procedia Engineering* **5**, 172 (2010).
9. X. Du and S. George, *Sensors and Actuators B-Chemical* **135**, 152 (2008).
10. L. C. Tien, P. W. Sadik, D. P. Norton, L. F. Voss, S. J. Pearton, H. T. Wang, B. S. Kang, F. Ren, J. Jun, and J. Lin, *Appl. Phys. Lett.* **87**, 222106 (2005).
11. P. Singh, V. N. Singh, K. Jain, and T. D. Senguttuvan, *Sensors and Actuators B-Chemical* **166**, 678 (2012).
12. U. Ozgur, Y. I. Alivov, C. Liu, A. Teke, M. A. Reshchikov, S. Dogan, V. Avrutin, S. J. Cho, and H. Morkoc, *J. Appl. Phys.* **98**, 013502 (2005).
13. D. Haridas, A. Chowdhuri, K. Sreenivas, and V. Gupta, *Sensors and Actuators B-Chemical* **153**, 152 (2011).
14. D. Haridas, K. Sreenivas, and V. Gupta, *Sensors and Actuators B-Chemical* **133**, 270 (2008).
15. K. S. Kim, S. K. Jha, C. Kang, and Y. S. Kim, *Microelectron. Eng.* **86**, 1297 (2009).
16. D. Haridas, A. Chowdhuri, K. Sreenivas, and V. Gupta, *Sensors and Actuators B-Chemical* **153**, 89 (2011).
17. H. Y. Lai and C. H. Chen, *J. Mater. Chem.* **22**, 13204 (2012).
18. T. Yamaguchi, T. Kiwa, K. Tsukada, and K. Yokosawa, *Sensors and Actuators A-Physical* **136**, 244 (2007).
19. M. J. Weber, A. J. M. Mackus, M. A. Verheijen, C. van der Marel, and W. M. M. Kessels, *Chem. Mater.* **24**, 2973 (2012).
20. Y. Wu, P.M. Hermkens, B.W.H. van de Loo, H.C.M. Knoops, S.E. Potts, M.A. Verheijen, F. Roozeboom and W.M.M. Kessels, *J. Appl. Phys.*, **114** 024308 (2013).
21. J. W. Elam, D. Routkevitch, and S. M. George, *J. Electrochem. Soc.* **150**, G339 (2003).
22. T. Aaltonen, M. Ritala, T. Sajavaara, J. Keinonen, and M. Leskelä, *Chem. Mater.* **15**, 1924 (2003).
23. A. J. M. Mackus, M. A. Verheijen, N. M. Leick, A. A. Bol, and W. M. M. Kessels, *Chem. Mater.* **25**, 1905 (2013).
24. H. W. Huang, W. C. Chang, S. J. Lin, and Y. L. Chueh, *J. Appl. Phys.* **112**, 124102 (2012).
25. I.J.M. Erkens, M.A. Verheijen, H.C.M. Knoops, W. Keuning, F. Roozeboom, and W.M.M. Kessels, *to be published.*

26. J. Hämäläinen, F. Munnik, M. Ritala, and M. Leskelä, *Chem. Mater.* **20**, 6840 (2008).
27. H. C. M. Knoops, A. J. M. Mackus, M. E. Donders, M. C. M. van de Sanden, P. H. L. Notten, and W. M. M. Kessels, Electrochem*. Solid-State Lett.* **12**, G34 (2009).
28. I.J.M. Erkens, A.J.M. Mackus, H. C. M. Knoops, P. Smits, T.H.M. van de Ven, F. Roozeboom, and W. M. M. Kessels, ECS *Journal of Solid State Science and Technology* **1**, 255 (2012).
29. W. M. M. Kessels, H. C. M. Knoops, S. A. F. Dielissen, A. J. M. Mackus, and M. C. M. van de Sanden, *Appl. Phys. Lett.* **95**, 013114 (2009).
30. A. J. M. Mackus, N.Leick, L.Baker, and W.M.M.Kessels, *Chem. Mater.* **24**, 1752 (2012).
31. L. Baker, A. Cavanagh, D. Seghete, S. George, A. Mackus, W. Kessels, Z. Liu, and F. Wagner, *J. Appl. Phys.* **109** 084333 (2011).
32. S. T. Christensen and J. W. Elam, *Chem. Mater.* **22**, 2517 (2010).
33. J. Silvestre-Albero, J. C. Serrano-Ruiz, A. Sepulveda-Escribano, and F. Rodriguez-Reinoso, *Applied Catalysis A-General* **292**, 244 (2005).
34. M. Zawadzki, W. Mista, and L. Kepinski, *Vacuum* **63**, 291 (2001).
35. M. Consonni, D. Jokic, D. Y. Murzin, and R. Touroude, *J. Catal.* **188**, 165 (1999).
36. H. H. Uhlig, J. S. Macnairn, and D. A. Vaughn*, Acta Metallurgica* **3**, 302 (1955).
37. Z. Moser, *Journal of phase equilibria* **12**, 439 (1991).

Chapter 9

Conclusions and Recommendations

In this thesis, several aspects concerning thermal and plasma-assisted ALD of Pt have been investigated. The main goal of this work was to gain a better understanding of plasma-assisted ALD of Pt and PtO_x, and to use this understanding to explore possible practical applications. The following general conclusions can be drawn from the study:

- *Temperature dependence of the Pt ALD process and reaction mechanism.*
  Thermal ALD of Pt has a lower temperature limit at around 250 °C which narrows the thermal Pt ALD process window. As discussed in Chapter 4, this temperature limitation is due to inhibited ligand combustion. During the precursor pulse, the precursor ligands may undergo dehydrogenation and combustion reactions on the catalytic Pt surface, forming respectively methane and carbon dioxide. As a result of the surface reactions, a carbonaceous layer is formed at the end of the precursor pulse which prevents O_2 dissociation at lower temperatures. The relatively narrow temperature window of the thermal Pt ALD process is one of the main reasons for using plasma-assisted ALD of Pt.

- One of the main new insights that we have gained concerning plasma-assisted ALD based on $(MeCp)PtMe_3$ and O_2 plasma, is the great importance of the $(MeCp)PtMe_3$ and O_2 plasma doses. The importance of dosing for this process goes beyond one of the fundamental requirements for ALD, namely that the saturation dose needs to be delivered to the surface. In fact, the $(MeCp)PtMe_3$ and O_2 plasma doses each influence the *composition* of the deposited material, where the ratio between the doses and the substrate temperature is important. For deposition in high aspect ratio trenches, the importance of $(MeCp)PtMe_3$ and O_2 plasma doses becomes even more apparent. Inside these trenches, the ratio between $(MeCp)PtMe_3$ and O_2 plasma doses varies. This can result in the deposition of spatially separated Pt and PtO_x material zones inside a single trench, where the deposition profile can even be controlled through the precursor and O_2 plasma doses, as shown in Chapter 7. To deposit films consisting only of Pt or PtO_x inside high aspect ratio trenches, precursor and plasma exposures need to be optimized carefully, as demonstrated in Chapters 5 and 6.

- *Influence of precursor sticking and radical recombination in plasma-enhanced ALD of Pt in 3D features*
  Reaching saturation for ALD in high aspect ratio structures may require an optimization of precursor and/or reactant doses compared to ALD of planar substrates. Whether an optimization is necessary depends on the sticking probability of the precursor/reactant, and the aspect ratio of the feature. For plasma-assisted ALD the recombination probability of the plasma radical may also influence the saturation dose. Depositing conformal Pt films in high aspect ratio structures requires an optimization of the precursor and O_2 plasma exposures due to the near-unity sticking probabilities of the $(MeCp)PtMe_3$ precursor molecules (as determined in Chapter 3) and O-radicals and the surface recombination probability of the O-radicals. As demonstrated in Chapter 5, by making use of optimized exposures, conformal Pt thin films can be deposited in trenches with aspect ratios up to 34.

- *Process window extension from metallic Pt to oxidic PtO_x films*
  One highly significant outcome from this thesis work is the finding that plasma-assisted ALD based on $(MeCp)PtMe_3$ and O_2 plasma can be used to deposit both metallic Pt and PtO_x in a temperature window ranging from room temperature to 300 °C, as demonstrated in Chapter 6. The composition of the deposited material can be controlled through the $(MeCp)PtMe_3$ and O_2 plasma exposures. With increasing substrate temperature, the thermal stability of PtO_x decreases and the reducing activity of the precursor ligands increases. Therefore, longer O_2 plasma exposures and/or lower $(MeCp)PtMe_3$ exposures are required to obtain PtO_x at higher temperatures. At lower temperatures, Pt can be obtained by reducing the O_2 plasma exposure, by increasing the $(MeCp)PtMe_3$ exposure, or by making use of an additional reducing gas.

- *ALD for room temperature gas sensing*
  By exploiting the merits of ALD such as precise thickness control, the ability to produce doped materials using super-cycles, and the ability to deposit catalytic nanoparticles, the design of applications such as gas sensing devices can be optimized. As demonstrated in Chapter 8, ALD can be used to fabricate gas sensing devices that are capable of detecting O_2 and CO down to ppm levels at room temperature. The precise thickness control of ALD can deliver ZnO thin films with the optimum balance between surface-to-volume ratio and conductivity for gas sensing. Moreover, by using super-cycles of ZnO combined with Al_2O_3 ALD, the doping level could be controlled and thus the conductivity of the deposited Al-doped ZnO was improved. By using ALD to add catalytically active Pt nanoparticles to the surface of the sensitive Al-doped ZnO layer, room temperature gas detection is enabled.

The results and insights obtained in this work allow for the description of a number of directions for future research:

- To deposit Pt at lower temperatures using ALD based on $(MeCp)PtMe_3$ and O_2 plasma, H_2 is now employed to reduce the PtO_x that is formed during the O_2 plasma step. However, as we have demonstrated in Chapter 7, Pt can be deposited at temperatures as low as 100 °C inside trenches where the O_2 plasma exposure is sufficiently reduced. Further investigation, both experimentally and by modeling, could determine whether the O_2 plasma exposure can be controlled such that the deposition of Pt on planar substrates becomes possible at 100 °C or even room temperature, without making use of H_2. This could be done e.g. by igniting a short O_2 plasma at low O_2 gas pressures.

- As we have demonstrated in Chapter 8, the unique features of ALD make it a very promising technique to improve the design of gas sensing devices. The design we have presented, exploits the excellent thickness control of ALD, as well as the possibility to produce Al-doped ZnO and the ability to deposit catalytic Pt nanoparticles. Although we have demonstrated the working principle of this design for room temperature sensing, additional optimization steps are still required. For example, the influence of Al doping, the thickness of the Al-doped ZnO layer, or the size distribution and loading of the Pt nanoparticles on sensitivity and selectivity should be investigated extensively. The sensitivity and selectivity may also be improved significantly by the use of nanoparticles of other catalytic materials such as PtO_x, Pd, Ir, etc.

- One feature of ALD that could be used to further improve the design of gas sensing devices, and which has yet to be fully explored, is the ability to conformally deposit inside high aspect ratio features. By making use of high aspect ratio nanostructured surfaces, the interaction with the target gasses could be improved significantly. The excellent conformality of ALD makes it the ideal deposition technique for the fabrication of devices based on this improved sensing design. ALD could be used for example to coat anodized aluminum oxide or other nanostructured substrates with a conformal gas sensitive metal oxide layer.

  The sensitivity of gas sensing devices that make use of high aspect ratio nanostructured surfaces could be further improved by depositing catalytic nanoparticles on the gas sensitive layer, as was already demonstrated for planar surfaces. Uniform size distribution of these particles throughout the high aspect ratio feature is important because the nanoparticle size influences the catalytic activity. The size distribution of Pt nanoparticles depends on the oxygen exposure, which may vary inside high aspect ratio structures. This warrants a more detailed study into the size distribution of Pt nanoparticles on high aspect ratio surfaces.

- As discussed in Chapter 6, the reaction mechanism of ALD of PtO_x depends on precursor and O_2 plasma exposure, and the temperature of the substrate. Remarkably, the GPC of PtO_x is comparable to that of Pt, despite the fact that the density of PtO_x is only approximately half that of Pt. This indicates that during a PtO_x ALD cycle only half the amount of Pt is deposited on the surface. Further study is required to elucidate the reaction mechanism of ALD of PtO_x. This may also prove relevant for the conformal deposition of PtO_x inside high aspect ratio structures, which proved more challenging compared to Pt. Monte

Carlo simulations similar to those mentioned in Chapter 5 could be extended to include oxidation and reduction reactions in order to obtain more information on the ALD of Pt and PtO_x. A more detailed SEM/TEM study could be performed to investigate the conformality of ALD of PtO_x in high aspect ratio features.

Summary

Understanding and Controlling Atomic Layer Deposition of Platinum and Platinum Oxide

Atomic layer deposition (ALD) is a thin-film deposition technique, yielding high-quality thin-film materials with precise thickness control, excellent uniformity over large-area substrates, and superior conformality over demanding 3-D topologies. The standard ALD approach is thermally activated growth using two or more self-limiting half-reactions. Novel technology options arise by going beyond this standard, such as e.g. plasma-assisted deposition enabling low substrate temperatures, the deposition of nanoparticles, or the deposition of doped materials. This makes ALD a promising technique in emerging applications using heterogeneous device integration in the so-called *More than Moore* domain. Pt and PtO_x are relevant materials in these new application fields, with many potential uses for both thin films and nanoparticles deposited on planar substrates as well as on challenging surface topologies. In this dissertation, the process windows of Pt and PtO_x layer growth by ALD from $(MeCp)PtMe_3$ vapor and O_2 gas/plasma have been explored and expanded using both planar and 3D substrates.

First, the reaction mechanism of the thermal Pt ALD process was elucidated by studying the volatile reaction products during the precursor and oxygen step using in situ mass spectrometry. This showed that the lower limit of the temperature window (250-300 °C) is determined by the accumulation of carbonaceous surface species at the Pt surface thus inhibiting the dissociation of oxygen molecules. When using an O_2 plasma instead of O_2 gas, O-radicals are created and supplied directly from the gas phase to the surface. The O-radicals make surface-mediated dissociation no longer necessary and enable the combustion of the carbonaceous surface species at much lower temperatures, thus extending the lower limit of the temperature window down to room temperature.

The composition of the deposited films for the plasma-assisted ALD process based on $(MeCp)PtMe_3$ and O_2 plasma was found to be governed by three main

parameters: the substrate temperature, the O_2 plasma exposure, and the (MeCp)PtMe$_3$ precursor exposure. By an extensive investigation of the influence of these three parameters, we succeeded in adding PtO_x to the ALD materials toolbox. It has been established that with increasing substrate temperature, the thermal stability of PtO_x decreases and the reducing activity of the precursor ligands increases. Therefore, longer O_2 plasma exposures and/or lower (MeCp)PtMe$_3$ exposures are required to obtain PtO_x at higher temperatures. Finally, it was shown that both PtO_x nanoparticles and ultrathin films can be deposited in a temperature window ranging from room temperature to 300 °C.

For the conformal deposition of thin films of Pt and PtO_x in high aspect ratio (HAR) features, the (MeCp)PtMe$_3$ vapor and O_2 plasma exposures need to be carefully chosen in order to ensure that the surface reactions are saturated throughout the feature. It was demonstrated that Pt-films can be deposited conformally in trenches with an aspect ratio of up to 34. Films of PtO_x were deposited conformally in trenches with an aspect ratio of up to 9. Remarkably, by tuning the substrate temperature, and precursor and O_2 plasma exposure, both Pt and PtO_x can be deposited concurrently in a single HAR feature. In this case, even the composition profile along the feature can be explained and controlled.

Furthermore, an example of how ALD of Pt can be applied in future applications was given. Gas sensing structures prepared from Al-doped ZnO layers were coated with catalytic ALD-Pt nanoparticles. It was demonstrated how this paves the way for room temperature detection of O_2 (down to 0.5 % O_2 in N_2) and CO (down to 20 ppm CO in N_2). Room temperature gas detection would make the necessary heating element in today's gas sensing devices obsolete, and thus open up pathways for the further reduction or ultimately the elimination of heating power for ultralow power (< 100 µW) ZnO-based sensing devices used in wireless autonomous sensing networks.

In summary, the work presented in this dissertation has led to a better understanding of ALD of both Pt and PtO_x. The insights that were obtained at the atomic level enable an extremely accurate degree of materials and process control required for future applications in electronics and other fields. It is this level of control that allows the properties of ALD-grown layers of Pt and PtO_x to be tailored to the envisioned next-generation *More than Moore*-type devices.

Acknowledgments

The past four years have been the best of times and the worst of times. I believe that what I will remember most from my PhD experience, are the people I have met and worked with, many of whom deserve my thanks.

First of all I would like to thank the staff of PMP and the Holst Centre for offering me the opportunity to complete my PhD project. Thanks to Erwin Kessels for his sharp eye-opening comments, which have truly made me reflect on my work and allowed me to become a better scientist. Thanks to Fred Roozeboom for all his work, kind words and his warm personal touch in everything he does. Special thanks to Marcel Verheijen, ever friendly and cheerful. Without your knowledgeable, pragmatic, and to-the-point insights I would not have been able to write this thesis, and our discussions always provided me with much needed energy to continue my work.

I would also certainly like to thank my students, who have helped me gather much of the data that was used in this work, and without whom I could not have completed my PhD. Bas, Joris, Pepijn, Tijn, Koen, Koen, Koen, Martijn, Thomas, and Paul, being your supervisor has been a great experience and a lot of fun as well. Thanks also to Tatyana Landaluce and Wytze Keuning for their assistance in supervising several of my students and their insights and expertise.

Two people from PMP that I would like to thank for being my guides in the world of platinum ALD are Harm Knoops and Adrie Mackus. Thank you for letting me draw from your indispensable knowledge and experience. Of course I also would like to thank all the other people from the group for making the past four years a wonderful experience, professionally but certainly also personally. Many thanks also for the technical staff for all their hard work. For welcoming me so warmly to the city I fell in love with, I would like to thank Onno Gabriel and the people from PVcomB in Berlin.

It is difficult to express in words how much I would like to thank my family and friends for being in my life; you make me happy. I would also like to express my deep admiration for my sister Linda and my mother Marjo, two of the strongest women I know.

Most thanks go to my girlfriend Viola, who seems to know me better than I know myself. You have patiently stood by me through the best of it and the worst of it, and I'm truly grateful that I was able to share this eventful period of my life with you.

Curriculum vitae

Personal information

Family name	Erkens
Given names	Ivo Johannes Maria
Date of birth	17 February 1983
Place of birth	Heerlen

Education

1995-2001	Diploma Voorbereidend Wetenschappelijk Onderwijs, Katholiek Gymnasium Rolduc, Kerkrade, the Netherlands
2001-2006	Bachelor of Science Degree in Applied Physics, Eindhoven University of Technology, the Netherlands
2006-2008	Master of Science Degree in Applied Physics, Eindhoven University of Technology, the Netherlands Three months internship at the Francis H. Burr Proton Research Center, Boston, USA Master thesis project in the "Experience Processing" group at Philips Research, High-Tech Campus, Eindhoven, the Netherlands
2008-2010	Professional Doctorate in Engineering in "Design and Technology of Instrumentation," Eindhoven University of Technology, the Netherlands Three months working visit to PVcomB at the Helmholtz Zentrum Berlin, Berlin, Germany
2010-2014	PhD student in the group "Plasma & Materials Processing," Department of Applied Physics, Eindhoven University of Technology, the Netherlands